UNIVERSIDAD DE LAS PALMAS DE GRAN CANARIA

Optical Camera Communication for Internet of Things in Urban Environments

Presented by:

Patricia Ximena Chávez Burbano

Presented as part of the Doctoral Program
EMPRESA, INTERNET, Y TECNOLOGÍAS DE LAS COMUNICATIONES
at the city of
LAS PALMAS DE GRAN CANARIA
on Thursday 5th November, 2020

UNIVERSIDAD DE LAS PALMAS
DE GRAN CANARIA

D. Miguel Ángel Ferrer Balllester
COORDINADOR DEL PROGRAMA DE DOCTORADO
EMPRESA, INTERNET Y TECNOLOGÍAS DE LAS COMUNICACIONES
DE LA UNIVERSIDAD DE LAS PALMAS DE GRAN CANARIA,

Que la Comisión Académica del Programa de Doctorado en su sesión de fecha .... tomó el acuerdo de dar el consentimiento para su tramitación, a la tesis doctoral titulada "Optical Camera Communication for Internet of Things in Urban Environments” presentada por la doctoranda Dª Patricia Ximena Chávez Burbano y dirigida por los Doctores Rafael Pérez Jiménez y José Rabadán Borges.

Y para que así conste, y a efectos de lo previsto en el Artº 11 del Reglamento de Estudios de Doctorado (BOULPGC 7/10/2016) de la Universidad de Las Palmas de Gran Canaria, firmo la presente en Las Palmas de Gran Canaria, a...de...de dos mil...........

Dedication

I dedicated this research work to my family. At first to my mother who gave me moral lessons on discipline from an earlier age and helped me in all things great and small. A special feeling of gratitude to my dear husband, Ignacio, whose words of encouragement pushed me to pursue my dreams and finish my thesis. Also gratefulness to my beloved son, Antonio, who has been by my side during the last mile of this work. Finally, to the memory of my father. He was my inspiration to never give up.

Thank you to my academic advisers who guided me in this process and the committee who kept me on track.

If we knew what it was we were doing, it would not be called research, would it?

Albert Einstein

Acknowledgement

- Main supervisor: Rafael Perez-Jimenez
- Second supervisor: Jose Rabadan Borges
- Academic Staff:
  - Victor Guerra
  - Julio Rufo
- Technical or support staff
  - Ayaya Perera Casiano
  - Baltasar Perez Diaz
- Academic staff from other departments:
  - Stanislav Zvanovec
  - Stanislav Vitek
- Other istitutions:
  - Escuela Superior Politecnica del Litoral, Ecuador.
  - Czech Technical University in Prague, Czech Republic

Contents

i

Dedication **iv**

Epigraph **vi**

Acknowledgement **viii**

Contents **x**

List of Figures **xiii**

List of Tables **xvi**

List of Equations **xvii**

Abstract **xviii**

Resumen **xxvii**

I Introduction **1**
- I.1 Motivation 4
- I.2 Hypothesis 4
- I.3 Objectives 5
- I.4 Methodology 6

II Optical camera communication: present, challenges and trends **9**
- II.1 Optical camera communication characterization 10
- II.2 Internet of things' applications 11
  - II.2.a Positioning, tracking and navigation 11
  - II.2.b Intelligent Transportation System 13
  - II.2.c Wireless sensor networks 14
- II.3 Modulation's schemes 14
  - II.3.a Modulations based on OOK 14
  - II.3.b Polychromatic modulations 16
  - II.3.c Undersampling modulations 18
  - II.3.d Modulations based on space-time coding 21
  - II.3.e Other modulations 22

II.3.f Modulations' comparison 24

III Optical camera communication fundamentals 25

III.1 OCC emitters 26
III.2 Cameras' operation 28
III.2.a Global shutter 30
III.2.b Rolling shutter 31
III.3 Cameras' characteristics 32
III.3.a Image exposure 33
III.3.b Frame rate 34
III.3.c Camera's resolution 35
III.3.d Field of view 35
III.4 Digital multilevel signal processing 36
III.4.a Binarization 36
III.4.b Image segmentation 37
III.4.c Image masking 39
III.4.d Convolution filtering 40
III.4.e Morphological operations 40
III.4.f Statistical measures in digital image processing 41
III.5 OCC data extraction 42
III.6 Geometry of projected distances 43
III.6.a Projections with rotation over the vertical axis 45
III.6.b Projections with rotation over the horizontal axis 47
III.6.c Generalized projections 49
III.7 Normalized power signal to interference ratio 50

IV Distance-independent modulation 53

IV.1 Theoretical fundamentals 53
IV.1.a Switching frequency 54
IV.1.b Statistic data 56
IV.2 Wake up process 56
IV.3 Modulation technique 60
IV.3.a Frequency multiplier's selection 62
IV.3.b Switching frequencies' selection 63
IV.4 Modulation's advantages 64

V Simulations and experimental validation 67

V.1 Validation of projected pixels' estimation 68
V.1.a Experimental setup 69
V.1.b Experimental results 72
V.2 NPSIR's calculation 73
V.2.a Experimental setup 74
V.2.b Calculated NPSIR 77
V.3 NPSIR's validation 78
V.3.a Simulation setup 80
V.3.b Simulation's results 82

V.4 Positioning, and tracking system 82
V.4.a System setup 85
V.4.b Image processing 87
V.4.c Position's results 90
V.4.d Tracking 'process results 91
V.5 Outdoor wireless sensor network 91
V.5.a Experimental setup 93
V.5.b Experimental results 94
V.6 Flickering-free distance independent modulation's validation 94
V.6.a Simulation setup 96
V.6.b Simulation's results 97
V.6.c Experimental setup 97
V.6.d Experimental results 103

VI Conclusions and future research lines **107**
VI.1 Conclusions 107
VI.2 Future works 112

Bibliography **115**

List of Abbreviations **125**

Symbols **129**

Glossary **131**

List of Figures

Chapter II

II.1 Asynchronous OOK scheme for optical camera communication . . 15
II.2 CSK and CDMA for RGB-LED 17
II.3 ColorBars: CSK for optical camera communication 17
II.4 CSK using rolling shutter mode 18
II.5 UFSOOK 19
II.6 UPSOOK's example 19
II.7 RGB UPAM 20
II.8 Undersampled Pulse Width Modulation 21
II.9 Three-layered STC matrix 22
II.10 2D-OFDM for optical camera communication 23
II.11 OCC modulations' schemes 24

Chapter III

III.1 Optical camera communication system 25
III.2 White LED implementation: blue LED with a yellow phosphor coating 27
III.3 White LED implementation: additive color method 28
III.4 Camera's basic elements 29
III.5 Color Bayer filters array 30
III.6 CCD global shutter scheme 30
III.7 CCD global shutter frame acquisition time 31
III.8 CMOS rolling shutter scheme 31
III.9 CMOS rolling shutter frame acquisition time 31
III.10 Blooming effect example 33
III.11 Field of view and focal length 35
III.12 Original image for DSP examples 36
III.13 Gray-scale image's binarization: fixed threshold 37
III.14 Gray-scale image's binarization: Otsu thresholding 37
III.15 Image segmentation: consecutive regions 38
III.16 Image segmentation: non-consecutive regions 38
III.17 Image masking 39
III.18 Convolution filtering 40
III.19 Dilation 41
III.20 Erosion 41

III.21 Images with perfect anti-correlation 42
III.22 Images with low linear correlation 42
III.23 Data extraction: global shutter case 43
III.24 Data Extraction: rolling shutter case 44
III.25 Image acquisition 44
III.26 Horizontal projection 45
III.27 Vertical projection 46
III.28 OCC system's diagram 50

Chapter IV

IV.1 Rolling shutter effect 54
IV.2 Wake up algorithm's diagram. 57
IV.3 Transmission's examples. 59
IV.4 Data extraction scheme's diagram. 62
IV.5 PCC values vs Frequency 64

Chapter V

V.1 Testbed designed for validating pixels' projections 69
V.2 Implemented experimental testbed 69
V.3 Designed LED's board with the distances between its elements. . . 70
V.4 Example of the projected pixels' estimation 71
V.5 Identified regions 72
V.6 Optical interference experimental calculation procedure. 74
V.7 Dilated binary image for distance $D = 100$ cm. 75
V.8 Image processing phase 76
V.9 Optical power emitted by the top left LED of the designed board . 77
V.10 Webcam Bayer filter response for blue, green, and red respectively. 77
V.11 Webcam silicon responsivity. 77
V.12 NPSIR for transmitting in white. 78
V.13 NPSIR for transmitting in blue. 78
V.14 NPSIR for transmitting in red. 79
V.15 NPSIR for transmitting in green. 79
V.16 Simulated indoor WSN scenario. 79
V.17 Simulation's synchronization process 81
V.18 Dome camera perspective of the sensors. 81
V.19 Positioning, and tracking system Scheme 83
V.20 Representation of the data necessary for the localization process. . 84
V.21 Synchronization Scheme. 85
V.22 Beacons in the first frame 86
V.23 Objects to be located 87
V.24 Positioning system: image processing flow chart. 87
V.25 Beacons' binarized image. 88
V.26 Dilated Binary Image 88
V.27 Beacons' ROI 89

V.28 Objects' ROI 89
V.29 Location's error map 91
V.30 Tracking example 92
V.31 Outdoor WSN System 92
V.32 Outdoor WSN's transmitter. 93
V.33 Outdoor WSN field experiment 94
V.34 Outdoor WSN Experiment results 95
V.35 Simulated binary image 97
V.36 Pearson correlation coefficient 98
V.37 Field experiment emitter 98
V.38 Emitter's optical power. 100
V.39 Field experiment receiver. 100
V.40 Modulation scheme's results for $\alpha = 15$ 104
V.41 Modulation scheme's results for $\alpha = 30$ 105
V.42 Modulation scheme's results for $\alpha = 75$ 106

List of Tables

III.1 Consecutive regions' characteristics: segmentation over a binarized image case. 39

IV.1 Waking up examples 58

V.1 Calculated pixels for horizontal distance $d_x = 16mm$ 70
V.2 Calculated pixels for vertical distance $d_y = 19mm$ when it is located in the object's side that is located closer to the camera 70
V.3 Calculated pixels for vertical distance $d_y = 19mm$ when it is located in the object's side that is located farther from the camera 71
V.4 Consecutive regions' characteristics of example in figure V.4 72
V.5 Calculated distances of example in figure V.5 72
V.6 Average error for horizontal measurements in pixels 73
V.7 Average error for vertical measurements in pixels 73
V.8 Regions' characteristics of image in figure V.7 75
V.9 ROI's edges for images taken at 100 cm 75
V.10 BER Results from the Monte Carlo Simulation 82
V.11 BER results estimated from applying the NPSIR value 83
V.12 Frequency of the Devices' Identification Signal 85
V.13 Emitter's 3-D positions 86
V.14 Theoretical Band's widths 86
V.15 Beacons' extracted data 88
V.16 Objects' extracted data from example on figure V.26 89
V.17 Beacons' Identification results 90
V.18 Objects' Identification results from example on figure V.26 90
V.19 Located Objects' Positions for example in figure V.26 91
V.20 Videos Bit Error Rate 95
V.21 Pearson Correlation Coefficient obtained values. 99

List of Equations

III.1 Field of view in a camera 35
III.2 Region's circularity 39
III.3 Pearson Correlation Coefficient 42
III.11 Horizontal Projection: rotation over vertical axis 46
III.15 Vertical Projection: rotation over vertical axis 47
III.23 Vertical Projection: rotation over horizontal axis 48
III.27 Horizontal Projection: rotation over horizontal axis 49
III.28 Generalized Horizontal Projection 49
III.29 Generalized Vertical Projection 49
III.30 Optical power arriving to the camera 50
III.31 Projected pixels from source X 51
III.32 Pixels' relationship 51
III.33 Normalized Power Signal to Interference Ratio (NPSIR) 51
IV.2 Pixels on the light's stripes: generalized case 55
IV.3 Data decodification 61
IV.4 Pixels on the light's stripes in function of the frequency multiplier α . 62
IV.6 Frequency Multiplier 63
IV.7 Gap Between Frequencies 63
IV.10 Switching Frequencies 64
V.1 ROI's corner points 75
V.3 WSN's simulation bit value decision 80

Abstract

The implementation of Smart Cities might be the path for restraining the critical problems that massive urbanization has caused in the world. These issues deeply impacted the social, economic, and environmental fields. By definition, a smart city is an urban area where data is continuously collected and transmitted for analysis. Powerful analytic tools are applied to these data to extract valuable information for managing assets, resources, and services in the interests of better performance, lower costs, and lessened environmental impact. Therefore, the concept of smarter cities is related to the reduction of energy consumption and greenhouse gas emissions, the inclusion of sustainable transportation systems, and the improvement of human settlements management. Ultimately, the city's operational efficiency increases, as well as the quality of government services and citizen welfare.

The future of smart cities' applicability relies on today's research, development, and implementation of Internet of Things (IoT) applications within urban environments. The devices that gather the information can be considered IoT elements that can connect and communicate, through wires or wirelessly, with other apparatus over short, medium, and long distances. However, the massive number of sensors required by a smart city for accurate decision-making limits the implementation of traditional wireless communication links based on Radio-Frequency (RF). This type of communication has two main issues: the spectrum saturation and the inter-systems interference, then additional complementary wireless communication techniques are needed. Some RF-related solutions for Intelligent Transportation Systems (ITS), real-time environmental monitoring, and early disaster detection have been developed already. But those solutions usually interact with a significant amount of interference. Since these data networks are fundamental for future smart cities, these systems' possible failure is critical. Consequently, their implementation should not depend only on RF links.

Considering that social, economic, and environmental problems are global, it is essential to impulse the implementation of smart cities in developed countries, where some pilot cities are already working, and in developing countries where the economic and technological limitations should be considered. Accordingly, some smart cities' applications require the reuse of previous massive deployments and take advantage of technological trends. In addition, IoT deployments should avoid the saturated spectrum portion, offer reliable communication (redundancy is desirable), moderate delay, low jitter, adequate bit rate, and security.

Nowadays, one important technological trend is the use of Light Emitting

Diode (LED) for illumination, advertising, and decoration in both indoor and outdoor environments. The LED-based devices present several advantages: energy efficiency, extended life cycles, cost-efficient manufacturing process, and high switching rate. The replacement of fluorescent and halogen lamps by LED illumination systems is part of a global initiative to control excessive power consumption and reduce climate change. This change affects different environments, such as homes, buildings, streets (public lamps), traffic (new signaling lights), and cars (hazard, tail, sidelights, and so forth), even in developing countries. Additionally, there is a movement for using LEDs in walls, clothes, and accessories for decoration purposes and deploying new high-resolution displays based on organic LEDs. This massive utilization of LED-based devices impulses the development and implementation of Visible Light Communication (VLC) systems.

VLC is an optical wireless communication technology that works with the visible light portion of the electromagnetic spectrum (430 THz to 790 THz) and transmits data by modulating a light's characteristic. The emitters are light sources: lamps, screens, or signs. On the reception side, photodiode-based devices are used for sensing the light variation. This technology presents several benefits over RF: larger bandwidth, resistance to RF interference, more security, and an unlicensed spectrum portion. However, the implementation of VLC with photodiodes implies the use of external and potentially expensive devices. For this reason, this study focuses on OCC, a VLC-based technique that uses image sensors for receiving the signals. This technology takes advantage of two trends: the insertion of devices with embedded cameras in a wide variety of day-to-day activities and the massive implementation of outdoor camera-based security and monitoring systems.

In general, OCC employs pre-existing devices for transmitting and receiving the signal. Consequently, OCC deployment is low cost. Additionally, smartphones, watches, tablets, and wearables are usually equipped with medium-range resolution cameras which image acquisition speed is acceptable for communication purposes. This technique also includes the possibility of full-duplex communication by using an infrared upload link and the implementation of Multiple-Input Multiple-Output (MIMO) systems by deploying spatially separated light sources. The employment of OCC as a complementary wireless communication technique for deploying IoT applications within urban environments requires an extended analysis.

The main goal of the IoT applications on urban environments would be the collection of data. Therefore a unidirectional link could satisfy this objective eliminating the necessity of studying the feasibility of potential uplinks. Similarly, the implementation of MIMO systems and adaptation of image processing techniques to enhance communication can be neglected in this research first stage. However, the study of the communication channel's characterization and the impact's analysis of the image sensors characteristics (shutter type, exposition time, distortions) over the data decodification are fundamental for characterizing indoor and outdoor implementations.

For applications within urban environments, the distance between the emitters

and the receivers can vary from some centimeters to several hectometers, affecting each transmitter's projection in the acquired image. This issue affects not only the number of pixels in the collected image corresponding to the emitted data source limiting the data transmitted by frame, but it also compromises the meaning of close-emitters interference. To estimate the number of pixels that a light source projects on the image, a set of simple equations were deduced. In this way, the systems can be designed or adapted easily for the minimum quantity of available pixels' specific constraints. In these links, other light source interference depends on the 2D projection's proximity, even if the emitters are safely separated in the real world. It is necessary to quantify this interference and then predict its impact over the communication link. For this task, it is fundamental to calculate the number of pixels representing the real-world objects and the relation between the legit signal and the interference, known as Normalized Power Signal to Interference Ratio (NPSIR).

Additionally, a study of currently proposed modulation techniques is necessary for developing a long-distance solution. In general, the OOK-based modulations are low complexity techniques that work correctly with moderate data rates exclusively for short distances. Therefore, this type of OCC modulations can be used for specific IoT applications within the range of 5 m, which support a low data rate. Since the polychromatic modulations take advantage of the red, green and blue (RGB) channels for simultaneous transmissions, the data rate increases, however, the achieved distance is short, and the system's complexity is moderate for Color Shift Modulation (CSK) and high for the CIELUV space. Nevertheless, implementing a polychromatic version of other modulations showed better results regarding data rate without increasing the complexity. The undersampled techniques provide the fastest transmissions rates with moderate to high complexity and medium-range distances. The modulations based on space-time coding reach long distances with relatively low data rates and very high complexity. Since the proposed implementations require specialized hardware for too complex processing, these techniques are not suitable for smart cities in developing countries. Finally, in all the cases, the modulation schemes that compare consecutive frames reach the most extended distances with moderate complexity. Other long-distance modulation schemes that have been proposed rely on significant or high complexity algorithms that require a thresholding technique for identifying the light state.

Moreover, the most advanced schemes use bits in each transmission header for calibration purposes, decreasing the throughput. Therefore, for developing a long-distance implementation, modulation schemes based on the comparison of consecutive frames is the best available option that overcomes these constraints. Additionally, the OCC implementations should avoid the flickering problem, so the lights can also be used for illumination, decoration, or advertising purposes without disturbing the people. The flickering free modulations with low complexity algorithms only perform adequately for a medium distance range because the number of bits represented in a single frame decreases with the distance. In general, the available modulation methods work correctly for either short or long distances but not for both cases. In this work, a flickering free, distance independent modulation that overcomes these constraints is proposed. This scheme can be defined as a rolling shutter effect-based modulation that requires a minimum number of light bands for extracting the information. Therefore it can work for short, medium and long distances.

Since OCC receivers, image sensors, were designed for obtaining pictures, it is necessary to adapt its operation for recollecting the transmitted data. The first step for achieving this purpose is to analyze a camera's function. In general, the cameras receive light through an opening in the objective for a defined period, known as exposure time (T_{EXP}). The light is focused on the image sensor chip using the imaging optic lenses. Then the microlenses array focuses the light on the semiconductors for producing electrical signals. Since the photosensors detect light intensity without wavelength specificity, each semiconductor is affected by a color filter, having a one color signal. The collected charge is converted to a voltage that is amplified to produce the electrical signal. A gamma correction tone is applied to the linear photon capture for assuring a normal distribution in the image's histogram. The electrical signals are digitized, then a spatial interpolation operation (demosaicking) is used for reconstructing a color image. Finally, the image is compressed and stored. The adequate camera's characteristics can be selected for controlling the image acquisition while highlighting the specific light changes in the frames. The transmitted data must be extracted from the frames. Therefore some digital multilevel signal processing tools are required for preparing the images and videos and bring out the information. Once the frame is processed, the data can be decoded.

This research work "Optical Camera Communication for Internet of Things in Urban Environments" focused on the possibility of implementing IoT applications that transform cities in developing countries by using OCC technology. Since proving the predictions is a fundamental phase in any scientific research, some simulations, lab experiments, and field tests were performed as part of this thesis for validating the possibility of such implementation. At first, a set of trials were done in a darkroom for validating the usability of equations III.28 and III.29, presented in section III.6, for estimating the number of pixels that ureal world objects produce in an image without complex plane transformations or projections. This estimation is fundamental for determining the closeness of light sources within an OCC system; and, therefore, for predicting the interference from close-emitters and its impact on the communication's performance. In the same way, the emitter's pixel projection approximation is used as a constrain value during the implementation of the proposed distance-independent modulation scheme. Once the accuracy of this pixels' estimation was validated, the prediction of close-emitters interference over an OCC communication link had to be proven. For this purpose, initially, an experiment was designed to obtain the values of the relation NPSIR, introduced in section III.7. These experimental measurements were then used to prove the usability of the NPSIR to directly quantify the impact of relative close emitters over the communication's link performance. An indoor Wireless Sensor Networks using OCC was designed and sim-

ulated. The BER of this system was calculated using the NPSIR values. These predictions were compared with the simulation's outcomes regarding the accuracy of the received signal. In this way, the possibility of estimating the impact of close-emitters interference over an OCC communication link was proved. This prediction of the communication performance's degradation due to the closeness of light sources can be used for avoiding its effect by applying interference compensation on the receiver side during the data extraction process or by placing the system's emitters adequately during the applications' implementation.

The next step in the research was to demonstrate the existence of viable OCC applications for IoT. Two proposed implementations were validated with lab tests and field experiments. The first one was an indoor positioning and tracking system, that can be adapted for outdoor applications, while the second one was an outdoor WSN for smart cities. With those simulations and field experiments, the implementation of OCC-based systems for IoT was validated. Nevertheless, the outdoor implementation was no flickering-free; the long-distance demodulation process required the same light state in the full emitter image even if the receiver was a rolling shutter camera. In this particular field experiment, since the selected LED-based device was used for advertising purposes, the flickering was not an issue. However, in general, the outdoor applications need a flickering-free distance-independent modulation scheme, like the one proposed in chapter IV. This process required validation for short, medium, and long-distance rages to be used in different applications. A two-phase procedure was used to prove that this scheme works appropriately.

During the first stage, the procedure for selecting the switching frequencies was tested. For this purpose, the modulated signals using the proposed scheme were generated using the switching frequencies obtained by applying equation IV.10 for different frequency multiplier values. Then these signals were used as the input of the light emitters in the frame's acquisition simulations. From these simulations, the corresponding Pearson correlation coefficient values were calculated to demonstrate the usability of the frequency selection procedure. Once this process was validated, the switching frequencies for three different distance ranges were selected and applied during the second stage. The experimental implementation of the proposed scheme was done using those frequencies for determining the system's Bit Error Rate and therefore prove that the proposed modulation scheme can be used for applications independently of the distance range.

From the simulations, lab evaluations, and field experiments, several conclusions were reached. At first, the usability of equations III.28 and III.29 for estimating the 2D pixel representation of real-world distance was validated with an average pixel error of 0.5605. Additionally, the importance of the minimum focus distance on the pixel representation prediction was established. For the samples taken at a position closer than the minimum focus distance ($D \leqslant 40$ cm), the maximum error was 2.7547 pixels, while the other samples presented values below one pixel. Furthermore, by taking into account only the pictures that observed that minimum distance, the mean error decreased to 0.3089 pixels (3.55%). The equations III.28 and III.29 estimate the 2D pixel's projection (x, y) in a photograph of an actual distance (dx, dy) in function of the separation between the object and the camera, the relative angles of the object, and the camera's characteristics. Therefore the first detailed objective of this thesis was fulfilled.

Then the interference from close-emitters within an OCC system was experimentally characterized in function of the transmitted wavelength and then used to calculate the relation NPSIR as a measurement of this chromatic interference. As expected, the worst-case scenario was the transmission of white light, which is affected by the three channels, resulting in lower NPSIR values. Additionally, when the legit emitter's transmission and the additional light source were done in the same wavelength, or the interference came from a device emitting white light, the NPSIR reaches the lowest results affecting the data communication negatively. For the other samples, the results showed a dependency on the selected wavelength. For the transmissions in blue and red, the interference came from close sources emitting in green, while the LED transmitting in green was affected similarly by blue and red emissions.

For the distance $D = 100$ cm, where the pixel separation between the sources' boundaries was around six pixels, the NPSIR represented minimum interference, above $86dB$, demonstrating that the communication link would not be affected by the close-emitter interference even when transmitting in the same wavelength. Therefore distances above six pixels are considered perfect spatial separation. On the other hand, for the distance $D = 200$ cm, where the pixel separation between the sources' boundaries was around one pixel, the NPSIR values for the two sources transmitting in the same wavelength and white light interference were below $50dB$. These values would impact the communication link's performance significantly. Therefore distances below one pixel are considered critical spatial separation. Finally, for the distance $D = 140$ cm, where the pixel separation between the sources' boundaries was around three pixels, the NPSIR values for the two sources transmitting in the same wavelength and white light interference were below $75dB$. These values would negatively impact the communication link's performance, but the effect will not be as bad as the critical case. Therefore distances between one and six pixels are considered limited spatial separation.

Since the NPSIR measures interference independently of the system characteristics, the experimentally calculated values can be applied for directly estimating the impact of relative close emitters over the communication's link performance. For this purpose, equation V.4 should be applied with the emitter's optical power and camera's Color Filter Array (CFA) and silicon responsivity, as was done in the experiment described in section V.3. The directly calculated BER values were compared with an extensive computational simulation of the camera system over several distances obtaining similar outcomes. Nevertheless, the values from the application of the NPSIR were slightly greater than the other ones in all the cases. Therefore we can conclude that the NPSIR provides an upper limit of the system's BER. Consequently, the usability of the introduced NPSIR for quantifying the impact of relative close emitters over the OCC systems' communication link was proved, fulfilling the second detailed objective.

The fulfillment of objectives 1 and 2 helped to prove the validity of the hypotheses 1 "OCC close-emitter interference can be characterized for indoor and outdoor implementations." The NPSIR provides an estimation of the maximum BER due to the interference of close emitters. This value can be used for predicting the interference of similar systems by projecting the distance in pixels. Therefore, the designed implementations can be validated, and some specific preventive measures can be implemented for mitigating the interference of close emitters.

The simulated scenario of section V.3 also proved the feasibility of implementing an indoor WSN based on OCC, contributing to attaining the fourth detailed objective of this thesis. The data communication for the worst case, the sensors one near the other (distance between the sensors' center is 2.08 cm, corresponding to critical separation), had a maximum simulated BER of $5.09 \cdot 10^{-4}$. When the separation between the centers reaches 4.00 cm (perfect spatial separation) the BER was less than $1 \cdot 10^{-6}$.

For proving the validity of the flickering-free distance-independent modulation scheme proposed in chapter IV simulations and field experiments were held. The simulations were developed for testing the procedure for selecting the switching frequencies. Then this procedure was applied for determining the switching frequencies for three different distance ranges. During the field experiments, these switching frequencies were used, and the system's BER and successful probability were calculated. In this way, the whole proposed modulation scheme was validated for applications independently of the distance range.

From the simulations, the resulting frames had at least 18 strip lines for all the tested frequencies. In the other case, the switching frequencies corresponding to $\alpha \leqslant 64$, the theoretical upper limit for the frequency multiplier, generated bandwidth of at least five pixels that can be easily extracted from longer distances. With these results, the proposed boundaries for the frequency multiplier has been validated. Additionally, the obtained PCC for each data symbol fitted perfectly within the defined range. Therefore, the procedure for selecting the switching frequencies was validated.

On the other hand, the field experiment proved the feasibility of implementing the proposed flickering-free distance-independent modulation scheme. For the short distance range, the transmission was successful with BER of $5 \cdot 10^{-4}$ for three consecutive frames at 20 m where 1.5 light bands were extracted. Equivalently, the transmission for medium distance range was successful with BER of $1.8 \cdot 10^{-3}$ for 3 consecutive frames and $1.1 \cdot 10^{-3}$ for 4 consecutive frames at 40 m where 1.5 light bands were extracted. Finally, at 95 m, long-distance range, the link has BER of $7 \cdot 10^{-4}$ for 3 and 4 consecutive frames that contains only 1,5 light bands, and the BER increases to $2 \cdot 10^{-3}$ for 3 consecutive frames and up to $7 \cdot 10^{-4}$ for 4 consecutive frames at 100 m. Additionally, the success probabilities are above 99.6% for distances that assures at least 1.5 light bands on each frame. These results demonstrated that the modulation scheme is functional, even when only 1.5 light bands are extracted.

The proposed modulation method was based on the analysis of the consecutive frames PCC without the implementation of calibration procedures. The simplicity of the wake-up process and the modulation method assures an overall minor complexity, an improvement compared with other long-distance modulation techniques, which presented significant and high complexity. Additionally, the results for three consecutive frames are comparable to the modulation schemes' outcomes based on the analysis of successive frames (long distance with moderate complexity). At the same time, the throughput of the system ($f_{cam} * 2/3$ bps) is better. Moreover, the experimental results showed a useful 100 m link using a frequency multiplier below the maximum calculated for the camera's characteristics. Therefore, longer distances can be easily reached.

Since both the simulations and the experiments presented positive results, the flickering-free distance-independent modulation scheme for OCC was validated. Furthermore, the third detailed objective was fulfilled. Since similar BER results and succeed probabilities were obtained for the short, medium, and long-distance range cases, it was proved that the modulation scheme performance does not depend on the distance itself. The real constrain for this modulation technique is the number of light bands extracted from the frame. The system requires at least 1.5 strips for proper demodulation. Therefore, the Hypothesis 2 "OCC systems can be deployed for medium and long distances by using a distance-independent modulation scheme based on consecutive frames relations without the necessity of previous calibration." has been validated.

The real-time two-step 3D localization system based on OCC was tested under lab conditions. During the experiments, four objects were accurately positioned at the same time. The maximum location error was acceptable for the three dimensions: 3.10 cm in x dimension, 2.65 cm in y dimension, and 1.32 cm in the z dimension. Moreover, the mean location error was 1.2404 cm, with an average processing time of 18.2 ms per frame. These results proved the applicability of such positioning system, which can be easily implemented, for example, in the emerging Industrial Internet of Things (IIoT) applications field for robots' navigation. The tracking phase of the system was proved with a mean error of 1.07 cm. The proposed method can then be applied for any tracking execution where the objects to be located do not possess embedded cameras but own a LED.based device. Consequently, these experimental results demonstrated that the proposed positioning system contributes to fulfilling this thesis's fourth detailed objective.

It is essential to highlight that the proposed localization system's position accuracy depends on the camera's resolution and FoV and the distance to the beacons. Each pixel represents a specific total distance over a plane parallel to the camera's normal plane in any image. This value is based on the plane and image sensor separation and the camera's characteristics. If the resolution is increased, the accuracy is also incremented. However, an enhancement on the FoV or a greater separation would decrease the position's accuracy. For example, each pixel in the photos took during these experiments at a distance of 2.00 m represents 3.40 mm. If the camera's resolution is changed to 1920 × 1080, each pixel will correspond to 1.24 mm. Therefore, in the second case, the position accuracy will increase remarkably since any on- pixel error would lead to a 1.24 mm location error. Furthermore, the camera's selection and set up during the system's implementation should take this effect into account.

The outdoor WSN system based on OCC was tested with a field experiment. A long-distance communication link, more than 300 m, between an old generation smartphone and a LED-based advertising device was successfully established. Despite the use of a fixed threshold for decoding the captured signal, the quality of the camera's sensor, the camera's instability during the trials, and the environmental conditions (fresh breeze and haze), the system reached an average BER of $1.388 \cdot 10^{-2}$, and a worst-case with BER of $2.222 \cdot 10^{-2}$. Therefore, this experiment demonstrated that an OCC application for IoT within urban environments is possible, fulfilling this thesis's fourth detailed objective.

The experimental results showed that the proposed distance-independent modulation scheme is effective and can be applied for long-distance implementations. Additionally, the feasibility of practical OCC-based implementations for IoT have been demonstrated. Furthermore, for eliminating the flickering issue of the proposed outdoor WSN system, the validated distance-independent modulation scheme can be employed. This WSN implementation can be used for environmental pollution monitoring, temperature or humidity variation control, water contamination monitoring, and disaster detection. Therefore the hypothesis 3 "OCC is a valid technique for implementing Internet of Things' systems in Urban Environments" was validated by reaching the detailed objectives three and four.

Resumen

La urbanización masiva que se ha desencadenado en todo el mundo en las últimas cuatro décadas ha causado graves problemas, impactando negativa y profundamente en los campos social, económico y ambiental. La implementación de Ciudades Inteligentes (Smart Cities) podría ser uno de los caminos para limitar o mitigar el impacto de varios de los problemas más críticos acarreados por este crecimiento desmedido de las urbes. Por definición, una ciudad inteligente es un área urbana donde una variedad de datos se recopilan constantemente, a fin de ser transmitidos en tiempo real para su análisis. Posteriormente, se aplican potentes herramientas estadísticas y analíticas a estos datos para extraer información específica que resulta valiosa y clave para tomar decisiones con respecto a la operación de la ciudad. En otras palabras, esta información permite la adecuada y eficiente administración de los activos, recursos y servicios de la ciudad en aras de un mejor rendimiento, menores costos y menor impacto ambiental. Adicionalmente, el concepto de ciudades más inteligentes está relacionado con la reducción del consumo de energía, la reducción de las emisiones de gases de efecto invernadero, la inclusión de sistemas de transporte sostenibles y la mejora en la gestión de los asentamientos humanos. En última instancia, la eficiencia operativa de la ciudad aumenta, así como la calidad de los servicios gubernamentales y el bienestar de los ciudadanos.

El futuro de la aplicabilidad de las ciudades inteligentes depende de muchos factores, entre los cuales podemos destacar la implementación eficiente de Internet de las cosas (IoT), el uso de tecnologías emergentes para la comunicación de datos y el uso inteligente de infraestructura preexistente. Es por ello que resulta importante la investigación, desarrollo e implementación de aplicaciones de Internet de las cosas (IoT) en entornos urbanos, no únicamente para interiores que son las aplicaciones actuales más comunes. Los dispositivos que recopilan la información en las ciudades inteligentes pueden ser considerados elementos IoT que requieren conectarse y comunicarse, a través de cables o de forma inalámbrica, con otros aparatos en distancias cortas, medias y largas. Sin embargo, la gran cantidad de sensores requeridos para que una precisa y eficiente decisión sea tomada en una ciudad inteligente, limita la implementación de los tradicionales enlaces de comunicación inalámbricos basados en Radio Frecuencia (RF). Estos sistemas de comunicación presentan principalmente dos problemas: la saturación del espectro radioeléctrico y la interferencia entre sistemas. Por estos motivos, se requieren nuevas técnicas de comunicación inalámbrica que trabajen de forma complementaria con los sistemas RF. Actualmente se han desarrollado algunas

soluciones basadas en RF para sistemas inteligentes de transporte (ITS), monitoreo ambiental en tiempo real y detección temprana de desastres. Sin embargo esas soluciones generalmente interactúan con una gran cantidad de señales de interferencia y un elevado piso de ruido. Dado que estas redes de datos son fundamentales para las futuras ciudades inteligentes, una posible falla de estos sistemas es considerado un problema crítico. En consecuencia, su implementación no debería depender únicamente de los enlaces RF.

Teniendo en cuenta que los problemas sociales, económicos y ambientales causados por la urbanización masiva son globales, es esencial impulsar la implementación de ciudades inteligentes no solo en los países desarrollados, donde algunas ciudades piloto ya están funcionando, sino también en los países en vías de desarrollo. Sin embargo, las implementaciones en los países del tercer mundo requieren consideraciones especiales relacionadas con las limitaciones económicas y tecnológicas que caracterizan a estos lugares. En consecuencia, el diseño y desarrollo de aplicaciones para ciudades inteligentes deberían aprovechar las tecnologías e infraestructuras instaladas previamente, así como las nuevas tecnologías orientadas al bajo consumo de recursos. Además, las futuras implementaciones de IoT deberían evitar la porción saturada del espectro radioeléctrico, mientras ofrece una comunicación confiable, retraso moderado, baja fluctuación de desfase, adecuada tasa de transferencia de datos y seguridad de la información.

Actualmente existe la tendencia extendida de emplear diodos emisores de luz (LED) para iluminación, publicidad y decoración, tanto en ambientes interiores como en exteriores. Existe una amplia variedad de dispositivos basados LEDs, los cuales presentan varias ventajas: eficiencia energética, ciclos de vida prolongados, procesos de fabricación rentables y alta velocidad de conmutación. Por estos motivos, el reemplazo de lámparas fluorescentes y halógenas por sistemas de iluminación LED es parte de una iniciativa global, implementada incluso en países en vías de desarrollo, para controlar el consumo excesivo de energía y reducir de esta manera el impacto del cambio climático. Este reemplazo afecta a diversos entornos entre los que podemos mencionar: hogares, edificios públicos y privados, calles (sistemas públicos de iluminación), tráfico (semáforos y nuevas luces de señalización) y automóviles (faros, luces traseras, luces laterales, etcétera). Adicionalmente, existen dos tendencias muy marcadas: usar LED con fines decorativos en paredes, ropa y accesorios; y emplear pantallas de alta resolución basadas en LED orgánicos como elementos publicitarios. Esta utilización masiva de dispositivos basados en LED impulsa el desarrollo e implementación de sistemas de comunicación por luz visible (VLC).

VLC es una tecnología de comunicación óptica inalámbrica que funciona con la porción de luz visible del espectro electromagnético (430 THz a 790 THz) y transmite datos mediante la modulación de una de las características de una luz. Los emisores son fuentes de luz: lámparas, pantallas o letreros, mientras que en el lado del receptor, los dispositivos basados en fotodiodos se utilizan para detectar la variación de la luz. Esta tecnología presenta varios beneficios sobre los enlaces RF tradicionales: mayor ancho de banda disponible, resistencia a la interferencia RF, más seguridad en las transmisiones y la utilización de una porción no licenciada y no saturada del espectro electromagnético. Sin embargo, la implementación de VLC con fotodiodos implica el uso de dispositivos externos, dedicados y potencialmente costosos. Por este motivo, este estudio se centra en la comunicación óptica por cámaras (OCC), una técnica basada en VLC que utiliza sensores de imagen, como las cámaras fotográficas digitales, para recibir las señales. Esta tecnología aprovecha principalmente dos tendencias: la inserción en una amplia variedad de actividades cotidianas de dispositivos con cámaras integradas y la implementación masiva de sistemas de seguridad y monitoreo basados en cámaras exteriores.

En términos generales, OCC emplea dispositivos preexistentes para transmitir y recibir la señal. En consecuencia, la implementación de estos sistemas OCC podría ser de menor costo. Además, los teléfonos inteligentes, relojes, tabletas y dispositivos portátiles generalmente están equipados con cámaras de resolución de rango medio cuya velocidad de adquisición de imágenes es aceptable para fines de transmisión de datos puntuales. Esta técnica también incluye la posibilidad de comunicación full-duplex mediante el uso de un enlace de subida a través de LED infrarrojos, y la implementación de sistemas de múltiples entradas y múltiples salidas (MIMO) mediante el despliegue de fuentes de luz separadas espacialmente. Sin embargo, el posible uso de OCC como una técnica de comunicación inalámbrica complementaria a las tecnologías existentes, para desplegar aplicaciones de IoT en entornos urbanos requerirá un análisis extendido.

El objetivo principal de las aplicaciones IoT en entornos urbanos es la recopilación de datos. Por lo tanto, un enlace unidireccional podría satisfacer este objetivo eliminando, al menos por el momento, la necesidad de estudiar la viabilidad de posibles enlaces de subida. De manera similar, la implementación de sistemas MIMO y la adaptación de técnicas de procesamiento de imágenes para mejorar el desempeño de la comunicación pueden obviarse en esta primera etapa de investigación. Sin embargo, el estudio de las interferencias que pueden afectar al sistema de comunicación y el análisis del impacto que las características propias de los receptores (tipo de obturador, tiempo de exposición, lentes) podrían tener sobre la decodificación de datos son fundamentales para caracterizar adecuadamente las implementaciones en interiores y exteriores.

Para aplicaciones en entornos urbanos, la distancia entre los emisores y los receptores puede variar desde algunos centímetros a varios hectómetros, afectando la proyección de cada transmisor en la imagen adquirida. Este problema afecta no solo al número de píxeles en la imagen recopilada que corresponden al emisor, lo cual limita los datos transmitidos por cuadro, sino que también compromete el significado de la interferencia de los emisores cercanos. Para estimar el número de píxeles que una fuente de luz proyecta en la imagen, se dedujeron un conjunto de ecuaciones simples. De esta manera, los sistemas se pueden diseñar o adaptar fácilmente para las restricciones específicas de la cantidad de píxeles disponibles para la decodificación. En estos enlaces, la interferencia de otras fuentes de luz depende de la proximidad existente en la imagen. Incluso si los emisores están separados de forma segura en el mundo real, la proyección de los transmisores en la fotografía puede estar superpuesta. Es necesario cuantificar esta interferencia y luego predecir su impacto sobre el enlace de comunicación. Para esta tarea, es fundamental calcular la cantidad de píxeles que representan los objetos del mundo real y la relación en píxeles entre la señal legítima y la interferencia. Esta relación es conocida como relación normalizada de señal de potencia a interferencia (NPSIR).

Adicionalmente, se presenta un estudio profundo de las técnicas de modulación propuestas actualmente para desarrollar soluciones basadas en OCC. En general, las modulaciones basadas en encendido-apagado (OOK) son técnicas de baja complejidad que funcionan correctamente con velocidades de transmisión de datos moderadas exclusivamente para distancias cortas. Por lo tanto, este tipo de modulaciones OCC se puede usar para aplicaciones IoT específicas para transmitir datos puntuales dentro del rango de distancias inferiores a los 5 m. Dado que las modulaciones policromáticas aprovechan los canales rojo, verde y azul (RGB) para transmisiones simultáneas, la velocidad de transferencia de datos aumenta. Sin embargo, la distancia alcanzada no mejora significativamente y la complejidad del sistema es moderada para la modulación por variación de color y alta para la modulación basada en el espacio de color CIELUV. En cambio, la implementación de la versión policromática de otras modulaciones mostró mejores resultados en términos de velocidad de transferencia de datos sin aumentar significativamente la complejidad de los algoritmos. Las técnicas de modulación con submuestreo proporcionan las velocidades de transmisión de datos más rápidas con una complejidad entre moderada y alta, alcanzando distancias de rango medio. Las modulaciones basadas en la codificación espacio-temporal alcanzan largas distancias con una velocidad de datos relativamente baja y una complejidad muy alta. Dado que las implementaciones propuestas requieren hardware especializado para un procesamiento extremadamente complejo, estas técnicas no son adecuadas para ciudades inteligentes en países en vías de desarrollo. Finalmente, en todos los casos, los esquemas de modulación basados en la comparación de cuadros fotográficos consecutivos alcanzan las distancias más largas con complejidad moderada. Los demás esquemas de modulación para larga distancia que se han propuesto se basan en algoritmos de alta complejidad que requieren la aplicación de umbrales para identificar el estado de la luz. Además, los esquemas más avanzados usan bits en cada encabezado de transmisión con fines de calibración, disminuyendo la tasa de transferencia efectiva de información. Por lo tanto, para desarrollar una implementación a larga distancia, los esquemas de modulación basados en la comparación de tramas consecutivas son la mejor opción disponible que supera estas restricciones. De igual manera, las implementaciones de OCC debería evitar el problema del parpadeo, a fin de que emisores puedan ser empleados para aplicaciones de iluminación, decoración o publicidad sin causar problemas a las personas. Los esquemas de modulación sin problemas de parpadeo que emplean algoritmos de baja complejidad únicamente trabajan adecuadamente para distancias cortas o medias, debido a que el número de bits que se pueden representar en una sola trama disminuye con la distancia entre el emisor y la cámara. En general, los métodos de modulación disponibles en la actualidad sólo pueden emplearse para distancias cortas o largas, pero no para los dos casos. En esta tesis se presenta un esquema de modulación libre de parpadeo e independiente de la distancia que supera estas limitaciones. Este método es definido como una técnica de modulación basada en el efecto del obturador rodante (*"rolling shutter"*) que necesita un número mínimo de bandas de luz proyectadas en la fotografía para poder extraer la información transmitida. Por ende, este esquema puede trabajar para diferentes rangos de distancia.

Dado que los receptores OCC, las cámaras digitales, fueron diseñados para obtener imágenes, es necesario adaptar su operación para recolectar los datos transmitidos. El primer paso para lograr este propósito es analizar el funcionamiento de una cámara. En términos generales, las cámaras reciben luz a través de una apertura en el objetivo por un período de tiempo definido, conocido como tiempo de exposición (T_{EXP}). La luz se enfoca en el chip del sensor de imagen utilizando las lentes ópticas. La luz cae sobre una matriz de microlentes que la enfoca nuevamente sobre los semiconductores para producir señales eléctricas. Estos fotosensores detectan la intensidad de la luz sin especificidad de longitud de onda o información de color. Por ello, cada detector se ve afectado por un filtro de color que separa la luz por el rango de longitud de onda, produciendo una señal de un solo color. Los fotodiodos reciben la luz y capturan los fotones. Hay dos formas posibles de leer la luz incidente: obturador global (se captura todo el cuadro a la vez) y obturador rodante (la escena se escanea por bandas). La carga acumulada se convierte en un voltaje que se amplifica para producir la señal eléctrica de salida. Se aplica un tono de corrección gamma a la captura lineal de fotones, para que el histograma de la imagen tenga una distribución normal. Las señales eléctricas se digitalizan y se les aplica una operación de interpolación espacial para reconstruir una imagen en colores. Luego, la imagen se comprime utilizando información de luminancia de 8 bits por color para cada píxel, perdiendo información. Finalmente, la imagen resultante se almacena. Con base a lo anteriormente expuesto, se pueden seleccionar las características adecuadas de la cámara para controlar la adquisición de imágenes mientras se resaltan, dentro de lo posible, los cambios de luz específicos de la transmisión de datos en cada uno de los cuadros fotográficos. Los datos transmitidos deben ser extraídos de las tramas. Por este motivo se deben emplear herramientas de procesado de señales multinivel para preparar las imágenes y/o videos. Una vez que las tramas son procesadas, la información puede ser decodificada.

Este trabajo de investigación "Comunicación óptica con cámaras para Internet de las cosas en entornos urbanos" se centró en la posibilidad de implementar aplicaciones IoT para transformar y mejorar ciudades en países en vías de desarrollo mediante el uso de tecnología OCC. Dado que demostrar los enunciados es una fase fundamental en cualquier investigación científica, como parte de esta tesis se realizaron algunas simulaciones, experimentos de laboratorio y pruebas de campo para demostrar la viabilidad de una implementación de este tipo. Al principio, se realizaron un conjunto de pruebas en un cuarto oscuro para validar la usabilidad de las ecuaciones III.28 y III.29, presentadas en la sección III.6 , para estimar la cantidad de píxeles que los objetos del mundo real producen en una imagen sin la necesidad de emplear transformaciones complejas. Esta estimación es la base para determinar la proximidad de las fuentes de luz dentro de un sistema OCC y por lo tanto para predecir la interferencia de emisores cercanos y su impacto en el desempeño del sistema de comunicación. De la misma manera, la aproximación de la proyección de píxeles del emisor se usa como valor de restricción durante la implementación del esquema de modulación independiente de la distancia propuesto. Una vez validada la precisión de la estimación de estos píxeles, se procedió a comprobar que se puede predecir la interferencia de emisores cercanos sobre un enlace de comunicación OCC. Para ello, inicialmente se diseñó un experimento para obtener los valores de la relación NPSIR. Luego, estas medidas experimentales se utilizaron para probar la usabilidad del NPSIR para cuantificar directamente el impacto de emisores relativamente cercanos sobre el rendimiento del enlace de comunicación. Se diseñó y simuló una red inalámbrica de sensores (WSN) para interiores usando OCC. La tase de error en la transmisión de bits (BER) de este sistema se calculó utilizando los valores de NPSIR. Estas predicciones se compararon con los resultados de la simulación del sistema WSN propuesto. De esta forma, se comprobó la posibilidad de estimar el impacto de la interferencia de emisores cercanos sobre un enlace de comunicación OCC. Esta predicción de la degradación del rendimiento de la comunicación debido a la proximidad de las fuentes de luz se puede utilizar para evitar su efecto aplicando compensación de interferencia en el lado del receptor durante el proceso de extracción de datos o colocando los emisores del sistema adecuadamente durante la implementación de las aplicaciones.

El siguiente paso en la investigación fue demostrar la existencia de aplicaciones OCC viables para IoT. Dos implementaciones propuestas fueron validadas con pruebas de laboratorio y experimentos de campo. La primera fue un sistema de localización y seguimiento para interiores que se puede adaptar para aplicaciones al aire libre, mientras que el segundo fue una WSN para ciudades inteligentes. Con esas simulaciones y experimentos de campo, se validó la implementación de sistemas basados en OCC para IoT. Sin embargo, la implementación de la WSN no fue libre de parpadeos, el proceso de demodulación de larga distancia empleado requería el mismo estado de luz en toda la porción de la imagen que correspondía al emisor, incluso si el receptor era una cámara con obturador rodante. En este experimento de campo en particular, dado que el dispositivo basado en LED que se seleccionó es empleado con fines publicitarios, el parpadeo no fue un problema. Sin embargo, en general, las aplicaciones al aire libre necesitan un esquema de modulación independiente de la distancia pero sin parpadeo, como el propuesto en este trabajo. Este proceso requirió validación para distintos rangos de distancia: corto, medio y largo, a fin de que se pueda utilizar en diferentes aplicaciones. Para demostrar que este esquema funciona correctamente, se utilizó un procedimiento de dos fases.

Durante la primera etapa de la validación, se corroboró el procedimiento para seleccionar las frecuencias de conmutación de la señal. Para ello, se generaron señales moduladas utilizando el esquema propuesto y las frecuencias de conmutación obtenidas aplicando la ecuación IV.10 para diferentes valores del multiplicador de frecuencia α. Luego, estas señales se utilizaron como entrada de los emisores de luz en las simulaciones de adquisición de la trama. A partir de los resultados gráficos de estas simulaciones, se calcularon los valores del coeficiente de correlación de Pearson (PCC) correspondientes para demostrar la usabilidad del procedimiento de selección de frecuencia. Una vez validado este proceso, se seleccionaron las frecuencias de conmutación para tres rangos de distancia diferentes y se aplicaron durante la segunda etapa. La implementación experimental del esquema propuesto se realizó utilizando esas frecuencias para determinar el BER del sistema y, por lo tanto, demostrar que el esquema de modulación propuesto se puede usar para aplicaciones independientemente del rango de distancia.

Con base en las simulaciones, evaluaciones de laboratorio y experimentos de campo realizados se llegaron a varias conclusiones. En primer lugar, la usabilidad de las ecuaciones III.28 y III.29 para estimar la representación 2D en píxeles de distancias del mundo real se validó con un error de píxel promedio de 0.5605. Adicionalmente, se estableció la importancia de la distancia mínima de enfoque en la predicción de la representación en píxeles. Para las muestras tomadas en una posición más cercana que la distancia mínima de enfoque ($D \leqslant 40$ cm), el error máximo fue 2.7547 píxeles, mientras que las otras muestras presentaron valores por debajo de un píxel. Además, al tomar en cuenta solo las imágenes que observaron esa distancia mínima, el error medio disminuyó a 0.3089 píxeles (3.55%). Las ecuaciones III.28 y III.29 estiman la proyección 2D en píxeles de una distancia real (dx, dy) en función de la separación entre los objeto y la cámara, los ángulos relativos del objeto y las características de la cámara. Por tanto, se cumplió el primer objetivo detallado de esta tesis.

Luego se caracterizó experimentalmnete la interferencia de emisores cercanos dentro de un sistema OCC, en función de la longitud de onda transmitida. Esta carcterización fue empleada para calcular la relación NPSIR como una medida de esta interferencia cromática. Como era de esperar, el peor escenario fue la transmisión de luz blanca, que se ve afectada por los tres canales cromáticos (rojo, verde y azul), lo que resulta en valores de NPSIR más bajos. Además, cuando la transmisión del emisor legítimo y la fuente de luz adicional se realizó en la misma longitud de onda o la interferencia provino de un dispositivo que emite luz blanca, el NPSIR alcanzó resultados más bajos afectando negativamente la comunicación de datos. Para los otros escenarios, los resultados mostraron una dependencia de la longitud de onda seleccionada. Para las transmisiones en azul y rojo, la interferencia provino de fuentes cercanas que emitían en verde, mientras que el LED que transmite en verde se vio afectado de manera similar por las emisiones en azul y rojo.

Para la distancia $D = 100$ cm, donde la separación de píxeles entre los bordes de las fuentes era de alrededor de seis píxeles, la NPSIR representaba una interferencia mínima, por encima de $86dB$, lo que demuestra que el enlace de comunicación no se vería afectado por la interferencia de emisor cercano incluso cuando se transmitía en la misma longitud de onda. Por lo tanto, las distancias superiores a seis píxeles se consideran una separación espacial perfecta. Por otro lado, para la distancia $D = 200$ cm, donde la separación de píxeles entre los bordes de las fuentes era de alrededor de un píxel, los valores de la NPSIR para las dos fuentes que transmiten en la misma longitud de onda y la interferencia de luz blanca estaban por debajo de $50dB$. Estos valores implican un impacto significativo en el desempeño del enlace de comunicación. Por lo tanto, las distancias por debajo de un píxel se consideran separación espacial crítica. Finalmente, para la distancia $D = 140$ cm, donde la separación de píxeles entre los límites de las fuentes era de alrededor de tres píxeles, los valores de la NPSIR para las dos fuentes que transmitían en la misma longitud de onda y la interferencia de luz blanca estaban por debajo de $75dB$. Estos valores impactarían negativamente en el rendimiento del enlace de comunicación, pero el efecto no será tan malo como en el caso crítico. Por lo tanto, las distancias entre uno y seis píxeles se consideran separación espacial limitada.

Dado que la NPSIR mide la interferencia independientemente de las características del sistema, los valores calculados experimentalmente se pueden aplicar para estimar directamente el impacto de los emisores relativamente cercanos sobre el rendimiento de otros enlaces de la comunicación. Para ello, la ecuación V.4 debe aplicarse con la potencia óptica del emisor y la capacidad de respuesta del silicio y el filtro de color de la cámara, tal como se hizo en el experimento descrito en la sección V.3. En este caso, los valores de BER calculados directamente se compararon con una simulación computacionalmente extensiva del sistema obteniendo resultados similares. Sin embargo, los valores de la aplicación de la NPSIR fueron ligeramente superiores a los de la simulación en todos los casos. Por lo tanto, podemos concluir que la NPSIR proporciona un límite superior de la BER del sistema. En consecuencia, se demostró la usabilidad de la NPSIR para cuantificar el impacto de emisores relativamente cercanos sobre el enlace de comunicación en sistemas OCC, cumpliendo el segundo objetivo detallado.

El cumplimiento de los objetivos 1 y 2 ayudó a probar la validez de la hipótesis H1 "La interferencia de emisores cercanos puede caracterizarse para implementaciones OCC en interiores y exteriores". La NPSIR proporciona una estimación del BER máximo debido a la interferencia de emisores cercanos. Este valor se puede utilizar para predecir la interferencia de sistemas similares proyectando la distancia en píxeles. Por tanto, se pueden validar las implementaciones diseñadas y se pueden implementar algunas medidas preventivas específicas para mitigar la interferencia de emisores cercanos.

El escenario simulado de la sección V.3 también demostró la viabilidad de implementar una WSN basado en OCC para interiores, contribuyendo parcialmente a alcanzar el cuarto objetivo detallado de esta tesis. La comunicación de datos para el peor de los casos, distancia crítica entre los sensores, tuvo un BER máximo simulado de $5.09 \cdot 10^{-4}$. Cuando la separación entre los centros de los sensores alcanza los $4,00$ cm (separación espacial perfecta) el BER descendió por debajo de $1 \cdot 10^{-6}$.

Al analizar las tramas resultantes de las simulaciones para la validación del proceso de selección de frecuencias del esquema de modulación propuesto se observó que los fotogramas resultantes tenían al menos 18 líneas de franjas para todas las frecuencias probadas. En el caso del ancho de píxel de las bandas, las frecuencias de conmutación correspondientes a $\alpha \leqslant 64$, límite superior teórico para el multiplicador de frecuencia, generaron un ancho de banda de al menos cinco píxeles por lo que las bandas se pueden extraer fácilmente. Con estos resultados se han validado los límites propuestos para el multiplicador de frecuencia. Además, el PCC calculado para cada símbolo de datos encaja perfectamente dentro del rango definido. Por tanto, se validó el procedimiento para seleccionar las frecuencias de conmutación.

Por otro lado, el experimento de campo demostró la viabilidad de implementar el esquema de modulación sin parpadeo independiente de la distancia. Para el rango de distancia corto, la transmisión fue exitosa con BER de $5 \cdot 10^{-4}$ durante 3 fotogramas consecutivos a 20 m donde se extrajeron 1,5 bandas de luz. De manera equivalente, la transmisión para un rango de distancia medio fue exitosa con BER de $1.8 \cdot 10^{-3}$ para 3 tramas consecutivas y $1.1 \cdot 10^{-3}$ para 4 tramas consecutivas a 40 m donde Se extrajeron 1,5 bandas de luz. Finalmente, a 95 m, rango de distancia largo, el enlace tiene BER de $7 \cdot 10^{-4}$ para 3 y 4 fotogramas consecutivos que contienen solo 1,5 bandas de luz, y el BER aumenta a $2 \cdot 10^{-3}$ por 3 fotogramas consecutivos y hasta $7 \cdot 10^{-4}$ por 4 fotogramas consecutivos a 100 m. Además, las probabilidades de éxito están por encima de $99,6\%$ para las distancias que aseguran al menos 1,5 bandas de luz en cada trama. Estos resultados demostraron que el esquema de modulación es funcional, incluso cuando solo se extraen 1,5 bandas de luz.

El método de modulación propuesto se basó en el análisis de la PCC de tramas consecutivas sin la necesidad de implementar procedimientos de calibración. La simplicidad del proceso de activación de la comunicación y el método de modulación aseguran en general una complejidad bajo, lo cual representa una mejora en comparación con otras técnicas de modulación de larga distancia que presentan una complejidad significativa y alta. Adicionalmente, los resultados de 3 fotogramas consecutivos son comparables a los resultados de los dos esquemas de modulación basados en el análisis de tramas consecutivas que alcanzan largas distancias con una complejidad moderada, mientras que la tasa de transferencia efectiva del sistema propuesto ($f_{cam} * 2/3$ bps) es mejor. Además, los resultados experimentales mostraron un enlace práctico de 100 m mediante el uso de un multiplicador de frecuencia por debajo del valor máximo calculado para las características de la cámara. Por lo tanto, se pueden alcanzar fácilmente distancias más largas.

Dado que tanto las simulaciones como los experimentos presentaron resultados positivos, se validó el esquema de modulación independiente de la distancia sin fluctuaciones para OCC. Además, se cumplió el tercer objetivo detallado de la tesis, dado que se obtuvieron resultados de BER y probabilidades de éxito similares para los casos de corto, mediano y largo alcance. De esta manera se demostró que el rendimiento del esquema de modulación no depende en sí de la distancia. La restricción real de esta técnica de modulación es el número de bandas de luz que se pueden extraer de la trama. El sistema requiere al menos 1,5 tiras para una demodulación adecuada. Por lo tanto, la hipótesis H2 "Los sistemas OCC se pueden implementar para distancias medias y largas utilizando un esquema de modulación independiente de la distancia basado en relaciones de tramas consecutivas sin la necesidad de calibración previa" ha sido validada.

El sistema de localización 3D en tiempo real basado en OCC fue validado en condiciones de laboratorio. Durante los experimentos, cuatro objetos se colocaron con precisión al mismo tiempo. El error de ubicación máximo fue aceptable para las tres dimensiones: 3.10 cm en la dimensión x, 2.65 cm en la dimensión y y 1.32 cm en la dimensión z. Además, el error medio de ubicación fue 1.2404 cm, con un tiempo de procesamiento promedio de 18.2 ms por fotograma. Estos resultados demostraron la aplicabilidad de dicho sistema de posicionamiento que se puede implementar fácilmente, por ejemplo, en el campo de aplicaciones emergentes de IoT industrial para la navegación de robots. Además, la fase de seguimiento del sistema se probó con un error medio de 1.07 cm. Adicionalmente, el método propuesto se puede aplicar para cualquier ejecución de seguimiento donde los objetos a ubicar no posean cámaras integradas pero tengan un dispositivo basado en LED. En consecuencia, estos resultados experimentales demostraron que el sistema de posicionamiento propuesto contribuye parcialmente al cumplimiento del cuarto objetivo detallado de esta tesis.

Es importante resaltar que la precisión del sistema de localización propuesto depende de la resolución y el campo de visión (FoV) de la cámara y la distancia entre la cámara y las balizas. Esto se debe a que en cualquier imagen, cada píxel representa una distancia real específica sobre un plano paralelo al plano normal de la cámara, basada en las variables antes mencionadas. Si aumenta la resolución, también aumenta la precisión del sistema. Sin embargo, un aumento en el FoV o una mayor separación con respecto a la cámara disminuiría la precisión de la posición. Por ejemplo, cada píxel de las fotos tomadas durante estos experimentos a una distancia de 2.00 m representa 3.40 mm. Si la resolución de la cámara se cambiara a 1920×1080, cada píxel correspondería a $1,24$ mm. Por lo tanto, en el segundo caso, la precisión de la posición aumentaría notablemente, ya que cualquier error de un píxel conduciría a un error de ubicación de 1.24 mm en lugar de 3.40 mm. Además, la selección y configuración de la cámara durante la implementación del sistema deben tener en cuenta este efecto.

El sistema de WSN para exteriores basado en OCC propuesto en este trabajo se validó con un experimento de campo. Se estableció con éxito un enlace de comunicación de larga distancia, más de 300 m, entre un teléfono inteligente de vieja generación y un dispositivo publicitario basado en LED. A pesar del uso de un umbral fijo para decodificar la señal capturada, la baja calidad del sensor de la cámara, la inestabilidad de la cámara durante las pruebas y las condiciones ambientales adversas (brisa fresca y calima), el sistema alcanzó un BER promedio de $1.388 \cdot 10^{-2}$, y en el peor de los casos un BER de $2.222 \cdot 10^{-2}$. Por tanto, este experimento demostró que una aplicación OCC para IoT en entornos urbanos es posible, cumpliendo con el cuarto objetivo detallado de esta tesis.

Dado que los resultados experimentales mostraron que el esquema de modulación independiente de la distancia propuesto es efectivo, se puede emplear para eliminar el problema del parpadeo en el sistema WSN para exteriores mencionado anteriormente. De esta manera se demuestra la viabilidad de implementaciones prácticas basadas en OCC para IoT en entornos urbanos. La implementación de una WSN para exteriores se puede emplear para monitorear la contaminación ambiental, controlar la variación de temperatura o humedad, monitorear la contaminación del agua o realizar detección temprana de desastres. Por lo tanto, la hipótesis H3 "OCC es una técnica válida para implementar los sistemas de Internet de las cosas en entornos urbanos" ha sido validada al alcanzar los objetivos detallados tres y cuatro de esta tesis.

Chapter I

Introduction

The implementation of smart cities through the application of Internet of Things (IoT) in urban environments is one step for restraining the social, economic, and environmental critical problems that massive urbanization has caused in the last decades. In September 2015, all United Nations Member States signed the "2030 Agenda for Sustainable Development" for pursuing peace and prosperity for people and the planet. As part of this agenda, goal 11 "Make cities and human settlements inclusive, safe, resilient and sustainable" includes diminishing energy consumption and greenhouse gas emissions, the inclusion of sustainable transportation systems, and improving human settlements management. This goal is deeply related to the employment of new technologies and the concept of smarter cities, especially in developing countries.

By definition, a smart city is an urban area that employs devices (general purposes sensors) to collect data and then apply powerful analytic tools to these data to manage assets, resources, and services in the interests of better performance, lower costs, and lessened environmental impact. In this way, the city's operational efficiency increases, and the related information is public, improving the quality of government services and citizen welfare. The future of smart cities' applicability relies partially on today's research, development, and implementation of IoT applications within urban environments. The different sensors used to gather the information can be considered IoT elements that can connect and communicate with other devices over short, medium, and long distances without wires' necessity.

Due to the number of sensor devices that a smart city requires for making accurate decisions, traditional wireless communication links based on Radio-Frequency (RF) become insufficient. This type of communication has two main issues: the actual spectrum saturation and the inter-systems interference based on the extensive use of RF links, so other complementary wireless communication techniques are needed. For example, Intelligent Transportation Systems (ITS) that allows some smart cities' capabilities such as efficient traffic routing, dynamic evacuation schemes, precise public transportation scheduling, relies on the deployment of Vehicle to Anything (V2X) communications, which requires the use of devices pre-installed in the vehicles. Some RF-related solutions have been developed; however, they interact with a significant amount of interference. Similarly, Wireless Sensor Networks (WSN) combined with long-distance communication, enables real-time environmental monitoring and early disaster detection systems. These networks are fundamental for the future smart cities; however, a possible failure of these systems is a critical problem, so its implementation should not depend only on RF links.

Accordingly, for real smart cities applications, the systems should avoid the saturated spectrum portion while offering reliable communication, moderate delay, low jitter, adequate bit rate, and security. It is also essential to take advantage of the technological trends and previous massive deployments to impulse the implementation of smart cities in developed countries, where some pilot cities are already working and in developing countries with economic and technological limitations.

Due to the advantages of Light Emitting Diodes (LEDs), such as energy efficiency, extended life cycles, cost-efficient manufacturing process, and high switching rate, there is a trend in the use of Light Emitting Diode (LED)-based devices for illumination, advertising, and decoration in both indoor and outdoor environments. This tendency especially affects the illumination systems of homes, buildings, streets (public lamps), traffic (new signaling lights), and cars (hazard, tail, sidelights, and so forth). The fluorescent and halogen lamps have been replaced by LED ones as a global initiative for controlling excessive power consumption and reducing climate change. Even developing countries, such as Ecuador, had replaced their main towns' traditional public illumination systems with LED-based devices. Additionally, there is a trend for using LEDs in walls, clothes, and accessories for decoration purposes and deploying new high-resolution displays based on organic LEDs. This massive utilization of LED-based devices impulses the development and implementation of Visible Light Communication (VLC) [1] systems.

VLC is an optical wireless communication technology that works with the visible light portion of the electromagnetic spectrum (430 THz to 790 THz) and transmits data by modulating a light's characteristic, commonly its intensity. Still, some authors are exploring the use of light's polarity and color temperature. The emitters are light sources, such as lamps, screens, or signs, usually LED-based devices, since they can be efficiently and effectively controlled while avoiding the flickering effect due to its high switching rate. On the reception side, photodiode-based equipment is used for sensing the variation on the selected light characteristic. This technology presents several benefits over RF solutions. Due to the use of the visible light portion of the electromagnetic spectrum, VLC is resistant to RF interference without affecting other RF system. In the same way, this emerging technology supports larger bandwidth; and it is more secure than the traditionally deployed wireless systems since light is confined to a specific area. Additionally, its transmitters are usually used for both illumination and communication with low power consumption.

However, the implementation of VLC systems with photodiodes as receivers implies the use of external and potentially expensive devices. For this reason, this study will focus on Optical Camera Communication (OCC) [2], which is a specific kind of VLC-based technique that uses image sensors, for example, cameras, for receiving the signals. In this case, the insertion of devices (smartphones, watches, tablets, or wearables) with embedded cameras in a wide variety of day-to-day activities, combined with the massive implementation of outdoor camera-based security and monitoring systems, opens the opportunity of deploying new communication systems over OCC technologies for IoT applications and services, such as V2X networks, WSN or Indoor Positioning System (IPS).

In general, since OCC employs pre-existing devices for receiving the signal, its deployment is low cost. In the same way, OCC offers immunity to RF interference and takes advantage of the fast development of cameras with higher resolution and better image acquisition speed while mitigates the current spectrum saturation of traditional wireless implementations. This technique also includes the possibility of an infrared upload link for full-duplex communication and the use of spatially separated sources for designing Multiple-Input Multiple-Output (MIMO) systems [3, 4]; two useful features for IoT applications. OCC presents itself as an excellent complementary wireless communication technique for deploying IoT applications. Nevertheless, the use of this technique for implementations within urban environments requires an extended analysis.

At first, the distance between the emitters and the receivers can vary from some centimeters to several hectometers, affecting each transmitter's projection in the acquired image. This issue affects not only the number of pixels in the collected image corresponding to the emitted data source limiting the data transmitted by frame, but it also compromises the meaning of close-emitters interference. To estimate the number of pixels that a light source projects on the image, a set of simple equations should be deduced. In this way, the systems can be designed or adapted easily for the minimum quantity of available pixels' specific constraints. In these links, other light sources interference depends on the proximity in the two dimensions (2-D) projection, even if the emitters are safely separated in the real world. For example, in a system with two identical transmitters separated by more than $10m$, the closer to the receiver has a bigger projection in the image. It can interfere significantly over the other emitter depending on their spatial location about the camera. It is necessary to quantify this interference and then predict its impact over the communication link. For this task, the set of pixel's projected equations is fundamental along with the NPSIR.

Secondly, the considerable variability of the transmitter-receiver distance requires developing a modulation scheme that works properly independently of this separation. Additionally, the modulation should avoid other issues such as the flickering problem, low data rate, excessive overhead, or the necessity of specialized hardware. Finally, a possible application should be tested to validate the implementation of similar systems for urban environments.

I.1 Motivation

This thesis's topic, "Optical Camera Communication for Internet of Things in Urban Environments," was selected based on three main factors: the research group expertise, my academic background, and the potential new research lines for my university in Ecuador.

At first, since the research has been developed within the Photonic Technology and Communications Division of the Instituto para el Desarrollo Tecnológico y la Innovación en Comunicaciones (IDeTIC) at Universidad de Las Palmas de Gran Canaria, the topic follows this group's evolution in the VLC field. They have worked from system's simulations [5] to applications prototyping [6–8] and prove-of-concept implementations [9, 10] with photodiodes at the receiver side. Therefore, the logical next step was to explore image sensors as receivers by using OCC systems. This research area was in progress when I joined the group.

Secondly, I obtained a Master of Science in Electrical Engineering with a concentration in Communications, Control, and Signal Processing from Northeastern University, United States of America (USA). This degree included courses related to multilevel signals, such as image and video, which provided me the required proficiency for working with camera-based communication systems. Additionally, my final master project was about nodes' localization within WSN, assuring my familiarity with a limited local processing power for highly dynamic environments.

Finally, as professor and researcher of the Telematic Engineering Department at Escuela Superior Politécnica del Litoral (ESPOL), Ecuador, one of my responsibilities is to foresee possible research lines and collaborative projects that can contribute to the social, technological, and economic progress of the country under the National Development Plan [11] guidelines. Since IoT applications for urban environments is the base for smart cities applicability, and OCC solutions can be implemented with Commercial off-the-shelf (COTS) equipment, the IoT field with a concentration on OCC is ideal as a potential new research line. Especially because Ecuador's main cities are migrating their general illumination systems into LED-based ones.

I.2 Hypothesis

As it has been exposed, OCC presents itself as a low-cost solution for short distances applications. However, this work pretends to prove the viability of implementing an Optical Camera Communication system for Internet of Things in Urban Environments. Along with the theoretical analysis, laboratory-based testing, and experimentation, this work provides equations for determining the 2-D projection of the objects, quantify the interference of other light sources, and develop a novel flickering-free modulation scheme. This OCC modulation should work adequately for short, medium, and long distances without the necessity of previous calibration or specialized equipment in both indoor and outdoor implementations, becoming the critical element of the future OCC systems for IoT within urban surroundings.

Hypothesis 1 (H1): *OCC close-emitter interference can be characterized for indoor and outdoor implementations.*

Similarly to Signal to Noise Ratio (SNR) in traditional wireless links, the NPSIR determines the relation between a legit emitter and a light source interfering in the communication; while providing an estimation of the maximum Bit Error Rate (BER) related to this interference. Additionally, this value can predict the interference of similar systems by projecting the distance in pixels. Since the close-emitter interference is inversely proportional to the distance between sources, its effect can be mitigated by maximizing this separation as much as possible.

Hypothesis 2 (H2): *OCC systems can be deployed for medium and long distances by using a distance-independent modulation scheme based on consecutive frames relations without the necessity of previous calibration.*

The main problem for implementing a long-distance OCC link is the limited amount of pixels per frame. The projection of close emitters has more pixels than distant sources, so the number of collected samples is greater for the close transmitter. A direct modulation scheme would lose samples from a distant source and require the signal's continuous transmission. However, if both sources are using the same switching frequency, and the receiver is a rolling shutter camera, their projection has similar light bands and the same correlation coefficient over consecutive frames. By exploiting this relation, a distance-independent modulation scheme can be developed. Since this technique is based on direct frames' comparison, the necessity of determining a light "ON" state threshold is eliminated, and therefore the calibration is avoided.

Hypothesis 3 (H3): *OCC is a valid technique for implementing Internet of Things' systems in Urban Environments.*

OCC has been proposed and validated as a solution for IoT implementations, specially for IPS and ITS, of short and medium range. In order to use this technology for systems in urban environments, a long-distance modulation is required. As have been explained previously, such modulation is feasible, and consequently the application of OCC for urban environments is valid.

I.3 Objectives

This work's main objective is to formally evaluate the viability of implementing an Optical Camera Communication system for Internet of Things in Urban Environments. To achieve this goal, some detailed objectives are needed:

1. Determine and experimentally validate the equations for estimating the 2D pixel projection $(x,\ y)$ in a photograph of a real distance $(d_x,\ d_y)$ in function of the separation between the object and the camera (D), the

relative angle of the object (vertical β or horizontal γ), and the camera's specific characteristics.
This estimation is the base for determining the closeness of light sources and the introduced interference. In the same way, these equations approximately calculate the number of pixels projected by the legit emitter, which can be used as a constrain value during the implementation of the distance-independent modulation scheme.

2. Determine and experimentally validate the usability of the introduced NPSIR for quantifying the impact of relative close emitters over the communication link in OCC systems.
   Since NPSIR represents the relation between a legit emitter and a light source interfering in the communication, this value can be used for calculating the maximum BER. Additionally, the quantification of the close-emitters interference within OCC systems is the first step for determining the proposed communication link's performance and then validate its usability.

3. Develop and experimentally validate the flickering-free distance-independent modulation scheme for OCC. This modulation is based on consecutive frames relations for avoiding calibrations.
   A flickering-free distance-independent modulation scheme is one of the critical factors in the feasibility of applying OCC for IoT within urban environments. Moreover, this modulation might avoid overhead, such as calibration headers, while adopting a minor complexity algorithm. By using the comparison of consecutive frames, these requirements can be achieved.

4. Propose viable applications of OCC for IoT within urban environments.
   To prove that OCC is a valid technique for implementing IoT in urban environments, it is required to demonstrate the existence of OCC applications. To fulfill this statement, the proposed applications should be tested at least under laboratory conditions.

I.4 Methodology

For developing this thesis, the inductive-deductive process, known as the scientific method, has been used. At first, the observation was performed as an analysis of IoT applications' and OCC systems' current situation, deployments, problems, and challenges. We focus this inquiry on the collaboration of both technologies. Then three hypotheses related to the adequate operation of OCC and the feasibility of its implementation for IoT were formulated along with four specific objectives. Subsequently, it was predicted that a rough estimation of the number of projected pixels on a frame would be sufficient for designing purposes and to evaluate the interference from other light sources by applying the NPSIR value. Similarly, it was foreseen that the viability of applying OCC for IoT within urban environments depends on the development of a flickering-free distance-independent modulation scheme based on frame comparison. To validate these predictions, a set of simulations and experiments were prepared.

In order to apply this methodology, the research work has been structured as follows:

1. State of the art. In this part, we analyzed the bibliography of OCC papers, focusing on the available modulation schemes, the previous characterization of similar systems, the proposed applications of this technology, and the limitations for applying these solutions for IoT. At this point, the well proved VLC modulation schemes are also analyzed to check if they can be adapted for OCC implementations. In the same way, the deficiencies of the current modulations, characterizations, and proposed applications of OCC are highlighted to define the characteristics that our solution should present for giving an improvement in terms of data rate, distance range, processing time, or implementation cost. The information obtained from reviewing the current works can be seen in chapter II.

2. Theoretical fundamentals. In this part, we present and analyze the basic concepts of OCC, including the cameras' operation and close emitters' effect over the communication link. This study is the foundation for pointing possible modulations out and validates the hypothesis 1. The detailed information is included in chapter III.

3. Solution development. This part is a continuous improvement process required to interact with the "Validation" and the "Results' Analysis." A modulation, including a synchronization phase, is proposed considering how cameras acquire images and the possibility of image distortions due to external factors, such as environmental light or relative motion. Additionally, some viable applications of OCC systems for IoT in urban environments are also presented. In this way, the introduced scheme assures the Validation of hypothesis 2 and 3. The developed solution is shown in chapter IV, while the viable applications are presented in chapter V.

4. Validation. Experiments verify the proposed modulation scheme and viable applications. We compare our modulation with the available solutions in terms of throughput, BER, and maximum distance, while the applications are contrasted with similar services in terms of accuracy and processing delay. Similarly, the developed equations for measuring in pixels the actual distances projected into images and quantifying the close-emitter interference are validated by a set of trials and a system simulation. The experimental and simulations set up along with the corresponding results are presented in chapter V.

5. Results' Analysis. The validation part results are analyzed to define which elements of our solution work properly and which modules require redesign or change as part of the continuous improvement process. Finally, the whole solution is evaluated for demonstrating that the objectives were reached. This analysis is the base of the "Conclusions and Future Work" section.

This work is divided as follows: chapter II presents the State of Art in OCC characterization, applications, and modulation schemes. It presents a review of OCC bibliography focusing on the key elements for urban implementations. chapter III introduces the theoretical framework of image acquisition and 2-D projections, fundamental for validating the proposed modulation scheme. The analysis of close emitters interferes is also shown in chapter III, where the NPSIR is defined as a tool for determining the BER boundary of an OCC link. In chapter IV, the novel modulation technique is formally introduced, including the proposed synchronization scheme and the constrain for the frequency selection. The simulation of an indoor WSN as a possible IoT application, along with the lab-test and experiments of outdoor communication links for WSN implementations, and the experimental validation of the equation set for 2-D projection are detailed on chapter V. In this section, the simulations and experiments for validating the proposed modulation scheme are also presented along with the results. Finally, in chapter VI, the conclusions of this work can be found.

Chapter II

Optical camera communication: present, challenges and trends

Since OCC is a relatively new technique, there are several open research fields and challenges related to its research, deployment, and implementation [4, 12]:

1. Characterization of the communication channel, including turbulence, fog, rain, snow, and so for.
2. Characterization of interference effect over the communication performance, including the impact of external interference and close-emitters interference;
3. Analyze the effect that the image acquisition characteristics (shutter type, exposition time, distortions) could have over the data decodification;
4. Development of a viable uplink, with adequate data rate without additional infrastructure or interference to the systems.
5. Implementation of MIMO systems by using multiple access techniques, such as Spatial division multiple access (SDMA).
6. Development or adaptation of modulation, coding, and error detection schemes for allowing better data rate or more extended link range.
7. Adaptation of image processing techniques for improving communication reliability.
8. Development and implementation of striking applications for this technology.

However, some open research lines contribute marginally to the analysis of implementing OCC systems for IoT applications in urban environments. For example, the development of a viable uplink is not critical in such deployments. The main goal of the IoT applications on urban environments would be the collection of data. Therefore unidirectional links could satisfy this objective eliminating the necessity of studying the feasibility of potential uplinks temporally. Similarly, the implementation of MIMO systems and adaptation of image processing techniques for enhancing the communication can be neglected in the first stage of research. However, in future works, all these issues should be considered.

On the other hand, the study of the communication link's characterization and the analysis of the possible issues that the image sensors characteristics (shutter type, exposition time, distortions) can produce over the data decodification are fundamental for deploying adequate OCC implementations. Similarly, a deep study of currently proposed modulation techniques should be included to verify the viability of employing OCC for outdoor long-distance links. Finally, the analysis of OCC striking applications and their viability in smart cities is required.

II.1 Optical camera communication characterization

Since OCC systems are based on VLC, they use signals within the visible light spectrum, while image sensors perform the modulated light's reception. Therefore, there are specific interfering sources that should be analyzed. Among them, weather conditions, image distortions, solar radiation, and other light sources constitute the main problems for OCC systems.

The impact of climate conditions over VLC systems' performance has been studied. In this sense, the effect of snowfall was simulated in [13], showing that the attenuation and the time variation of the received signal should not be neglected. This influence mainly depends on the snowflakes' size distribution due to Fresnel diffraction. In [14], the influence of rainfall in VLC links was analyzed. Since the data is transmitted through an optical signal, the received power diminished according to the rain rate. The emitted light beam is scattered when it hits a raindrop. In this paper, the rain rate was defined as the number and size of raindrops during a specific time. Besides, the attenuation introduced by fog in Free-space optical (FSO) communications was studied in [15], showing that it can be predicted according to visibility scenarios without using heavy computer codes. These channel modeling research works were based on photodiode receivers.

Nevertheless, Ashok *et al.* [16] studied the effect of distance over multi-element receivers, such as cameras, using a photodiode array. The authors modeled the reception according to the distance. When the separation between emitter and receiver increases, the number of pixels representing the LED in the frame decreases, and the critical distance is reached when the emitter generates a one-pixel projection. Then the viewing-angle dependency was characterized in [17]. This work showed a direct relation between this angle and the SNR of the communication link. However, no formal equation was presented. In the case of image distortion, the works related to image sensors are not recent. The potential distortions due to optical turbulence were studied in [18, 19], while the effect of lens aberration was analyzed on [20]. In both cases, the research did not consider data transmission, only image generation.

The study of self-interference in OCC as a performance degradation factor has been addressed in [17] and [21]. However, the relation between the light wavelength and the impact over the transmission has not been discussed. In this topic, the characterization of vehicle to traffic light communications assuming that the link is affected only by background solar radiation (for yellow, red, and green) and artificial light sources (lighting and advertising), excluding close emitters from the same system was presented in [22]. Some practical issues related to using multi-LED transmitters with chromatic modulation were addressed by [23, 24] for OCC, but only the viewing angle's distortion was used as a critical parameter. Finally, Hong and Chen [25] presented the effect of mobility on the performance of these systems using photodiodes as receivers. It was shown that the system performance depends on the speed; if the users move faster, the packet loss increases.

II.2 Internet of things' applications

Nowadays, different devices, such as smart-phones, wearables, and tablets, have embedded cameras that can be easily used by people of all ages in a wide variety of day-to-day activities. Additionally, the use of LED-based lamps and screens has been globally extended, not only for indoor and outdoor illumination but also for signaling, advertising, and decorative purposes. These two key factors together open the future for the deployment of communication systems based OCC [2] different IoT applications, such as positioning, tracking and navigation, motion captures, ITS, and WSN.

II.2.a Positioning, tracking and navigation

The increasing trend of implementing location-based services and applications (e.g. indoor navigation or opportunistic marketing) requires more accurate IPS. However, Global Positioning System (GPS) is not an accurate option for indoor localization [26]. Alternative solutions based on Wireless Fidelity (WiFi), Bluetooth, RF, Ultra-Wide Band (UWB), Infra-Red, and VLC have been proposed [27, 28]. Among all these techniques, VLC [1] provides high position accuracy, energy efficiency and can be easily and almost inexpensively implemented, while offering immunity to traditional RF interference. VLC takes advantage of the promoted replacement of conventional lighting systems with LED-based devices and the introduction of these elements for decoration purposes.

Visible Light Positioning (VLP) techniques can be classified in several ways. In [29], these techniques were separated into two main groups: direct positioning and two-step localization. The direct positioning techniques are usually highly complex and lead to optimal solutions without previous parameter estimation [30, 31]. The two-step localization relies on the first stage for data extraction, which is then used for estimating the position in a less complex second stage that gives suboptimal results [32, 33]. Based on this analysis, a real-time IPS should be implemented as a two-step localization method to avoid high data storage requirements, computing-intensive algorithms, and high computational delays. Another VLP techniques classification was presented in [34], where the methods were divided into five groups: proximity, fingerprinting, triangulation, vision analysis, and hybrid algorithms. The proximity [35], fingerprinting [36, 37] and triangulation [38–40] methods use photodiodes as receivers, and require a multiplexing process. While vision analysis techniques use cameras as receivers and do not need the multiplexing stage. However, the hybrid algorithms [41, 42] use photodiodes or cameras as receivers, and the multiplexation is optional. However, the photodiodes are susceptible to the light beam direction, limiting their use with mobile objects. While the image sensors can spatially separate light sources and cameras with better characteristics (resolution and frame rate) have already been included inside buildings for security reasons. Therefore, the vision analysis VLP techniques should be exploited.

In 2012 a specialized device that determines its 3D location based on trigonometric calculations using two embedded cameras and four external beacons was patented [43]. The beacons' position and the distance between the cameras were known, so the device's central point, corresponding to the object's 3D location, was calculated by comparing the captured images. Luxapose, an VLP system introduced in [44], calculated the smart-phone position based on scaling factors using its camera and beacons, each one with different frequencies. This positioning algorithm reached an average location error of 10 cm. In [45], the use of neural networks for avoiding complex mathematical models in the translation from real-world distances to images pixels projections was proposed. This approach reported an error of 1 cm at a distance of 10 cm but increased to 20 cm at 2 m, and consumed computational resources and time. The VLP proposed in [46] used wearables with embedded cameras (e.g., smart glasses, watch) and polarized the beacons. Then, the lights' orientation and location were extracted from the camera's video, and the device's position was calculated by implementing an Angle of Arrival (AOA) algorithm. The average location's error was 30 cm with a 1.8 s delay working at 300 MHz. In [47], the location of the device independently of the receiver orientation was done based on the camera and the accelerometer. In this case, a rotation matrix based on the accelerometer's information is applied to the set of quadratic equations that represent the real world positions projected over the photo. The average location's error was 10 cm, even with noise reduction in the frames.

The VLP technique proposed in [48] used the camera, accelerometer, and gyroscope embedded on the smart-phones for finding the location and orientation of the mobile device. A low-complexity singular value decomposition-based sensor fusion algorithm was used to enhance the positioning accuracy with the sensors' data, and the mean positioning error was reduced to 4.4 cm. An indoor VLP experimental demonstration using image sensors was presented in [49], the camera's position was determined from the geometrical relations of the LEDs in the images. These devices continuously transmitted their coordinates using Undersampled Phase Shift Keying (UPSK) modulation. The mean position error was 5 cm for a distance of 1.20 m, and it increased to 6.6 cm for a height of 1.80 m. This method was improved in [50] by grouping the LEDs into blocks with a single coordinates' emitter and implementing a backpropagation Artificial Neural Network (ANN) for a roughly and precise direct estimation of the position. In this case, the mean positioning error was reduced to 1.49 cm for a height of 1.80 m with an online processing time of 0.15 s.

In [51, 52], the authors present a two-step 3D indoor positioning system using OCC. This system establishes the position and tracks several devices' movements simultaneously, based on the trigonometric relations between the camera and a beacon's virtual plane. Instead of locating an embedded camera device, the usual paradigm of OCC 's VLP techniques, this system employs a single camera for positioning different objects based on the identification of static beacons which location is previously known. Its implementation is low cost: the items to be located and the beacons use inexpensive LED-based devices, while the receiver is a pre-existing security camera. This method showed a mean location error of 1.24 cm with an average process time of 18.2 ms per frame for four simultaneous targets, at a distance of 2.00 m, demonstrating the viability of such application.

II.2.b Intelligent Transportation System

Since nowadays the vehicles are equipped with cameras and LED-based car lights, OCC is suitable for implementing ITS presenting several advantages over other wireless communication systems [53]. At first, OCC provides a less interfered communication link with perfectly separated light sources over the focal plane, providing spatial separation. Additionally, the LEDs' location can be extracted from the received image, allowing light sources' identification. In this way, the meaningful pixels from legit emitters are focused while the other sources are discarded. For deploying V2X communication links, the cameras can be used for receiving optical signals from traffic lights, nearby vehicle headlights, brake lights, and signage. However, ITS implementations using OCC technology require high-speed frame capturing and data extraction for assuring flicker-free solutions. In this sense, some experimental implementations [54–56] have used high-speed camera (up to 1000 fps) for data transmission of 10 Mbps with less than 10^{-3} BER at a distance of 45 m. Nevertheless, the same data transmission with $1.14 \cdot 10^{-4}$ BER for uncoded data was achieved in [57] by using a commercial camera (15 fps). However, in this case, the implementation was tested at a distance of 2 m. Similarly, the system proposed in [58] used a 30 fps camera for the numerical simulations. A 15 kbps link with 10^{-2} SER was obtained for 75 m with direct communication and presented the use of a relay vehicle for achieving longer distances. Similarly, in [59, 60], the authors present implementations with a 120 fps micro camera with selective capturing for speeding up the acquisition process (up to 435 fps). During the experimental validation, the communication link achieved 6.912 kbps with 10^{-5}BER for a distance of 1.75 m.

II.2.c Wireless sensor networks

The use of pre-existing cameras-based infrastructures, such as traffic camera networks or security systems, is a valid method for decreasing the implementation costs of OCC deployments. Additionally, the use of spatially separated sources allows the design of MIMO systems [3, 4], which can increase the transmission data rate of OCC systems.

The use of the visible light band for communication links in smart cities applications has been proposed previously. For example, Kumar [61] presented a public illumination system of a smart city that can be used for ubiquitous communication, assuring a broad coverage. However, the work was limited to public LED lamps, leaving aside attractive possible emitters, such as traffic lights or advertising screens, and only cover modified devices as receivers and high-speed communication links. In newer works [62], the traffic lights and car lights have been studied as potential transmitter devices, but only for MIMO inter-vehicular communication solutions with a short distance range. A long-distance OCC system has been proposed in [63], but only for rolling shutter cameras with a maximum distance of 2 m. In [64] a real long-distance OCC system, above 300 m, for slow data rate applications in smart cities is introduced. This system was proposed for Wireless Sensor Networkss (WSNs) to transmit low load data periodically. The implementation used pre-existing infrastructure over heterogeneous networks, reducing the deployment cost. However, this solution does not address the flickering problem.

II.3 Modulation's schemes

Several modulation schemes for OCC have been proposed and can be mainly divided into four categories: based on On-Off Keying (OOK), polychromatic modulations, undersampling techniques, and based on space-time coding.

II.3.a Modulations based on OOK

At first, the researchers adapted the OOK modulation directly from VLC [65] with Nyquist sampling. The LED 's switching frequency is half the camera's frame rate, and two consecutive frames are required for representing each symbol to avoid stripes with uncertain states. This method's implementation is simple; a test with high-speed cameras (600 fps) was performed, reaching a data bit rate of 150 bps. However, it involves specialized hardware and a synchronization stage. Due to this, in [66], an asynchronous OOK is presented, improving the data bit rate. For this modulation, three consecutive frames represent two bits, and two frames are selected, as shown in figure II.1, eliminating the synchronization delimiters necessity. This technique reaches a data bit rate of 20 bps for 30 fps cameras, but the light flickering problem was not considered. Later on, the authors improved this asynchronous technique [67] by using a dynamically adaptive threshold for speeding up the transmission and increasing the LED pulse rate for mitigating the flickering problem. This modified method achieved a 1900 bps link rate but only for a distance of 0.2 m.

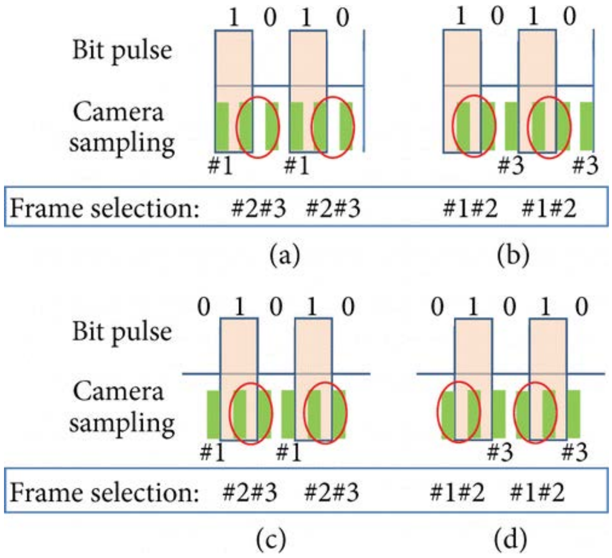

Figure II.1: Asynchronous OOK scheme for optical camera communication [67].

Similarly, the flickering problem was mitigated in [68], by combining OOK modulation with Manchester codification, as defined in IEEE802.3. In this case, they use the camera's rolling shutter effect for representing several bits per frame. The data bit rate is improved up to 3100 bps for 20 fps cameras. The implementation of this method requires Complementary Metal Oxide Semiconductor (CMOS) cameras, synchronization, and additional image processing. Due to these restrictions, this modulation does not tolerate environmental noise or distances greater than 1 m between devices, and the average transmission delay is 3.9 s. Rajagopal *et al* [69, 70] introduce a binary Frequency Shift Keying (FSK) scheme, which two frequencies are separated by 200 Hz to avoid possible inter-symbol interference. This modulation supports several transmitters due to the implementation of Frequency Division Multiple Access (FDMA); each emitter uses a different pair of frequencies. This modulation solves the light flickering problem since the LEDs are switching above 2000 Hz for sending each bit. The experiments performed with a 30 fps camera showed a data transmission rate of 10 bps per source and up to 29 concurrent LED-lamps. However, this technique requires a synchronization delimiter with a flag and a pilot signal for each transmission. Later on, Lee *et al* [71] took advantage of the rolling shutter effect and developed a modulation scheme by assigning different frequencies for each symbol from a predefined cluster depending on the camera's characteristics. To mitigate the devices' synchronization problem, the researchers added a fixed frequency splitter before each symbol and a parity symbol. In the same way, two delimiters are attached, one at the beginning and one at the end of the communication, for minimizing the transmission localization complexity. This scheme reached 96 bps with a 30 fps camera but required Line of Sight (LoS) and only works for short distances, less than 1 m. On [72], the authors combine OOK modulation with Manchester codification and dynamic thresholding for rolling shutter cameras to increase the data rate of the system while avoiding the blooming effect. In this case, a second-order polynomial fitting was used for determining the threshold in each packet transmission, minimizing the overlapping row's exposure time. By applying this dynamic threshold, the system can adapt to possible environmental noise but requires extra header bits, and the demodulation process is more complex than previous solutions. The experimental results using 30fps cameras showed a 1680 bps data rate with 10^{-3} BER for 60 bits payload and 1500 lux uniform illumination. In [73], the same dynamic thresholding, modulation scheme, and codification are applied to a MIMO system based on Red, Green, and Blue (RGB) transmitters and smart-phones receivers. The experimental results presented mitigation of the Inter-channel Interference (ICI) and a successful retrieve of the three channels, where the blue channel performed the best results with less than $3.8 \cdot 10^{-3}$ BER. Despite these results, the system only worked properly for short distances, less than 0.1 m. For improving the performance and distance range of OOK, Li *et al.* [74] proposed the application of image processing in the receiver. Using histogram equalization and image filters over each received frame, area outside the light source that also contained data was recovered, and therefore longer distances were achieved. For experiments with a mobile phone camera, a 0.4 m communication link was established with $2.14 \cdot 10^{-2}$ BER for 2000 bps, but the complexity of the system was increased significantly.

In [63], the authors enhanced the OOK modulation by applying adaptive thresholding (Bradley algorithm) based on changing groups of n pixels where the threshold T_i is calculated as the average pixel value of the n pixels with center in i. Additionally, this paper introduced the novelty of a Not Line of Sight (NLoS) system testing the algorithm with the floor's reflection. The experiments showed a 2 m link working at 68 bps with less than 10^{-2} BER while adding 1.89 ms to the process for each packet. However, all the packets require to be transmitted twice with a 12 bit header, decreasing the throughput.

II.3.b Polychromatic modulations

Several authors work with polychromatic systems using modulation schemes based on Color Shift Modulation (CSK). Chen *et al* [75] presents a basic 4 color CSK modulation, see figure II.2 that reached a 240bps data rate for a 30fps camera while allowing multiple receivers by using Code Division Multiple Access (CDMA). Nevertheless, this method require multi-LED transmitters and its range is less than 1m.

In the same research line, Hu *et al* [76] introduce a high level constellation modulation: 8-CSK, 16-CSK and 32-CSK, see figure II.3. The best results were obtained with the 16-CSK, a data rate of 2400 bps for a 120 fps smart-phone camera. However, this method needs a synchronize delimiter in the OOK 's header and a periodic calibration packet during the transmission. Additionally, its implementation requires high-tech devices due to the computational resources

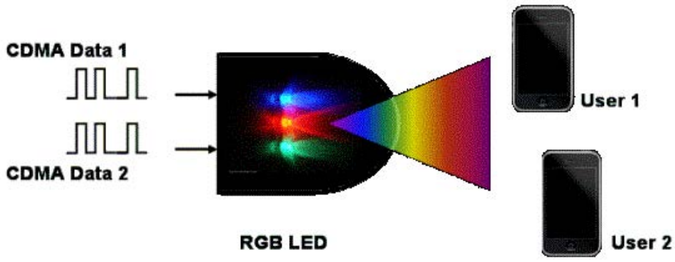

Figure II.2: Color-shift keying and code-division multiple-access transmission for RGB-LED visible light communications [75].

needed for complex image processing. And the authors introduced white light frames, based exclusively on ten volunteers' perception, for avoiding the flickering issue.

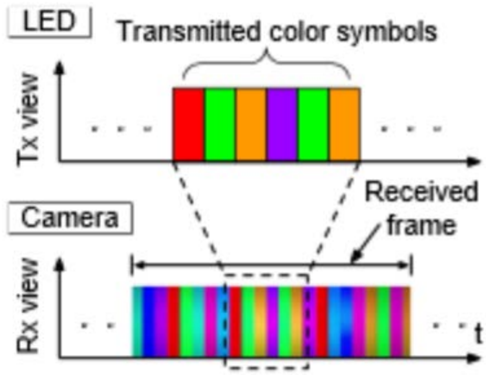

Figure II.3: ColorBars: CSK for optical camera communication [76]

In [46] the authors define their technique as Binary CSK. Instead of modulating the light intensity, they changed its polarization and applied a dispersion film, so the receiver perceives the polarization as two different colors for avoiding the angle dependency. This solution solves the flickering problem and improves the transmission range up to 10m with a slow data rate (14 bps) for 30 fps devices, but require modifications on the receivers. The solution proposed in [23, 24] is an asynchronous CSK scheme in which the data rate reached up to 2400 bps for devices with 120 fps. However, it only works for distances under 1 m. Another modulation based on changing the color of the light is the Generalized Color Modulation (GCM) [77, 78]. This scheme is similar to CSK, but different color constellations are created to achieve a specific target color, not only the traditional white light, working in the CIELUV space instead of CIE1931. Its implementation demonstrated a link range of 75 m without the necessity of sending a reference to the target color. The use of several target colors allowed a multiplexation and increased the data rate. Nevertheless, the packets require two delimiters, header, and verification bits, decreasing this method's throughput. Additionally, the information was split into m-bits symbols represented by 2^m specific colors; more than eight colors are not recommended due to the complexity of the involved decoding process.

Recently, in [79], an 8-CSK modulation was presented along with a beacon jointed packet reconstruction scheme. This scheme reads the signals bidirectionally during the demodulation process. In this way, the transmitted packets can be longer, and therefore the data rate is increased. In this paper, the authors introduced the "pixel efficiency", a data-rate evaluation method based on the rolling shutter effect. The pixel efficiency is defined as the horizontal resolution divided by the total data per frame (pixels-per-bit.) Then for a higher data rate, each bit should be represented with fewer pixels. The proposed modulation scheme had a pixel efficiency of 3.75 pixels per bit, a data rate of 8.64 kbps, and an average BER below $3.8 \cdot 10^{-3}$. However, the system's distance range is limited (less than 0.05 m) and requires the transmission of a reference signal for calibration.

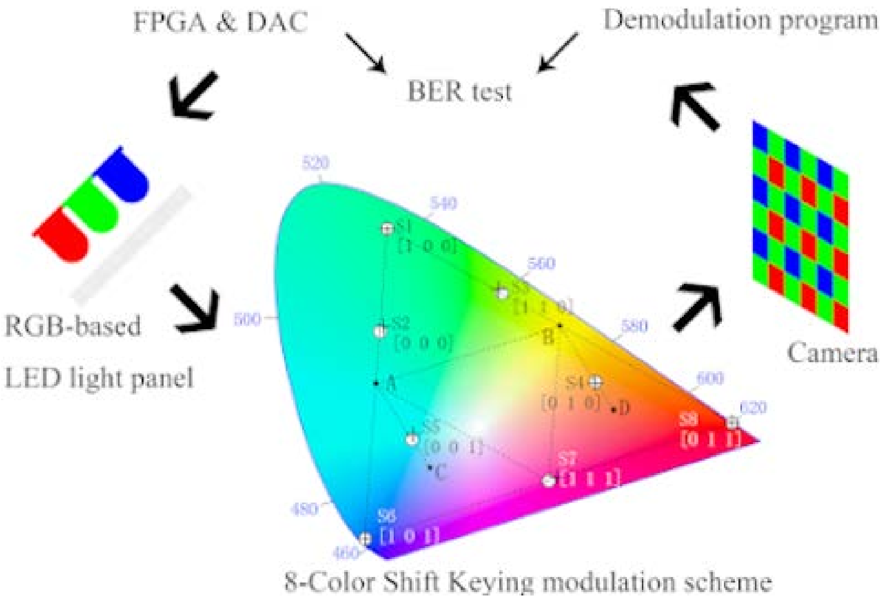

Figure II.4: Color-shift keying (CSK) for optical camera communication using rolling shutter mode [79].

II.3.c Undersampling modulations

The modulation's schemes based on undersampling transform the data signal into a passband signal used for switching the LEDs with a higher frequency. Depending on the applied shift keying, they are classified in: frequency, phase, and amplitude shifting.

In [80] the Undersampled Frequency Shift On-Off Keying (UFSOOK) modulation was introduced, using one specific frequency for each state (one or zero). The selected frequencies were greater than 100 Hz for avoiding the flickering problem and a multiple of the camera's frame rate for assuring synchronization. Two consecutive frames represent each sampled bit; if the value is the same, the data is a zero; otherwise, it is a one (see figure II.5.) Therefore the data rate of this method is half the camera's frame rate. In the same way, Le *et al* [81] defined the two subcarrier frequencies as the discrete sampling of the camera's frame acquisition speed but taking into account the shutter speed as an additional limitation. The authors focus their research on the shutter speed's impact over the system's throughput, showing that longer shutter times reach fewer bits per second for the same frames per second.

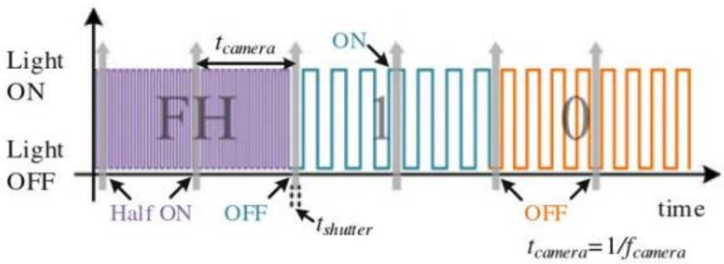

Figure II.5: Undersampled frequency shift on-off keying (UFSOOK) [82].

In [83], Luo *et al* presented the idea of shifting the phase instead of the frequency, avoiding the flickering while representing each 3-bit symbol with one frame. The authors used two phases (one for bit ”0” and one for bit ”1”) separated by 180°, so the bits' representations are complementary: ON-OFF and OFF-ON. Since the chosen frequency is a multiple of the camera's frame rate, the two light states (ON and OFF) of each bit are always obtained, and the demodulation requires knowing how the primary bit ”1” was represented, see figure II.6. This technique, known as Undersampled Phase Shift On-Off Keying (UPSOOK), increased the data rate to three times the camera's frame rate while reaching distances up to 12 m. However, it needs a synchronization delimiter and the transmission of a bit ”1” to properly define the system demodulation logic, increasing the system complexity while decreasing its throughput.

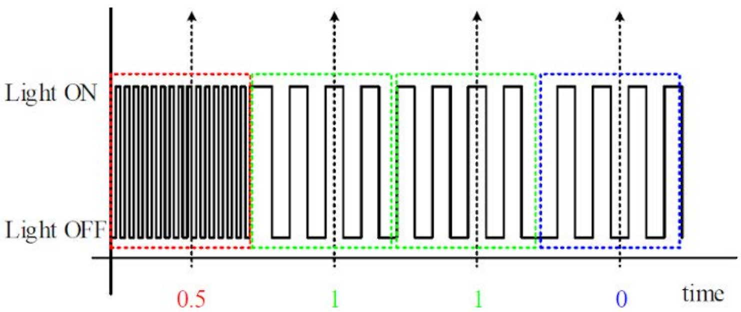

Figure II.6: Example of undersampled phase shift on-off keying (UPSOOK) [83].

Similarly, these authors proposed the change of the light amplitude with the modulation [84, 85]. By modulating the light intensity, the flickering problem is avoided since the light never turns off completely. This Undersampled Pulse-amplitude modulation with Subcarrier Modulation (UPAMSM) system used the Gray codification for improving the data rate, reaching up to five times the camera's frame rate [84]; and employed an RGB emitter with a MIMO implementation for longer distances, extending the link to 60 m with less than $3 \cdot 10^{-3}$ BER at three times the camera's frame rate [85] (figure II.7). Nevertheless, this method demands the transmission of all intensity light levels in a predefined order for the demodulation process when a new communication is established, decreasing the throughput.

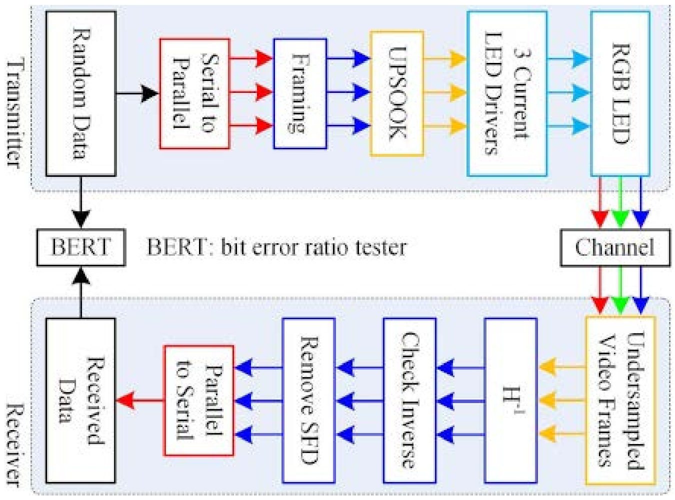

Figure II.7: RGB undesampled pulse-amplitude modulation (UPAM) [85].

Consequently, these authors improved the UPAMSM [86] by using a Quadrature Amplitude Modulation (QAM), which I and Q components were the originally proposed modulation technique. This QAM optical camera communication system double the data rate of their previous work, but the implementation requires two transmitters, and its performance degrades significantly for distances greater than 1.5m. Additionally, since this method used several light intensity levels (ten in the experimental validation of this work), a compensation of the camera's gamma correction is obliged to perform. The corresponding curve is determined from the intensity levels transmitted in the header, aggregating processing time, and complexity to the system. An Undersampled Differential Phase Shift On-Off Keying (UDPSOOK) technique was presented in [87] for mitigating the phase uncertainty problem of the previous UPSK-based modulations. In this case, the signal is transmitted by controlling the phase of two consecutive samples; the signal shifts the phase 180° in the second frame for sending a bit "1" while the use of the same phase represents a bit "0. Since the demodulation is based on this difference, the method avoids the headers' transmission for determining the camera's sample phase. The results showed a 0.5 m link with $6.08 \cdot 10^{-5}$ BER and a 1 m link with $1.88 \cdot 10^{-3}$ BER at 23.02 bps. Nevertheless, the BER increased significantly with the distance.

Finally, in [88] a two-level non-flickering modulation, called undersampled pulse width modulation (UPWM), is presented. In this case, the Pulse Width Modulation (PWM) is combined with the Undersampled Pulse-amplitude modulation (UPAM). The PWM signals modulate the LED 's brightness levels by changing its duty cycle instead of the frequency, while UPAM mapped the bit's stream onto an m-ary amplitude modulation constellation before modifying its amplitude. Therefore, the UPWM maps the binary data onto an m-ary duty cycle constellation that is used for generating the PWM signal, as shown in figure II.8. The experimental results for a distance of 1 m showed a BER of $6.76 \cdot 10^{-4}$ for a modulation order of 32-PAM, while no error was registered for the basic 2-PAM. However, the authors reported that nine frames were dropped due to lost data for the 2-PAM case. This modulation scheme presents BER values below the Forward Error Correction (FEC) limit ($3.8 \cdot 10^{-3}$, but its complexity is high white the distance range is restricted to close by communications.

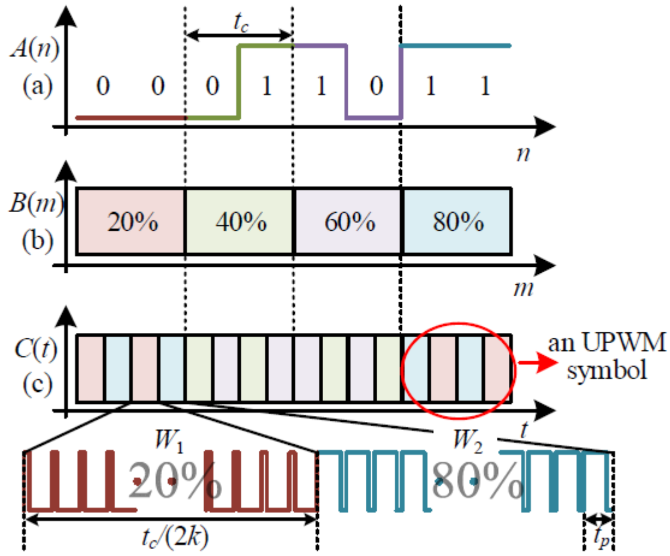

Figure II.8: Undersampled pulse width modulation (UPWM). [88]. **(a):** binary data to be transmitted; **(b):** duty cycle for the transmission of each 2-bits symbol; **(c):** UPWM waveform: W_1 is the first PWM segment with the corresponding duty cycle (20%), while W_2 is the second PWM segment with the complementary duty cycle ($100\% - 20\% = 80\%$)

II.3.d Modulations based on space-time coding

For ITS applications, Amano *et al* presented a space-time coding [89] based on the modified Alamouti code [90] which avoid the use of negative signals. For short distances where each LED is represented by at least 1 pixel, the demodulation is simple. However, longer distances require extra information and processing for matrix reconstruction. The authors employed a preamble of 26 frames with baker sequence for giving relative LED location. Since the pair of space-time codes are transmitted independently by known LEDs of the matrix, the reconstruction is possible based on statistical decisions. During the validation, a 48 m link with less than $1 \cdot 10^{-5}$ BER was achieved but at 50 m the BER increased up to $2 \cdot 10^{-2}$ BER.

For improving this method, Ebihara *et al* [91] introduced a layered space-time coding: the $2^n \times 2^n$ matrix is divided into four submatrices $2^{n-1} \times 2^{n-1}$ where the diagonal matrices represent the first layer bitstream and the anti-diagonal are divided recursively into four blocks for the upper layer's bitstreams. See figure II.9. Since the pixels projected on the image are less than the original number of LEDs, demanding image processing techniques are needed for bipolar interpolation purposes. The experimental demonstration used a 8×8 LED matrix, where a OOK modulation was applied on each LED, as the transmitter and a high speed camera (1000 fps) as the receiver. As a result, a 1 kbps link was established for 210 m with $3 \cdot 10^{-1}$ BER using maximum resolution and a 3-layer bitstream.

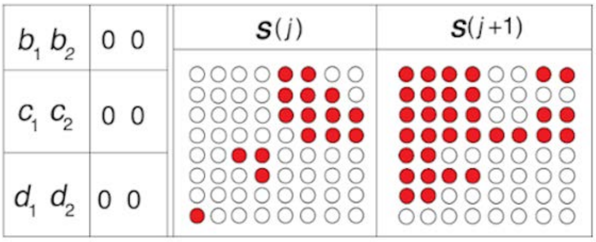

Figure II.9: Example of three-layered STC matrix mapping of the 8×8 LED array for $[b_1, b_2] = [0, 0]$, $[c_1, c_2] = [0, 0]$, and $[d_1, d_2] = [0, 0]$. [91]

Similarly, Masuda *et al* [92] presented a layered space-time coding for spatial modulation with different interpolation techniques. The experimental implementation of this method also used a 8×8 LED matrix and a 1000 fps camera. The system could send data successfully over a 240 m link, but only 3 bits were decoded for this distance. Both methods required specialized software and hardware and the complexity of the demodulation process increased the transmission delay.

II.3.e Other modulations

Outside these four main categories, some proposed modulations deserve to be analyzed. Recently, Chow *et al* in [93] proposed an RGB Undersampled Modulation (USM) based on Undersampled Frequency Shift Keying (UFSK) and OOK signal for data transmission which compares two consecutive frames. Each packet started with a high data rate header perceived as a "half-ON" state for synchronizing the transmission. For each frame, only one band is analyzed per color channel and classified as "ON" or "OFF" state; if two consecutive frames have the same state, the transmitted bit is "1" otherwise is "0". Therefore, the data rate is half the camera's frame rate for each channel. The experimental results showed the implementation of a 100 m link with $3.8 \cdot 10^{-3}$ BER and a 60 m link with less than $1 \cdot 10^{-5}$. However, the threshold definition and calibration are critical problems, and the variable camera's frame rate. In [94], the authors solved the frame rate variability by applying a similar FSK scheme over two transmitters. The second emitter's signal is a 90° phase-shifted version of the original FSK waveform. In this way, the receiver selects the best emitter for each communication process, avoiding a possible reception problem due to frame rate variation. A $1.7 \cdot 10^{-3}$ BER communication was achieved for a 160 m link with a bit rate of 50 bps. Nevertheless, the thresholding and calibration issues were not taken into account.

In [95] a differential modulation for MIMO space-time division multiplexing is proposed for LoS and NLoS communication paths. The emitters are spatially separated over the ceiling (spatial division), and they are divided into g groups that can transmit data over a specific time slot (time division). Due to this space-time division and the application of frame subtraction and masking, data from different sources can be recovered even with an optical footprint's overlap. The signal is differentially encoded using the module-2 addition of the current packet ($b_{k,l}$) and the previous encoded packet ($x_{k-1,l}$), assuming that the first packet is zero ($x_{0,l} = 0$). The experimental results showed a 10 m links with $1 \cdot 10^{-3}$ BER. However, in addition to the N_d bits of payload, each packet has N_p bits of preamble, the group identifier, and the transmitter location (mask). Therefore, the system's overhead increased, although the method complexity is moderate.

A two-dimensional Orthogonal Frequency Division Modulation (OFDM) screen scheme for OCC is proposed in [96]. In this case, a single screen is divided into cells within the code area for allowing MIMO implementations. The structure of the spatial code (See figure II.10) supports 360° rotation (rotation tracking corners), asynchronous communication, frame rate variation, and perspective distortion's correction (Clock cells). Each code cell contains an OFDM symbol created by applying the inverse fast Fourier transform to a two-dimensional Hermitian matrix containing the data. During the experimentation, a 50 kbps link with 10^{-5} BER was achieved for 4.5 m. Nevertheless, the complexity of this scheme is high

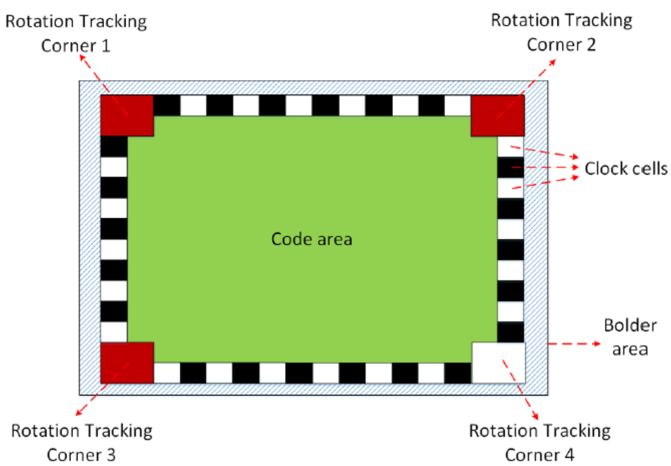

Figure II.10: 2D-OFDM for optical camera communication. [96]

II.3.f Modulations' comparison

In general, the OOK-based modulations are low complexity techniques that work correctly with moderate data rates exclusively for short distances. Therefore, this type of OCC modulations can be used for specific IoT applications within the range of 5 m, which support a low data rate. Since the polychromatic modulations take advantage of the RGB channels for simultaneous transmissions, the data rate increases. However, the achieved distance is short, and the system's complexity is moderate for CSK and high for the CIELUV space. Nevertheless, the polychromatic version of other modulations showed better results in terms of data rate and should be considered. The undersampled techniques provide the fastest transmissions rates with moderate to high complexity and medium-range distances. The modulations based on space-time coding reach long distances with relatively low data rate and very high complexity. Since the proposed implementations require specialized hardware for too complex processing, these techniques are not suitable for smart cities in developing countries. Finally, in all the cases, the modulation schemes that compare consecutive frames reach the most extended distances with moderate complexity. Figure II.11 summarize the analyzed modulations schemes in terms of complexity and distance range.

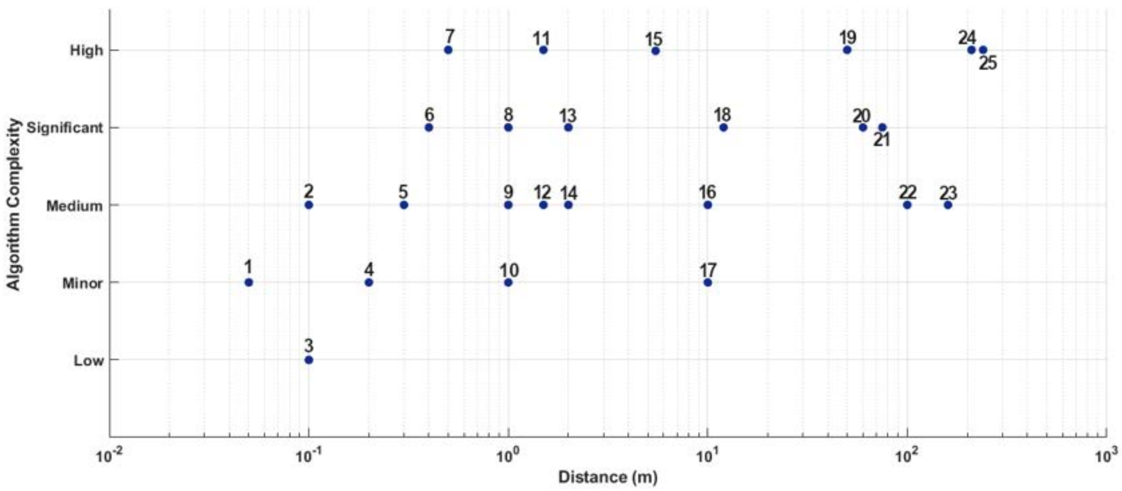

Figure II.11: Optical camera communication's modulations schemes distributed by complexity and distance Range. **(1):** High Level CSK; **(2):** OOK-MIMO; **(3):** OOK and asynchronous OOK; **(4):** asynchronous OOK with dynamic thresholding and OOK with Manchester coding and adaptive thresholding; **(5):** UFSOOK; **(6):** OOK with DSP; **(7):** CSK with DSP; **(8):** UPWM; **(9):** OOK with Manchester coding, CSK, asynchronous CSK, and UDPSOOK; **(10):** FSK and FSK with fixed frequencies; **(11):** QAM-UPAMSM; **(12):** UPAMSM; **(13):** 2^n-CSK; **(14):** OOK with dynamic thresholding; **(15):** 2D-OFDM; **(16):** ST-code with MIMO; **(17):** binary CSK; **(18):** UPSOOK; **(19):** ST-code; **(20):** UPAMSM with MIMO; **(21):** GCM; **(22):** RGB-USM; **(23):** RGB-FSK; **(24):** layered ST-code; and **(25):** layered ST-code with interpolation.

Chapter III

Optical camera communication fundamentals

The OCC systems, as shown in figure III.1 are composed by LED-based devices as emitters, and image sensors as receivers. Since OCC is a type of VLC technique, the data is transmitted by modulating visible light. However, OCC systems also explores the use of Infrared links. Therefore it can use the portion of the electromagnetic spectrum from 300 THz to 790 THz.

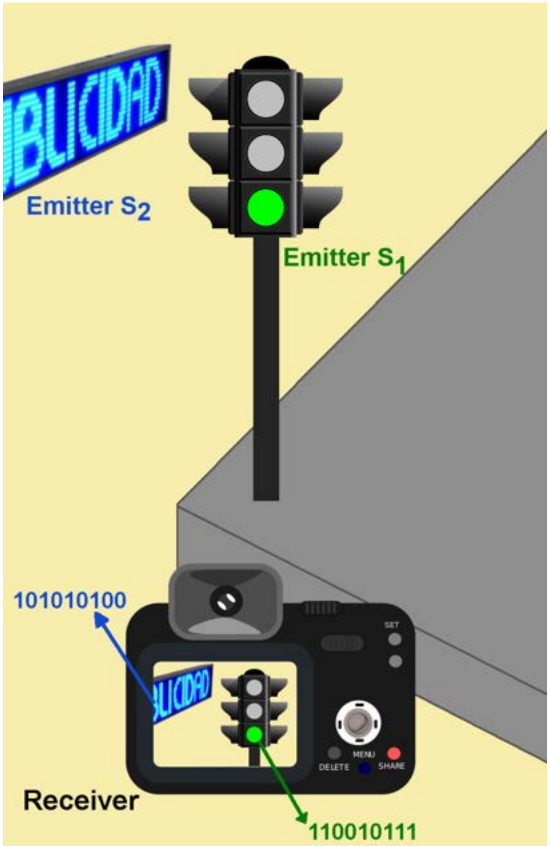

Figure III.1: Optical camera communication system

The light can be modeled as electromagnetic radiation. This electromagnetic radiation is made up of photons. Therefore the light exhibits properties not only of particles but also waves. Depending on its coherence level, the light is propagated with a specific aperture range while traveling in a straight line. When the light falls upon an object, the photons are absorbed, reflected, or transmitted depending on the material. The number of photons determines the light intensity of a particular object emitting or reflecting those photons. The modulation of the light intensity is usually used for transmitting data in VLC systems and consequently in OCC implementations.

The deployment of OCC systems require the adequate selection and configuration of both emitters and receivers. In section III.1 the OCC emitters are briefly described, focusing in their elements and components. In the same way, section III.2 reviewed the camera's operation, while section III.3 presented the main camera's characteristics. Additionally, the transmitted data must be extracted from the frames. Some digital multilevel signal processing tools are required for preparing the images and videos and bring out the information. The tools that have been used in this research work are surveyed in section III.4. Once the frame is processed, the information can be decoded, as described in section III.5.

On the other hand, the approximations of the projected objects on the images and the relation between legit sources and close by interference signals are as important as the communication system's elements for understanding and designing OCC solutions. In section III.6, the equations for calculating the 2-D projection of real-world objects are deduced. Finally, the characterization of the close emitters interference is introduced in section III.7.

III.1 OCC emitters

Since the emitters, LED-based devices, are primarily used for illumination, decoration, or displaying images, the data transmission must not interfere with those tasks. A light switching at a frequency greater than 100Hz is perceived by human beings as turned on because the brain processes the acquired image [97]. In this way, the light of commercial illumination devices can modulate a signal without perturbing people. Due to this fact, LEDs that have a high switching rate is ideal for transmitting the signal.

The LED-based transmitters are composed of a lamp, a driver, and an enclosure. The lamp bulbs are usually formed by more than one LED that can be considered a unique light source due to a diffuser panel as part of the enclosure. Although the commercial lamps have a driver circuit for controlling the current flow and, therefore, the brightness. For OCC implementations, this circuit needs modifications for introducing the modulated signal into the LED without compromising the LED's illumination performance. Consequently, the light is perceived as even without flickering, dimming, or color changes for human eyes. In some cases, the LED-based emitters do not use the light diffuser panel; for example, in Vehicle to Vehicle (V2V) implementations, the signals are transmitted through the car lights which enclosure does not include the diffuser panel. Furthermore, some OCC systems require a LED-based screen as an emitter. In this particular case, the display is controlled through software using one or more drivers depending on the specific necessity of the application and the possibility of image generation. Additionally, the use of a light diffuser panel is avoided since the screen's primary operation is to display sharp images.

For commercial lamps, white light is usually required. The LEDs can produce white light in two different ways [98]. The first method, see figure III.2, is known as "Phosphor White." It combines a short wavelength LED, blue or Ultraviolet (UV), with a yellow phosphor coating. Some of the blue or UV photons generated in the LED are converted into yellow photons in the phosphor layer. The combination of the blue and yellow photons generate white light. This procedure is relatively high efficient and low cost for production. However, the phosphor coating limits the switching rate, which is a constrain for deploying OCC emitters. Additionally, over time, the blue die and the yellow phosphor degrade, resulting in a light shifting in color.

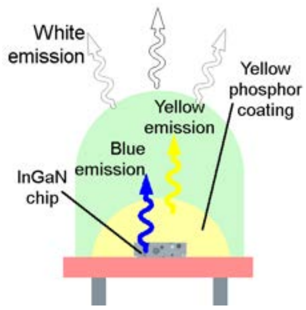

Figure III.2: White LED implementation: blue LED with a yellow phosphor coating

The second method, see figure III.3, is an additive color method which employs three LEDs: red, green, and blue. The output of those LEDs is combined to obtain the white light. This solution gives control over the light's exact color, incorporates three channels to the communication systems so the signal can be multiplexed, and provide faster modulation ratios. However, individual colored LEDs respond differently to drive current, operating temperature, and dimming. This method is then hardware-intensive and requires additional controls for color consistency, increasing the expenses, and implementation costs.

Depending on the selected application of the OCC system, a white light emitter would be deployed with one method or another. For systems that require a high data transmission rate, the RGB method is a solution since the three channels can be used. However, for implementations with strong financial constraints, the phosphor method is a better option. Nevertheless, there are OCC deployments that work with other light colors. For example, in ITS, the system could be implemented using the car's red backlights.

In general, for transmitting the data, the light source's intensity is controlled through the driving current of the LEDs. At first, the data is converted into an optical message, and then the corresponding sequence is used to switch the

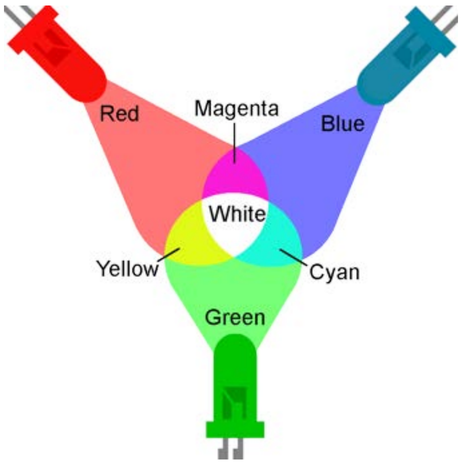

Figure III.3: White LED implementation: additive color method

driver's circuit. The switching frequency depends on the selected modulation scheme. In the specific case of screen-to-camera communication, the data is usually converted into a 2-D-code. An image sensor captures the signals transmitted within the emitted light from a lamp or screen.

III.2 Cameras' operation

Since OCC receivers, image sensors, were designed to obtain pictures, it is necessary to adapt its operation to recollect the transmitted data. The first step for achieving this purpose is to analyze a camera's operation. The adequate camera's characteristics need to be selected for controlling the image acquisition while highlighting the specific light changes in the frames. For analyzing the cameras' operation, it is important to introduce the basic elements of a camera. As shown in figure III.4, the digital cameras usually contain these parts [99]:

1. Lens or objective.- optical lens or assembly of lenses that directs and focuses the light rays on the sensor.

2. Iris diaphragms.- thin opaque structure with an opening called aperture that limits the amount of light passing.

3. Shutter.- basically is an opaque curtain that controls the time that the light can pass. This mechanism can also be implemented electronically by turning the sensor on and off.

4. Digital sensor chip.- semiconductor image sensor that converts the incident light into an array of electrical signals. There are two types Charge Coupled Device (CCD) and CMOS.

5. Processor chip.- device that processes the collected electrical signals into an image.

6. Memory card.- device where the processed image is stored.

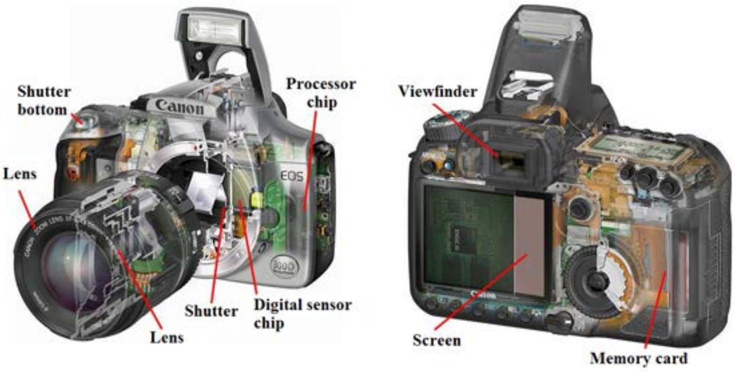

Figure III.4: Camera's basic elements [99]

Similar to the human eyes, the cameras receive light through an opening in the objective. In digital single-lens reflext (DSLR), mirrorless, and higher-end compacts cameras, the aperture is variable. However, in small cameras, like the ones embedded on smartphones, tablets, or wearables, the opening is fixed. This aperture is managed via the iris, and the f-number determines its dimension. A lens's f-number is calculated as the focal length ratio divided by the diameter of the aperture. The lowest f-number represents the biggest aperture and, therefore, the most significant amount of light passing through the lens and gathering by the sensor, which the camera needs to produce quality images. Each step on the f-number doubles the luminosity. [100]

Additionally, the shutter closes and opens the lenses' orifice, allowing the light rays only a defined time's period, known as exposure time (T_{EXP}). The exposure time usually varies from 4 s to 1/2000 s. It is essential to highlight that in small and shoot cameras, the shutter is electronic instead of mechanical. The digital image sensor is turned on only a portion of the time, being sensitive to light. When the exposure time is finished, the sensitivity is disabled, and the charge at each pixel readout. [101]

The light is focused on the image sensor chip using the imaging optic lenses. The distance between these lenses is variable for assuring adequate image sharpness. However, the minimum focus distance is the shortest distance at which a lens can focus. This value depends on the objective as well as its minimum f-number. Nevertheless, the image sharpness is not necessary for implementing OCC systems.

The light then falls upon a microlenses array that focuses it on the semiconductors for producing electrical signals that can be considered analog pixels. These photosensors detect light intensity without wavelength specificity or color information. Therefore a Color Filter Array (CFA), typically a Bayer filter located on top of the photosensors' grid, is needed. Each semiconductor is affected by a color filter that separates the light by wavelength range, including information about the color, see III.5. However, the CFA induces that each semiconductor produces a one color signal. The Bayer filter has a mosaic pattern with 50% green, 25% red, and 25% blue that mimics the human color perception.

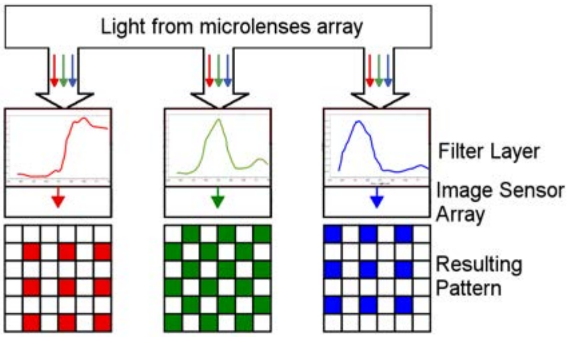

Figure III.5: Color Bayer filters array

The semiconductors receive the light and capture the photons; more light intensity means more electrical charge. The amount of light that the photosensors are capable of catching depends on the sensibility or ISO value. There are two possible ways for reading the incident light: global shutter and rolling shutter.

III.2.a Global shutter

In the case of the global shutter, usually used in Charge Coupled Device sensors (figure III.6), the entire frame is captured at once. As shown in figure III.7, all the pixels are exposed to the incoming light simultaneously, capturing a "static frame" even when the scene's elements are moving. Before the exposure, the pixels' charge is drained. During the exposure time, the pixels collect charge, which is transferred to the corresponding pixel's readout node at once.

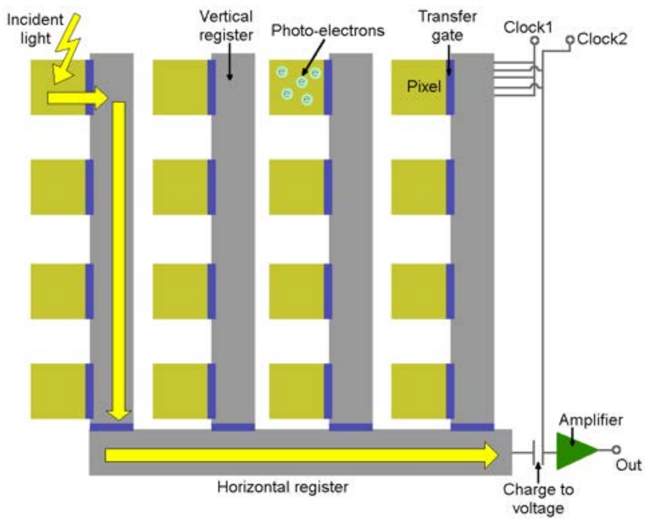

Figure III.6: CCD global shutter scheme

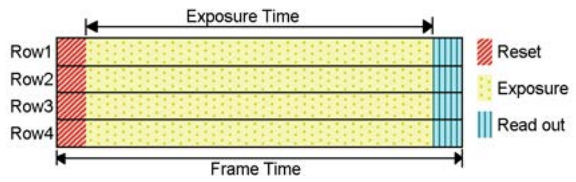

Figure III.7: CCD global shutter frame acquisition time

III.2.b Rolling shutter

The rolling shutter is commonly applied in CMOS sensors (figure III.8). In this case, the scene is scanned by bands, either vertically or horizontally. As shown in figure III.9, different array lines are exposed to the incoming light at different times. Before the exposure, the pixels' charge is drained. When the exposure starts, each row is switched on for collecting charge in sequence. At the end of the row's exposure time, the charge is transferred into each pixel's readout node. All the rows have been exposed to the light the same time but with a slight offset. Therefore different image regions will not be precisely correlated in time, causing spatial distortion. This distortion is known as the rolling effect, and it is more evident when the scene is changing at rates that the image readout could not match. This photographic disadvantage is an advantage for OCC systems. Different rows of the image will represent different times of the transmitted signal.

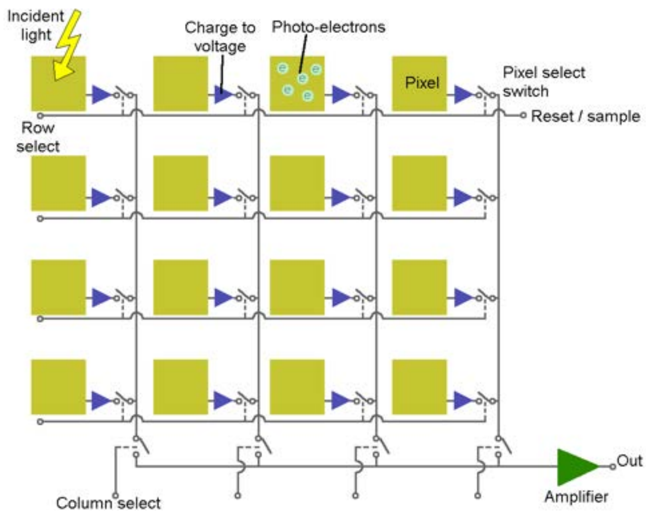

Figure III.8: CMOS rolling shutter scheme

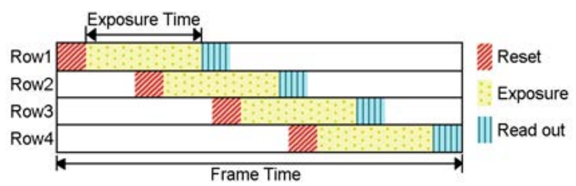

Figure III.9: CMOS rolling shutter frame acquisition time

The collected charge is converted to a voltage amplified according to the ISO value to produce the electrical output signal. Nevertheless, unlike human eyes, the photosensors lack compressive nonlinearity. For this reason, a gamma correction tone is applied to the linear photon capture. So the image's histogram has a normal distribution.

An Analog-to-Digital Converter (ADC) digitizes the electrical signals from the image sensor. However, in this image, each pixel contains the information of only one color. To produce a full-color image, a spatial interpolation operation known as demosaicking is used. Demosaiking is the reconstruction of a color image from the data acquired with a CFA. The simplest method interpolates the missing color values of a pixel from its neighborhood. Since each pixel is affected by one color filter, the exact value of that color is registered, but the other two components must be calculated from the neighbors. However, not all the close pixels have the same color, so the interpolation must be done only along high-contrast edges. [102]

This image requires further digital multilevel signal processing. At first, the white balancing and color correction in function of the light conditions is performed. This process's goal is to define the white color for obtaining a color's temperature pattern. Then the colors under the same light conditions are fixed through this pattern. Additionally, the image is processed to decrease the impact of any faulty pixel (due to a defective photosensor) or imperfect optics.

Finally, the image is compressed using 8-bit luminance information per color (red, green, and blue) for each pixel. It saves memory space and increases the taking pictures' rate. However, information related to white balance, noise reduction, and sharpening is lost in the process. The resulting image is stored in the memory card. In the case of DSLR cameras, the sensor's unprocessed output can be stored as a raw image file, with minimum loss of information. However, these files require post-processing and more storage space.

The obtained image contains information related to the light emitted and reflected by the objects. The configuration of the camera's characteristics determines the appearance of these data. Therefore, the main camera's characteristics should be surveyed for designing OCC systems.

III.3 Cameras' characteristics

Since OCC receivers are image sensors, a critical phase in the system setup is the adequate camera's characteristics management. In this way, during the image acquisition, the specific light changes will be reflected in the obtained frames, and the general system's calculations, such as the appropriate transmission rate, can be done. The primary characteristics that require special attention for OCC implementations are: image light exposure, camera's frame rate, camera's resolution, and camera's Field of View (FoV).

III.3.a Image exposure

During the image acquisition phase, it is vital to avoid the image sensor array's overexposure to the light. If there is too much charge for one photosensor, this charge will overflow to its neighboring semiconductors producing the "blooming effect." As shown in figure III.10, the resulting photo will have white regions with a halo, and the chromatic aberrations will be more visible.

Figure III.10: Blooming effect example

The photo's exposure to light is a balance among the iris opening, the exposure time, and the sensor sensibility. The camera's photometer measures the available light to adjust the iris opening, the time the light can reach the image sensor, and the number of photons that the semiconductors can absorb. So there are three characteristics to control during the setup process.

Sensibility

The digital image sensors can absorb a different amount of photons depending on the selected sensibility. This characteristic is measured according to the International Organization for Standardization (ISO) with integer numbers. The typical sensibility values are: 100, 200, 400, 800, 1600. A greater number represents a greater sensibility and, therefore, more light absorption in the photosensor. However, an increment in the semiconductor sensibility also increases the noise level and reduces the image definition. The image's noise will be seen as color dots in dark zones.

Iris aperture

The aperture of the iris diaphragm is measured with the f-number. This number is considered a quantitative measure of the lens speed or its maximum aperture diameter (minimum f-number). A fast lens has a large maximum aperture and uses a fast shutter speed for collecting light, while a slow lens (smaller maximum aperture) delivers less light intensity and requires a longer exposure time for the same outcome. By definition, the f-number of an optical system, such as a camera lens, is the ratio of the system's focal length to the diameter of the clear aperture in the iris diaphragm. Ignoring differences in light transmission efficiency, a lens with greater f-number projects darker images. The brightness of the projected image (illuminance) relative to the brightness of the scene in the lens's field of view (luminance) decreases with the square of the f-number. In other words, doubling the f-number decreases the relative brightness by a factor of four. In the case of fixed iris aperture, the light collected per second does not change, and therefore the image brightness depends on the exposure time.

Exposure time

Exposure time or shutter speed is the length of time when the digital image sensor inside the camera is exposed to light. During this time, the camera's shutter is open. The amount of light that reaches the image sensor is proportional to the exposure time. The number used in setting the shutter speed refers to the fraction's denominator; a shutter speed set to 60 means that each frame is exposed to light for 1/60 seconds. Additionally, there is a direct relationship between the f-number and the exposure time. To maintain the same photographic exposure when doubling the f-number, the exposure time would need to be four times as long.

III.3.b Frame rate

The frame rate is the average number of images that the camera take per second, expressed as frames per second (fps). This term applies to cameras, computer graphics, and motion capture systems. Frame rate may also be called the frame frequency and be expressed in hertz. A higher frame rate results in more acquired images, assuring that the camera will capture the changes in the light. However, a higher frame rate requires more sophisticated hardware, a larger storage capacity, and higher communication bandwidth for sending the frames if the images are not be processed in situ. Therefore, the selection of the frame rate should not be trivial.

Shutter speed and frame rate are two closely related camera settings but are not the same. As seen in the previous subsection, Shutter speed is the amount of time that each frame is exposed.

III.3.c Camera's resolution

The camera's resolution is the amount of detail that the camera can capture. It is measured in pixels, usually megapixels (MP), due to multiplying the pixel axis dimensions of the obtained frame. An image with more pixels has more details and information. Therefore more bits can be sent per frame, and a higher data transfer range can be achieved. However, a more oversized frame also requires more storage capacity that is a constrain for the cameras embedded on nowadays portable devices or wearables. Consequently, the image resolution selection in some Internet of Things (IoT) applications requires a trade-off between the required information rate and the available storage capacity.

III.3.d Field of view

FoV is the portion of the scene that is visible through the camera. Objects outside the FoV are not recorded in the photograph. The FoV is typically expressed as an angle of view, the angular size of the view cone.

As shown in figure III.11 and equation III.1, the FoV is determined by the lens' focal length (f) and the sensor's size. Focal length is a measure directly proportional to the lens' size. The FoV narrows as the focal length increases.

$$\text{FoV} = 2\arctan\left(\frac{\text{Sensor Size}}{2f}\right) \tag{III.1}$$

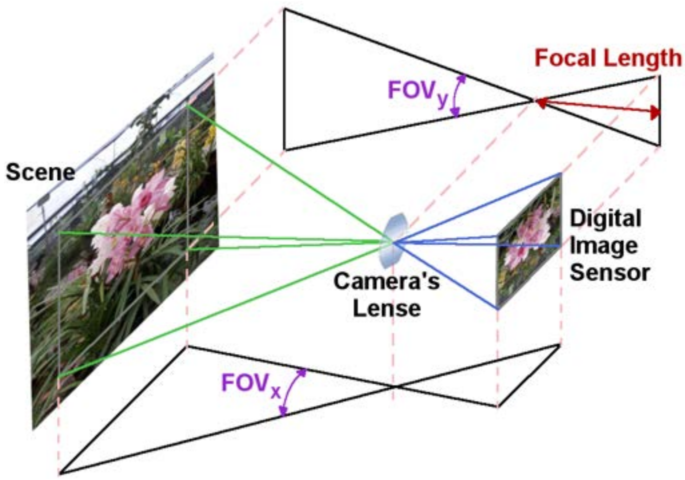

Figure III.11: Field of view and focal length in image acquisition

Since the digital image sensor's size and the focal length depend on the camera's implementation, the FoV is a fixed camera's characteristic. However, this characteristic defines a captured object's maximum size at a specific distance from the camera. Therefore, the receiver's selection should take into account this value along with the maximum resolution of the device.

All these camera's characteristics are fundamental for capturing the transmitted data in the image adequately. Nevertheless, for extracting the information from each frame, a digital multilevel signal processing is required.

III.4 Digital multilevel signal processing

The data extraction from the images is not a trivial task. The appropriate image processing tools should be used during this procedure. In this subsection, some necessary image processing tools used in this work are explained. The primary image showed in figure III.12 is employed to illustrate each procedure's operation.

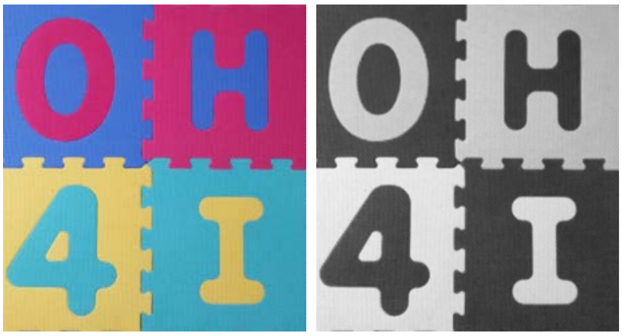

(a) (b)

Figure III.12: Original image for DSP. **(a):** RGB image; **(b):** gray-scale image

III.4.a Binarization

Binarization is the process of transforming an image into a binary array. At first, the image is converted into grayscale, or the process should be applied to each frame component: red array, green array, and blue array. A threshold gets applied; any pixel's intensity above this value is considered a one; otherwise, it is a zero. The threshold can either be set fixed or adaptive. The resulting image is a white and black version of the captured scene. In figure III.13 an example of binarization using a fixed threshold of 0.25 (63.75/256) is showed. Since the value was selected independently of the image, the binarization is not optimal, and the resulting image has some blurred zones.

During the research work, the Otsu thresholding method [103] has been applied. This procedure separates pixels into two classes based on the image's histogram values. The threshold is determined by minimizing the intra-class intensity variance. This variance is defined as the weighted sum of the two classes' variances. Otsu's method requires a histogram with bimodal distribution and a deep and sharp valley between the two peaks. In figure III.14.(a) the histogram of the original image is showed. This histogram presents two peaks: pixel's intensity 55 and 200, with a well-defined valley between them. Based on that histogram,

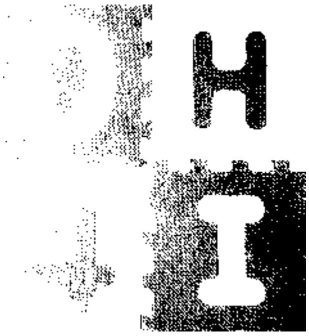

Figure III.13: Binarization of gray-scale image using fixed threshold (0.25)

the Otsu algorithm set the threshold on $145/255 = 0.5686$. The resulting binary array is showed on figure III.14.(b).

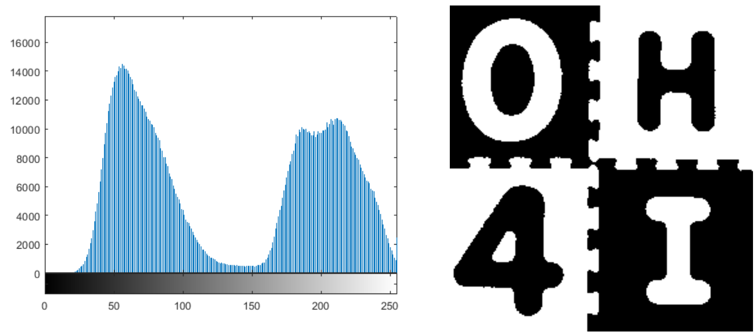

(a) (b)

Figure III.14: Binarization of gray-scale image using Otsu thresholding: **(a):** Histogram of grayscale image; **(b):** Binarized image

During the data extraction, the frames' binarization is usually the first step in obtaining the location of the light sources. In general, this binarization uses adaptive thresholding algorithms.

III.4.b Image segmentation

Image segmentation is the process of defining which pixels belong to which objects, called image regions. Therefore, a region in an image is a group of connected or unconnected pixels with similar properties. Pixels are assigned to regions using some criterion that distinguishes them, for example, value similarity (the difference between pixel intensity) and spatial proximity (Euclidean distance). This segmentation can also be done by finding boundary pixels, called edges. Most edge detectors use intensity characteristics since regions on either side of the boundary may have different gray values. The segmentation is fundamental during the data extraction procedure. Usually, the regions of the frame correspond to the different emitters.

An example of segmentation over a binary image with continuous regions is shown in figure III.15. In this case, the segmentation algorithm assumed that the regions were composed of the connected "white" pixels. Therefore five regions were obtained; region 3 is the internal part of the number four (4) represented in region 1.

(a) (b) (c) (d) (e)

Figure III.15: Image segmentation of the binarized image into consecutive regions. **(a):** region 1; **(b):** region2; **(c):** region 3; **(d):** region 4; **(e):** region 5.

Another example of segmentation is shown in figure III.16. In this case, the segmentation was performed by color, allowing non-consecutive regions. The algorithm was feed with a sample of the desired colors: red and yellow. Therefore the regions with other colors (green and blue) were eliminated.

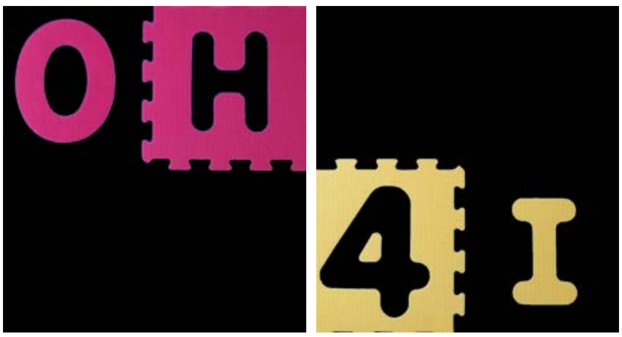

(a) (b)

Figure III.16: Image segmentation by color of the image into non-consecutive regions. **(a):** region of color red; **(b):** region of color yellow.

Several properties can be extracted from the regions. During this research, the used properties were: area, perimeter, centroid, circularity, and significant axis length. The area is defined as the number of pixels in the region, while the perimeter is the distance in pixels around the region's boundary. The centroid is the region's center of mass; in the case of non-consecutive regions, the centroid can be outside the regions. The major axis length corresponds to the ellipse's major axis, with the same normalized second central moments as the region. Finally, the circularity is an estimation of the object's roundness; it is calculated with equation III.2. For a perfect circle, the circularity value is 1.

$$\text{Circularity} = \frac{4 * \text{Area} * \pi}{\text{Perimeter}^2} \tag{III.2}$$

These information help in the adequate identification of the regions. In this way the analysis can be focus on the regions containing the transmitted data. For example, in table III.1 the information from the recovered regions showed on figure III.15 is presented. These information identify the region 3 as an small object in comparison with the other regions, therefore it is identified as the center of the number without the necessity of visualizing or extracting that region.

Table III.1: Consecutive regions' characteristics: segmentation over a binarized image case.

Region	Area	Centroids	Major Axis Length	Perimeter	Circularity
1	231042	(289,906)	833.92	3016	0.32
2	105031	(235,285)	521.71	1796	0.41
3	7261	(212,920)	129.87	388	0.61
4	284743	(843,307)	754.13	3325	0.32
5	61376	(863,929)	541.43	1560	0.32

Areas, Major Axis Lengths, and Perimeters are in pixels. Centroids is the location following a (x,y) format

III.4.c Image masking

Image masking is the process of separating specific objects within a picture. For this purpose, a binary image, which has the same dimensions as the picture, is used as a mask. The pixels corresponding to the objects are set to one, while the others are set to zero. Then the original image frame and the mask are multiplied element by element. figure III.17 shows the result of this process.

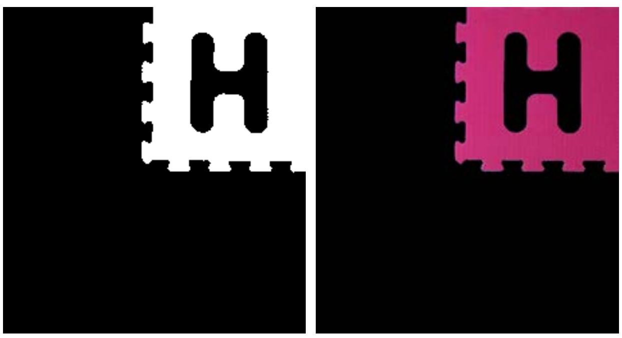

(a) (b)

Figure III.17: Image masking example. **(a):** selected mask; **(b):** resulting cropped image.

An application of image masking is the extraction of the region of interest (ROI) in a frame. By definition, ROI is a portion of an image required to extract information or perform some other operation.

III.4.d Convolution filtering

Convolution Filtering is an image processing method in which a small image, called a filter mask, is defined and then used to modify a larger image. The general process of filtering consists of moving the filter mask from point to point in an image. At each point (x,y) of the original image, a filter's response is calculated by a predefined relationship called convolution. Convolution is a neighborhood operation in which each output pixel is the weighted sum of neighboring input pixels. This procedure accomplishes many image processing techniques, such as edge detection, motion detection, and noise reduction. figure III.18 shows a filter for noise reduction over an RGB image. In this way, a frame obtained under bad environmental conditions can be enhanced for the data extraction.

(a) (b)

Figure III.18: Convolution filtering using filter mask h = [1 0 1] **(a):** original image; **(b):** resulting image.

III.4.e Morphological operations

Morphological Operations is a broad set of non-linear image processing operations related to the shape or morphology of features in an image. The value of each pixel in the processed image is based on comparing the corresponding pixel in the original image with its neighbors. These operations apply a structuring element, a small shape or template that identifies the pixel in the original image and defines the neighborhood used in the processing.

Morphological operations rely on the relative ordering of pixel values, not on their numerical values, and therefore are especially suited to the processing of binary images. However, these techniques can also be extended to grayscale images.

The most basic morphological operations are dilation and erosion. Dilation adds pixels to both the inner and outer boundaries of regions in an image. In this case, the selected structuring element is used for probing and expanding the shapes, as shown in figure III.19. It acts as a maximum local filter, makes objects more visible, and fills in small holes in objects.

(a) (b)

Figure III.19: Dilation of binary image using a 15 pixel radius disk as structuring element. **(a):** original image; **(b):** dilated image.

Erosion removes pixels on both the inner and outer boundaries of regions in an image. The structuring element is used for probing and reducing the shapes contained in the input image, as shown in figure III.20. It acts as a local minimum filter; the holes and gaps between different regions can be eliminated.

(a) (b)

Figure III.20: Erosion of binary image using a 5 pixel radius disk as structuring element. **(a):** original image; **(b):** eroded image.

III.4.f Statistical measures in digital image processing

Sometimes for the data extraction procedure, some statistical measures are needed. The three main statistical measures in digital image processing are the 2D mean, the 2D standard deviation, and the correlation coefficient. The most basic of all statistical measurements is the 2D mean ($\mu_A(x, y)$). It represents the average value of the intensity of the pixels. In other words, it is the expected value of a pixel. The mean is used for noise reduction by spatial filtering of the image.

In the same way, the 2D standard deviation ($\sigma_A(x, y)$) is a measure of variability or diversity of the intensity of the pixels. It shows how much dispersion exists in the image from the average value. A low standard deviation indicates that the pixels tend to be very similar. The standard deviation can be used for noise reduction. However, this measurement gives more information related to the image.

The Pearson correlation coefficient (PCC) assesses the degree of linear correlation between two image matrices A and B. The coefficient is calculated using equation III.3 and varies from -1 to 1. If the two images are equal, they are perfectly correlated, and therefore the coefficient would be 1. In the case of similar images, as shown in figure III.19, the value of the coefficient is close to one; for the proposed image, the value was 0.7306. Suppose the two images are opposite, as the images are shown in figure III.21, they are perfectly anti-correlated so that the coefficient would be -1. If there is no linear correlation between the images, the coefficient would be 0. For example, the images in figure III.22 are not similar neither opposite; therefore, the resulting coefficient is close to zero (0.1605).

$$PCC(A,B) = \frac{\sum_x \sum_y (A_{xy} - \overline{A})(B_{xy} - \overline{B})}{\sqrt{\left(\sum_x \sum_y (A_{xy} - \overline{A})^2\right)\left(\sum_x \sum_y (B_{xy} - \overline{B})^2\right)}} \tag{III.3}$$

(a) (b)

Figure III.21: Images with perfect anti-correlation

(a) (b)

Figure III.22: Images with low linear correlation

This brief review of the fundamental digital multilevel signal processing tools is the base for explaining the data extraction

III.5 OCC data extraction

In OCC systems, the transmitted signal is captured in the images. These data require additional image processing for being recovered. In some applications, the emitters' location is unknown, and therefore the first step is to detect the light sources on the frame. Usually, the frame is binarized with an adaptive threshold algorithm for this purpose.

Once the light source is located, the corresponding ROI is extracted for speeding up the extraction process. It is quicker to analyze a small frame than a complete image. From the ROI the light state is extracted in the case of the global shutter sensors, as shown in figure III.23. However, if the sensor is a rolling shutter, the image's light and dark strips should be analyzed; see figure III.24.

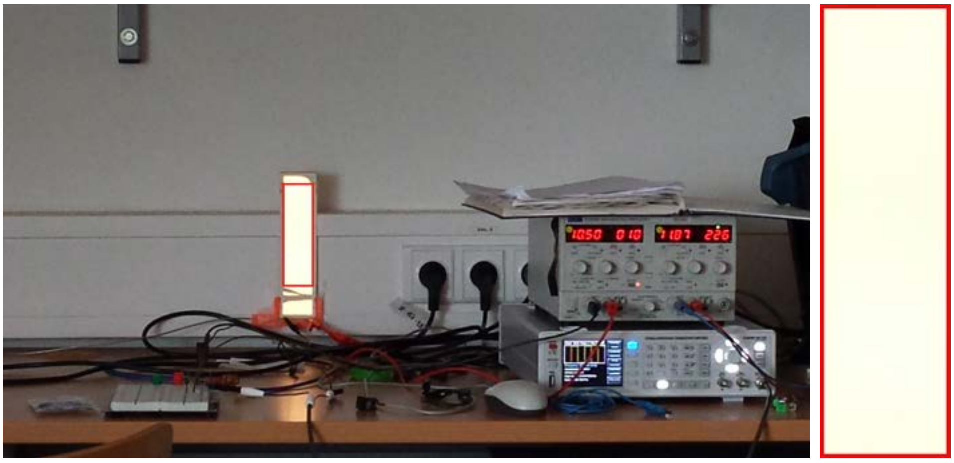

(a) (b)

Figure III.23: Data extraction: example with global shutter sensor. **(a):** acquired image, the red rectangle is the location of the light source; **(b):** extracted ROI, in this case the light state is ON

III.6 Geometry of projected distances

As described in chapter I, the implementation of IoT applications in urban environments requires a simple method for estimating the number of pixels that represent a real object in a photography. This estimation should be based on the camera's main characteristics (FoV and resolution), the distance between the camera and the target, and the object's rotations. There are two basic rotations for the element: over the horizontal axis and over the vertical axis. The first one is represented by the camera-object horizontal plane's angle intersecting the object's normal plane (β). In this case, when $\beta = 90°$ the device is aligned horizontally with the camera. In the same way, the second rotation is determined by the angle of the camera-objective vertical plane intersecting the objective's normal plane (γ). When $\gamma = 90°$ the device is aligned vertically with the camera. figure III.25 shows an example of image acquisition.

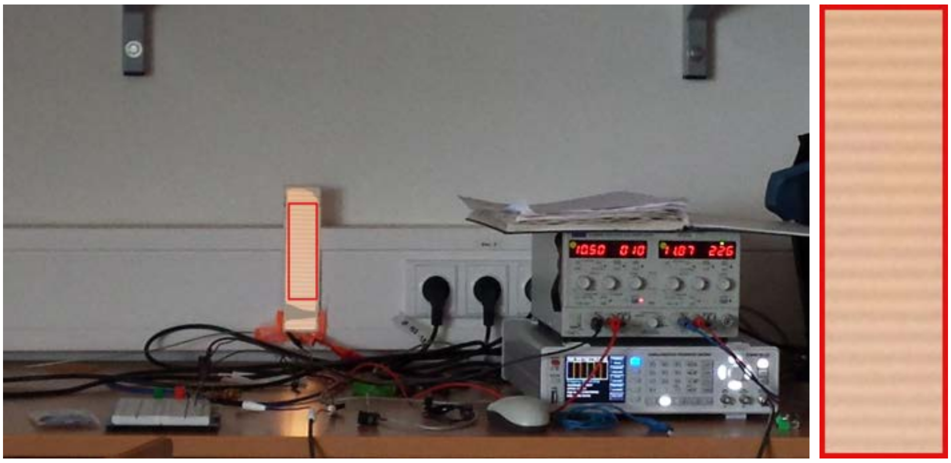

(a) (b)

Figure III.24: Data extraction: Example with rolling shutter sensor. **(a):** acquired image, the red rectangle is the location of the light source; **(b):** extracted ROI, in this case the darker strips represent zeros, while the brighter bands are ones

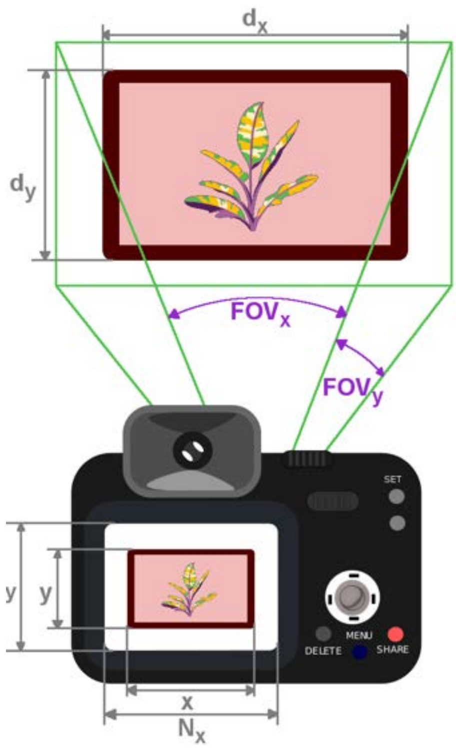

Figure III.25: Image acquisition example. In this case, D is the distance between the camera (receiver) and the object (transmitter), d_x and d_y are the horizontal and vertical distances in the real world

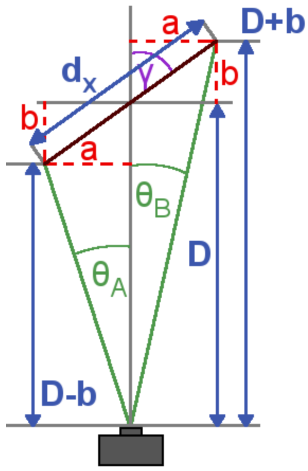

Figure III.26: Horizontal projection with angle $\beta = 90°$ and angle γ variable

III.6.a Projections with rotation over the vertical axis

To represent the rotation of the object over the vertical axis, the angle of the emitter-receiver vertical plane intersecting the emitter's normal plane, γ, is presumed to be variable. Nevertheless, for simplicity, the emitter-receiver horizontal plane's angle intersecting the transmitter's normal plane, β, is assumed to be fixed to 90°.

Horizontal projection

For the horizontal projections, the FoV corresponds to the horizontal pixel's resolution of the frame. In the same way, the angle θ corresponds to the 2-D projection of d_x:

$$\left.\begin{array}{c}\mathrm{FoV}_x \to N_x \\ \theta \to 2x\end{array}\right\} \implies x = \frac{\theta}{\varphi_x} \tag{III.4}$$

where, as shown in figure III.26:

$$\theta = \theta_A + \theta_B \tag{III.5}$$

$$\tan\theta_A = \frac{a}{D-b} \to \theta_A = \arctan(\frac{a}{D-b}) \tag{III.6}$$

$$\tan\theta_B = \frac{a}{D-b} \to \theta_B = \arctan(\frac{a}{D+b}) \tag{III.7}$$

In the same way the values of a and b values can be obtained from the relations of the angle γ:

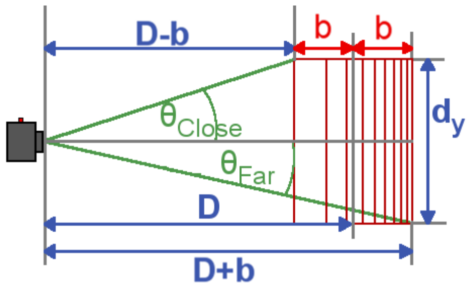

Figure III.27: Vertical projection with angle $\beta = 90°$ and angle γ variable

$$\sin\gamma = \frac{a}{d_x/2} \implies a = \frac{d_x}{2}\sin\gamma \tag{III.8}$$

$$\cos\gamma = \frac{b}{d_x/2} \implies b = \frac{d_x}{2}\cos\gamma \tag{III.9}$$

Therefore the 2-D projection of d_x can be expressed as:

$$x = \frac{1}{\varphi_x}\left[\arctan\left(\frac{\frac{d_x \cdot \sin\gamma}{2}}{D - \frac{d_x\cos\gamma}{2}}\right) + \arctan\left(\frac{\frac{d_x \cdot \sin\gamma}{2}}{D + \frac{d_x\cos\gamma}{2}}\right)\right] \tag{III.10}$$

After some simplifications the equation is:

$$x = \frac{1}{\varphi_x}\left[\arctan\left(\frac{d_x \cdot \sin\gamma}{2D - d_x\cos\gamma}\right) + \arctan\left(\frac{d_x \cdot \sin\gamma}{2D + d_x\cos\gamma}\right)\right] \tag{III.11}$$

Vertical projection

For the vertical projections, the FoV corresponds to the vertical pixel's resolution of the frame. In the same way, the angle θ corresponds to the 2-D projection of d_y:

$$\left.\begin{matrix} \mathrm{FoV}_y \to N_y \\ \theta \to y \end{matrix}\right\} \implies y = \frac{\theta N_y}{\mathrm{FoV}_y} = \frac{\theta}{\varphi_y} \tag{III.12}$$

Since β is assumed to be fixed to 90° while γ is variable, there are two cases for the vertical projection, as shown in figure III.27. Due to the object's rotation, its vertical edge can be closer to or farther from the camera, so the 2-D projection will not be the same.

Case 1: the vertical edge of the object is closer to the camera ($\theta = 2\theta_{\text{close}}$)

$$\begin{aligned}
\tan\theta_{\text{close}} &= \frac{d_y/2}{D-b} \\
\implies \theta_{\text{close}} &= \arctan\left(\frac{d_y/2}{D-b}\right) = \arctan\left(\frac{d_y/2}{D-(d_x/2)\cos\gamma}\right) \\
\implies y_{\text{close}} &= \frac{2}{\varphi_Y}\arctan\left(\frac{d_y}{2D-d_x\cos\gamma}\right)
\end{aligned} \tag{III.13}$$

Case 2: the vertical edge of the object is farther from the camera ($\theta = 2\theta_{\text{far}}$).

$$\begin{aligned}
\tan\theta_{\text{far}} &= \frac{d_y/2}{D+b} \\
\implies \theta_{\text{far}} &= \arctan\left(\frac{d_y/2}{D+b}\right) = \arctan\left(\frac{d_y/2}{D+(d_x/2)\cos\gamma}\right) \\
\implies y_{\text{far}} &= \frac{2}{\varphi_y}\arctan\left(\frac{d_y}{2D+d_x\cos\gamma}\right)
\end{aligned} \tag{III.14}$$

Therefore the 2-D projection of d_y can be expressed as:

$$y = \begin{cases} \frac{2}{\varphi_y}\arctan\left(\frac{d_y}{2D+d_x\cos\gamma}\right) & \text{farthest element} \\ \frac{2}{\varphi_y}\arctan\left(\frac{d_y}{2D-d_x\cos\gamma}\right) & \text{closest element} \end{cases} \tag{III.15}$$

III.6.b Projections with rotation over the horizontal axis

When the object is rotated over the horizontal axis, the emitter-receiver horizontal plane's angle intersecting the transmitter's normal plane, β, is variable. For the rotation over the vertical axis, for simplicity, γ is fixed to 90°.

Vertical projection

For the vertical projections, the FoV corresponds to the horizontal pixel's resolution of the frame. In the same way, the angle θ corresponds to the 2-D projection of d_y:

$$\left.\begin{matrix} \text{FoV}_y \to N_y \\ \theta \to 2y \end{matrix}\right\} \implies y = \frac{\theta}{\varphi_y} \tag{III.16}$$

where,

$$\theta = \theta_A + \theta_B \tag{III.17}$$

$$\tan\theta_A = \frac{a}{D-b} \to \theta_A = \arctan\left(\frac{a}{D-b}\right) \tag{III.18}$$

$$\tan\theta_B = \frac{a}{D-b} \to \theta_B = \arctan\left(\frac{a}{D+b}\right) \tag{III.19}$$

In the same way the values of a and b values can be obtained from the relations of the angle β:

$$\sin\beta = \frac{a}{d_y/2} \implies a = \frac{d_y}{2}\sin\beta \tag{III.20}$$

$$\cos\beta = \frac{b}{d_y/2} \implies b = \frac{d_y}{2}\cos\beta \tag{III.21}$$

Therefore the 2-D projection of d_y can be expressed as:

$$y = \frac{1}{\varphi_y}\left[\arctan\left(\frac{\frac{d_y \cdot \sin\beta}{2}}{D - \frac{d_y\cos\beta}{2}}\right) + \arctan\left(\frac{\frac{d_y \cdot \sin\beta}{2}}{D + \frac{d_y\cos\beta}{2}}\right)\right] \tag{III.22}$$

After simplifications the following equation is obtained:

$$y = \frac{1}{\varphi_y}\left[\arctan\left(\frac{d_y \cdot \sin\beta}{2D - d_y\cos\beta}\right) + \arctan\left(\frac{d_y \cdot \sin\beta}{2D + d_y\cos\beta}\right)\right] \tag{III.23}$$

Horizontal projection

For the horizontal projections, the FoV corresponds to the horizontal pixel's resolution of the frame. In the same way, the angle θ corresponds to the 2-D projection of d_x:

$$\left.\begin{matrix} \mathrm{FoV}_x \to N_x \\ \theta \to x \end{matrix}\right\} \implies x = \frac{\theta N_x}{\mathrm{FoV}_x} = \frac{\theta}{\varphi_x} \tag{III.24}$$

Since γ is assumed to be fixed to 90° while β is variable, there are two cases for the horizontal projection.Due to the object's rotation, its horizontal edge can be closer to or farther from the camera, so the 2-D projection will not be the same.

Case 1: the horizontal edge of the object is closer to the camera ($\theta = 2\theta_{\text{close}}$).

$$\begin{aligned} \tan\theta_{\text{close}} &= \frac{d_x/2}{D-b} \\ \implies \theta_{\text{close}} &= \arctan\left(\frac{d_x/2}{D-b}\right) = \arctan\left(\frac{d_x/2}{D-(d_x/2)\cos\beta}\right) \\ \implies x_{\text{close}} &= \frac{2}{\varphi_x}\arctan\left(\frac{d_x}{2D - d_y\cos\beta}\right) \end{aligned} \tag{III.25}$$

Case 2: the vertical edge of the object is farther from the camera ($\theta = 2\theta_{\text{far}}$).

$$\begin{aligned} \tan\theta_{\text{far}} &= \frac{d_x/2}{D+b} \\ \implies \theta_{\text{far}} &= \arctan\left(\frac{d_x/2}{D+b}\right) = \arctan\left(\frac{d_x/2}{D+(d_y/2)\cos\beta}\right) \\ \implies y_{\text{far}} &= \frac{2}{\varphi_x}\arctan\left(\frac{d_x}{2D + d_y\cos\beta}\right) \end{aligned} \tag{III.26}$$

Therefore the 2-D projection of d_x can be expressed as:

$$x = \begin{cases} \frac{2}{\varphi_x} \arctan\left(\frac{d_x}{2D+d_y\cos\beta}\right) \text{ farthest element} \\ \frac{2}{\varphi_x} \arctan\left(\frac{d_x}{2D-dy\cos\beta}\right) \text{ closest element} \end{cases} \quad \text{(III.27)}$$

III.6.c Generalized projections

Finally, the generalized equations III.28 and III.29 have been obtained. These equations estimate the 2-D pixel projection (x, y) in a picture of a real distance (d_x, d_y) in function of the separation between the object and the camera (D), the relative angle of the object (β or γ), and the camera's FoV and resolution in pixels ($N_{x,y}$).

$$x = \begin{cases} \frac{1}{\varphi_x}\left[\arctan\left(\frac{d_x\sin\gamma}{2D-d_x\cos\gamma}\right) + \arctan\left(\frac{d_x\sin\gamma}{2D+d_x\cos\gamma}\right)\right] & \beta = 90^\circ \\ \frac{2}{\varphi_x}\left[\arctan\left(\frac{d_x}{2D+d_y\cos\beta}\right)\right] & \gamma = 90^\circ \text{ \& Farthest} \\ \frac{2}{\varphi_x}\left[\arctan\left(\frac{d_x}{2D-d_y\cos\beta}\right)\right] & \gamma = 90^\circ \text{ \& Closest} \end{cases} \quad \text{(III.28)}$$

$$y = \begin{cases} \frac{2}{\varphi_y}\left[\arctan\left(\frac{d_y}{2D+d_x\cos\gamma}\right)\right] & \beta = 90^\circ \text{ \& Farthest} \\ \frac{2}{\varphi_y}\left[\arctan\left(\frac{d_y}{2D-d_x\cos\gamma}\right)\right] & \beta = 90^\circ \text{ \& Closest} \\ \frac{1}{\varphi_y}\left[\arctan\left(\frac{d_y-\sin\beta}{2D-d_y\cos\beta}\right) + \arctan\left(\frac{d_y\sin\beta}{2D+d_y\cos\beta}\right)\right] & \gamma = 90^\circ \end{cases} \quad \text{(III.29)}$$

These deduced equations demonstrated that a more significant amount of pixels would represent an emitter closer to the camera than a transmitter farther from the receiver when they have the same size in the real world. Therefore, the data extraction when the distance between the camera and the light source increases is more challenging. Additionally, for the modulation schemes that take advantage of the rolling shutter effect for speeding up the transmission, the number of bits represented in a single frame decreases with the distance.

Another critical problem that requires special attention is the interference from close emitters. In some cases, even if the transmitters are adequately separated in the real world, due to the location of the elements and the distance's difference, one external light source's projection may interfere with a legit emitter. The transmitter closeness in the projected frame should be analyzed.

III.7 Normalized power signal to interference ratio

As mentioned in chapter I, the light emitted by sources outside the OCC system can interfere with the legit transmitters. In other words, some light rays of external lamps can affect the projection of the transmitters. This interference depends on the sources' proximity over the projected scene, even if the emitters are separated in the real-world. Closer emitters will affect more the projection than farther sources.

The relation between the legit source's pixels and the close emitter's pixels was deduced for determining this particular optical interference. This relation is called NPSIR. It was determined within the corresponding image channel, directly related to the color wavelength.

The calculation of the number of pixels projected from a light source depends on how the OCC system affects the optical power. This communication system has two main blocks: the channel and the camera process, as shown in figure III.28.

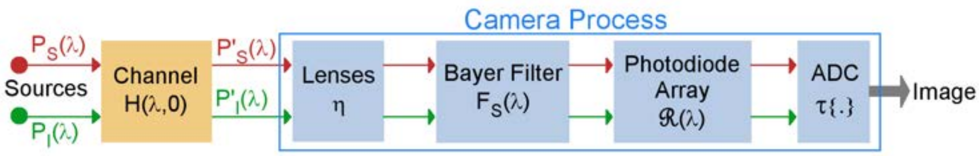

Figure III.28: OCC system's diagram for a legit light source and a close emitter interfering

Each illumination source emits an optical power spectrum, $P_X(\lambda)$, which is affected by the environmental conditions and other interferences within the communication link. Since this channel can be modeled by the gain $H(\lambda, 0)$, the light from any illumination source that arrives at the camera can be expressed by equation III.30.

$$P'_X(\lambda) = \int P_X(\lambda) H(\lambda, 0) d\lambda \tag{III.30}$$

In section III.2 the frame acquisition process was outlined. The light falls on the lenses and then in the microlenses array, so the signal is corrected using the geometric factor η, and the lenses focus the light into the digital image sensor composed by a photodiode array. Before this array, the light rays impact over the CFA, typically a Bayer Filter. These filters have impulse responses $F_{Color}(\lambda)$, for each image channel. The signal is affected by the corresponding $F_S(\lambda)$. Then the signal arrives at the photodiode array where each component has a Silicon Responsivity $R(\lambda)$, changing the signal. Finally, the ADC transforms the signal using the nonlinear function $\tau\{\cdot\}$. Therefore, in the obtained image, the number of pixels from the source X can be expressed by equation III.31

$$\mathrm{Pix}_X = \eta_X \cdot \tau\Big\{ \int P_X(\lambda) H(\lambda,0) F_S(\lambda) R(\lambda) d\lambda \Big\} \tag{III.31}$$

The NPSIR depends only on the number of pixels in the frame that includes information from multiple light sources. For this work, the worst-case scenario is assumed. Both light emitters are transmitting all the time simultaneously. In this way, the NPSIR is not affected by the camera's shutter speed, which defines the image integration time. Therefore equation III.31 is not affected by this camera's characteristic and can be directly used for calculating the number of pixels. The deduced pixel relation can be observed in equation (III.32).

$$\frac{\mathrm{Pix}_S}{\mathrm{Pix}_I} = \frac{\eta_S}{\eta_I} \cdot \frac{\tau\Big\{ \int P_S(\lambda) H(\lambda,0) F_S(\lambda) R(\lambda) d\lambda \Big\}}{\tau\Big\{ \int P_I(\lambda) H(\lambda,0) F_S(\lambda) R(\lambda) d\lambda \Big\}} \tag{III.32}$$

The expression η_S/η_I corresponds to the geometric ratio. The relation between the number of pixels of signal respect to the number of pixels of interference within the frame's ROI. In other words, the geometric ratio is the NPSIR. This interference ratio is independent of the transmitted optical power, the silicon responsivity of the photodiode arrays, and the camera's Bayer filter.

For simplicity, the analyzed scenario is assumed as LoS without aerosols or precipitations. In this case, the extinction factor is unitary for all λ. Therefore the term $H(\lambda, 0)$ can be considered constant and can be taken out of the integral and simplified. Finally the NPSIR can be determined using equation III.33.

$$\mathrm{NPSIR} \cong \frac{\mathrm{Pix}_S}{\mathrm{Pix}_I} \cdot \frac{\int P_I(\lambda) F_S(\lambda) R(\lambda) d\lambda}{\int P_S(\lambda) F_S(\lambda) R(\lambda) d\lambda} \tag{III.33}$$

Since NPSIR is defined as a tool for determining the BER boundary of an OCC link, this value can be used as a primary measurement for simulating more complex scenarios. An example of this will be presented in chapter V.

Chapter IV

Distance-independent modulation

As seen in section II.3, there are several modulation schemes developed or adapted for OCC. However, these modulation techniques have three main constraints: data rate, limited distance range, and the algorithm's complexity. Additionally, the OCC implementations should avoid the flickering problem, so the lights can also be used for illumination, decoration, or advertising purposes without disturbing the people. The flickering free modulations with low complexity algorithms only perform adequately for a medium distance range because the number of bits represented in a single frame decreases with the distance. In the case of the long-distance modulation schemes that have been proposed [46, 77, 78, 89, 91, 92], these techniques rely on high complexity algorithms that require an adaptive thresholding method and a calibration process for identifying the light state. Moreover, the most advanced schemes use several bits in each transmission header for assuring the calibration, decreasing the throughput [93, 94]. In general, the available modulation methods work correctly for either short or long distances but not for both cases.

In this chapter, a flickering free, distance independent modulation that overcomes these constraints is proposed. This scheme can be defined as a rolling shutter effect-based modulation that requires a minimum number of light bands for extracting the information. Therefore it can work for short, medium and long distances. At first, the theoretical fundamentals of the modulation are presented in section IV.1. Then, to assure that the system can identify that a transmission started, a simple wake-up process is proposed in section IV.2. The modulation and demodulation scheme is detailed in section IV.3, where the equations for determining the appropriated switching frequencies for the implementation are presented. Finally, in section IV.4, the advantages of this scheme are presented.

IV.1 Theoretical fundamentals

This effect should be analyzed since the proposed scheme can be considered a rolling shutter effect-based modulation. As stated in subsection III.2.b, when a rolling shutter digital image sensor is employed, one scan-line of photosensors is exposed to the light at the time, and the output is immediately read-out.

Therefore the first line starts its exposure at T_0, and the next scan-line is shifted by a fixed period T_1, acquiring different light information. For this reason, if a light source is switching on and off at frequency f_{SW} greater than the camera's frame rate f_{CAM} the resulting image will include dark and light bands, as shown in figure IV.1. The pixel's intensity in those bands depends on the environmental conditions, the emitter's optical power, and the camera's settings. However, the light strips' width depends on the camera's characteristics and the transmitter's switching frequency.

(a) (b) (c)

Figure IV.1: Rolling shutter effect: ROI of images containing a LED-based lamp switching at 1500 Hz, acquired with a rolling shutter camera at 25 fps. **(a):** original frame size 640×480, default camera's characteristics for gray-scale image, room light turned on; **(b):** original frame size 1080×1420, default camera's characteristics for color image, room light turned off; **(c):** original frame size 1080×1420, camera's with high contrast, low brightness and low exposure time, color image, room light turned off

IV.1.a Switching frequency

It is important to deduce an equation for calculating the light bands' width due to the rolling shutter effect. At first, the light source's location is determined and the corresponding ROI is extracted. Independently of the emitters' shape, the ROI is a rectangle within the light source containing the maximum number of available rows. In this way, the resulting image only contains the light and dark lines eliminating the background and limiting possible elements that can affect the system performance. From the definition of the camera's frame rate is deduced that each frame is acquired over the same time T_{CAM}. The total amount of exposed lines, pixels' resolution in that direction (N_y), correspond to that time. In the same way, the switching signal period T_{SW} is related to the number of pixels in a dark band and a light strip combined. Assuming that the switching signal has a 50% duty cycle, the band's pixel resolution, N_{BAND}, is approximately the same for dark and light strips, and it is related to half the time T_{SW}, as shown in equation IV.1.

$$\left.\begin{array}{r} N_y \rightarrow T_{\text{CAM}} \\ N_{\text{BAND}} \rightarrow T_{\text{SW}}/2 \end{array}\right\} \implies N_{\text{BAND}} = \frac{N_y T_{\text{SW}}/2}{T_{\text{CAM}}} \tag{IV.1}$$

Since $T_{CAM} = 1/f_{CAM}$ and $T_{SW} = 1/f_{SW}$, the band's pixel resolution can be calculated in function of the camera's frame rate and the switching signal's frequency, well-known values, using equation IV.2.

$$N_{\text{BAND}} = \frac{N_y f_{\text{CAM}}}{2\ f_{\text{SW}}} \tag{IV.2}$$

Additionally, depending on the relation between the switching frequency and the camera's frame rate, the lighter and darker bands' relation on consecutive frames change. These changes will be used as the data codification scheme in the proposed flickering free, distance independent modulation. Since the relation between the bands on consecutive frames can be calculated using the PCC, the switching frequency can be deduced from this value. There are three possible cases for the relation between the switching frequency and the camera's frame rate:

1. The signal frequency is a multiple of the camera's frame rate.

$$f_{SW} = \alpha f_{CAM}$$

2. The signal frequency is perfectly uncoupled.

$$f_{SW} = (\alpha + 0.5) f_{CAM}$$

3. The signal frequency is between the previous values.

$$\alpha f_{CAM} < f_{SW} < (\alpha + 0.5) f_{CAM}$$

In the first case, the signal's period will repeat exactly α times during the frame's acquisition. Therefore, if the light is turned on at T_i of frame m, the light will also be turned on at T_i of frame $m+1$. Furthermore, consecutive frames of the light source's ROI will be almost equal. In other words, when $f_{SW} = \alpha f_{CAM}$ the consecutive frames are highly correlated and therefore $PCC \approx 1$.

In the second case, the signal's period will repeat exactly $(\alpha+0.5)$ times during the frame's acquisition. In other words, when the camera starts the next frame's capture, the signal will be shifted 50% of its period. If the light is turned on at T_i of the capturing process of frame m, the light will be turned off at T_i of frame $m+1$ a due to the 50% signal's duty cycle. Furthermore, consecutive frames of the light source will be close to inverted images. So, when $f_{SW} = (\alpha + 0.5) f_{CAM}$ the consecutive frames are almost anti-correlated and therefore $PCC \approx -1$.

In the third case, the signal's period will repeat exactly $(\alpha + k)$ times during the frame's acquisition. In other words, when the camera starts the next frame's capture, the signal will be shifted between 0% and 50% of its period, depending on the selected switching frequency. The resulting images of consecutive frames vary from highly correlated to almost anti-correlated in a quasi-linear relation, and therefore $-1 < PCC < 1$.

The inspection of these consecutive frames gives information related to the frequency of the switching signal. However, the PCC is not the only statistical measure that provides information about the signal transmitted over the light. The 2-D mean ($\mu_{ROI}(x, y)$) and the 2-D standard deviation ($\sigma_{ROI}(x, y)$) also presents interesting relations with the light source input signal.

IV.1.b Statistic data

Other 2-D statistic measurements also provides interesting information related to the acquired images. If we calculate the 2-D mean ($\mu_{ROI}(x, y)$) and the 2-D standard deviation ($\sigma_{ROI}(x, y)$) of images with different switching signal's frequencies, the values will not change significantly.

The 2-D mean is related to the average pixel's intensity; therefore, this value will be affected by the environmental conditions, the camera's exposition setup, and the light intensity. Two frames of switching lamps captured by the same camera under similar environmental conditions will have similar intensity values, even if the frequency varies. In the case of a continuous signal, the 2-D mean value will increase due to eliminating the dark strips.

In the same way, since the 2-D standard deviation ($\sigma_{ROI}(x, y)$) represents the variability of the intensity of the pixels, its value do not change for the blinking images which pixels diversity is similar (dark and light strips). However, the 2-D standard deviation of the image where the light is continuously turned on is close to zero.

These two statistic measurements provide important information related to the light source's input signal, especially by comparison. If a continuous signal is employed, $\sigma_{ROI}(x, y)$ will be close to zero while $\mu_{ROI}(x, y)$ will directly represent the lamp optical power. If a switching signal is used, $\sigma_{ROI}(x, y)$ will increase while $\mu_{ROI}(x, y)$ will decrease. Therefore by comparing the 2-D mean and standard deviation of two frames, a possible input signal change can be detected. Therefore these elements can be used for implementing a simple wake-up process.

IV.2 Wake up process

As stated in the previous section, the 2-D mean and 2-D standard deviation can be employed for determining a change in the light input signal. Consequently, these values can be used for detecting the beginning of the transmission as the base of the wake-up procedure.

Since the emitters can start the transmission at any time, the camera is continuously acquiring frames. However, there must be a mark that triggers data extraction, also known as the wake-up signal. For this scheme, a change in the LED's input signal was selected as the token.

If the LED-based lamp is not emitting data, it will be constantly turned on. Therefore, $\sigma_{ROI}(x,y)$ will be close to zero and $\mu_{ROI}(x,y)$ will have its maximum value. When the transmission starts, the LED will vary its state from on to off continuously. As a result of this change, $\sigma_{ROI}(x,y)$ increases while $\mu_{ROI}(x,y)$ decreases, triggering the data extraction on the camera's communication side.

Similarly, when the transmission ends, the emitter receives once again a constant signal at its input. So, $\sigma_{ROI}(x,y)$ returns to the minimum value and $\mu_{ROI}(x,y)$ increases, stopping the information's extraction process.

As can be observed in figure IV.2, the wake-up process is based on the comparison of consecutive frames' 2-D mean and analysis of actual frame's 2-D standard deviation. Since the procedure started assuming that the system is not transmitting data (State = waiting), the maximum possible value was assigned to the 2-D mean as an initial value, $\mu_{F0}(x,y) = 255$. In the case of the 2-D standard deviation, a threshold value is needed; a 3% of the maximum value was selected, $\sigma_{Th}(x,y) = 6.3750$, based on experimental intermediate results.

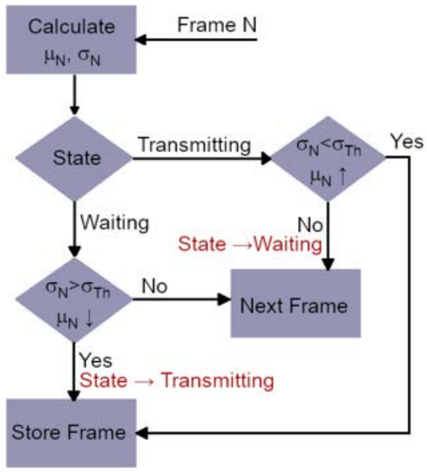

Figure IV.2: Wake up algorithm's diagram.

When a frame (F_N) is captured, the ROI that contains the emitter's projection is extracted for calculating the 2-D mean ($\mu_{F_N}(x,y)$) and standard deviation ($\sigma_{F_N}(x,y)$). Then the obtained values are compared with the previous frame's mean and the threshold standard deviation. Depending on the comparison's outcome and the current system's state, F_N's ROI can be stored for data extraction or ignored. If the algorithm was waiting for a transmission, the standard deviation is greater than the threshold ($\sigma_{F_N}(x,y) > \sigma_{Th}(x,y)$), and the mean decreases ($\mu_{F_N}(x,y) < \mu_{F_{N-1}}(x,y)$), then a transmission has started. So the system's state change to transmitting, and the frame's ROI is stored.

In the same way, if the algorithm is in the "emitting data" state, the frame's ROI is stored except when the standard deviation is lower than the threshold ($\sigma_{F_N}(x,y) < \sigma_{Th}(x,y)$), and the mean increases ($\mu_{F_N}(x,y) > \mu_{F_{N-1}}(x,y)$). In this case, the transmission is assumed to be stopped, the system's state changes to waiting, and the frame is ignored. In table IV.1, the obtained values from three experiments are showed. In all the examples, the camera was acquiring frames at a rate of 25 fps. In the first case, the original frames $F_(a)$ were gray-scale images of 640×480 that were taken in a room with the light turned on. The camera's exposure time was low. For the second case, $F_(b)$ were color images of 1080×1420 taken by a camera with default characteristics in a room where the light was turned off. In the last case, the camera's settings were high contrast, low brightness, and low exposure time for 1080×1420 color images $F_(c)$, taken in a room with the light turned off.

Table IV.1: Waking up examples from transmissions shown on figure IV.1. The case **(a)** cooresponds to gray-scale images of 640×480 taken in a room with the light turned on. For the case **(b)** the camera acquired color images of 1080×1420 with default characteristics in a room where the light was turned off. In the last case **(c)**, the camera's setting were high contrast, low brightness and low exposure time for 1080×1420 color images taken on a room with the light turned off.

State	$\mu_{ROI(a)}$	$\sigma_{ROI(a)}$	$\mu_{ROI(b)}$	$\sigma_{ROI(b)}$	$\mu_{ROI(c)}$	$\sigma_{ROI(c)}$
Waiting	223.87	4.22	252.52	4.26	168.95	4.66
Transmitting	208.39	18.76	231.43	27.28	120.74	55.93

With this procedure, the transmission is detected. However, when the communication starts, there are three options regarding the acquisition of the emitter's projection (ROI):

1. The data transmission start before the ROI scanning, figure IV.3.a.
2. The data transmission start after the ROI scanning, figure IV.3.b.
3. The data transmission start in the middle of the ROI scanning, figure IV.3.c.

In the first case, the emission began previous to the emitter's acquisition, therefore the 2-D standard deviation of the ROI in the first frame, F_1, is bigger than the defined threshold ($\sigma_{F_1} > 3\%$) and the transmission is detected on that frame. Assuming that the emission of that particular symbol lasted for at least three frames, the ROI extracted from F_1, F_2 and F_3 are stored for demodulation. The data can be obtained without problem from those images. For example, on figure IV.3 the first transmitted symbol corresponds to the perfectly correlated frequency ($f_{SW} = \alpha f_{CAM}$), in case (a) the calculated PCC of those three stored ROI is equal to one ($PCC(F_1, F_2) = PCC(F_2, F_3) = 1$), so the symbol is perfectly identified.

In the second case, the emission started after the emitter's acquisition, therefore the 2-D standard deviation of the ROI from frame F_1 is lower than the defined threshold ($\sigma_{F_1} < 3\%$) and the transmission is not detected on that frame. However the calculated 2-D standard deviation of frame F_2 is bigger than the

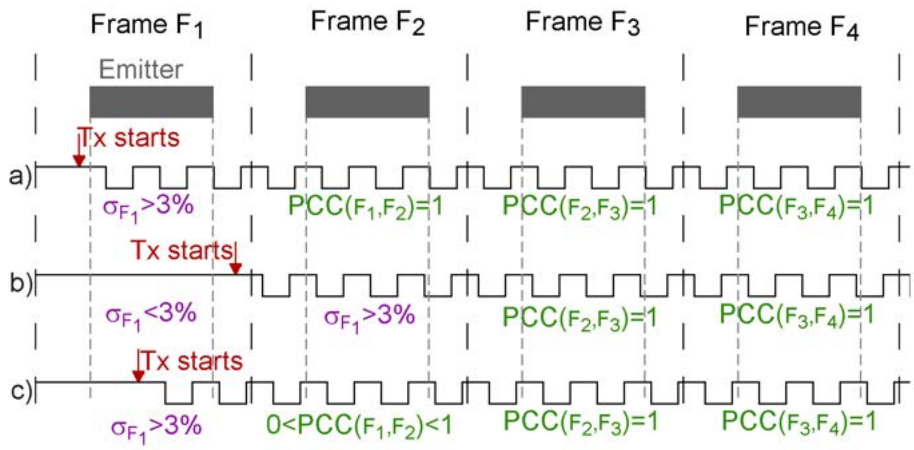

Figure IV.3: Transmission's examples. **(a):** the transmission started previous to the emitter's acquisition; **(b):** the emission began after the projection of the transmitter on the frame; **(c):** the first bit was transmitted during the acquisition of the emitter's pixel rows.

threshold ($\sigma_{F_1} > 3\%$) and the transmission is detected on the second frame. Assuming that each symbol is emitted for at least three times the frames' acquisition period ($3T_{CAM}$), the ROI extracted from F_2, F_3 and F_4 are stored for demodulation. The data can be obtained without problem form those images. For example, on figure IV.3 case (b) the calculated PCC of those three stored ROI is equal to one ($PCC(F_2, F_3) = PCC(F_3, F_4) = 1$), so the symbol is perfectly identified.

In these two scenarios, the information is successfully extracted from all the stored frames. Nevertheless, the third case is different. Since the transmission starts during the acquisition process, one part of the ROI from frame F1 has a wide bright strip. This band corresponds to the time previous to the data transmission when the emitter is continuously turned on. Depending on the remaining acquisition time, there are two possibilities: the ROI has dark stripes, or ROI has only bright rows. In the first scenario, due to the presence of darker stripes, the 2-D standard deviation of the ROI is bigger than the threshold ($\sigma_{F_1} > 3\%$), and the transmission is detected on this frame. Assuming that each symbol is emitted for at least three times the frames' acquisition period ($3T_{CAM}$), the ROI extracted from F_1, F_2 and F_3 are stored for demodulation. Nevertheless, the data can not be appropriately obtained from those images. For example, on figure IV.3 case (c) the calculated PCC of the two first stored ROI is positive and less than one ($0 < PCC(F_1, F_2) < 1$), so the symbol is wrongly identified, while the PCC of the remaining stored ROI is equal to one ($PCC(F_2, F_3) = 1$) and the symbol is identified. The second scenario is similar to the case where the emission started after the emitter's acquisition. All the rows are bright pixels so the 2-D standard deviation of the ROI is lower than the threshold ($\sigma_{F_1} < 3\%$) and the transmission is not detected on F_1. The ROIs collection is triggered on frame F_2, so the ROI extracted from F_2, F_3 and F_4 are stored for demodulation. Dislike the previous scenario, the demodulation from frames F_2 and F_3 is correct, but the accuracy of the symbol extracted from frames F_3 and F_4 can not be assured due to the presence of the next transmitted symbol.

To avoid the demodulation uncertainty that a transmission starting during the acquisition process may produce, all the emissions begin with a known symbol. If the decoded symbol from the first two ROIs is different from the defined one, the emission started during the acquisition process generating the first scenario, and the ROI has dark stripes. In this case, the first frame's ROI of each frame group is ignored, and the data extraction is applied to the remaining frames. However, if the decoded symbol from the last two ROIs is different from the defined one, the emission started during the acquisition process generating the second scenario; the ROI has no dark stripes. In this case, the last frame's ROI of each frame group is ignored, and the data extraction is applied to the remaining frames.

After explaining the wake-up procedure that determines if the transmission started and selects which frames should be analyzed for data extraction, the modulation and demodulation technique will be introduced.

IV.3 Modulation technique

As was detailed on section IV.1, depending on the switching signal's frequency value there is a specific correlation between consecutive frames, with three main cases:

1. If the frequency is a multiple of the camera's frame rate ($f_{SW} = \alpha f_{CAM}$), the consecutive frames are highly correlated. Therefore, as stated on Subsecection III.4.f, the PCC is close to one.

2. If the frequency is perfectly uncoupled ($f_{SW} = (\alpha + 0.5) f_{CAM}$), the consecutive frames are almost anti-correlated, therefore the PCC is almost minus one.

3. For the frequencies between this two cases ($\alpha f_{CAM} < f_{SW} < (\alpha{+}0.5) f_{CAM}$), the resulting images of consecutive frames varies from highly correlated to almost anti-correlated in a quasi linear relation, in other words, the PCC is between minus one and one.

These correlations are the flickering free distance independent modulation's basis. During the data transmission state, the emitter is switched on and off by applying a square signal with 50% duty cycle. This signal's frequency varies depending on the corresponding data symbol. Since each frequency generates a specific correlation between consecutive frames, the symbol can be identified by calculating the PCC value. The PCC represents the linear correlation between two images using equation III.3. This value varies from -1 (opposite images) to 1 (similar images). The correct frequency selection assures four possible outcomes from the consecutive frames' comparison and, therefore, a 2 bits per symbol codification:

1. Consecutive frames highly correlated ($PCC > 0.7$), when the frequency is a multiple of the camera's frame rate ($f_{SW} = \alpha f_{CAM}$).

2. Consecutive frames highly anti-correlated ($PCC < -0.7$), when the frequency is perfectly uncoupled ($f_{SW} = (\alpha + 0.5)f_{CAM}$).

3. Consecutive frames moderately correlated ($0 < PCC < 0.65$), when the frequency is greater than but close to a multiple of the camera's frame rate.

4. Consecutive frames moderately anti-correlated ($-0.65 < PCC < 0$), when the frequency is lower than but close to the uncoupled frequency.

Each two-bit symbol is emitted for a specific time (T_{SW}), which is a multiple of the frame's time ($T_{SW} = mT_{CAM}$). For assuring the data extraction accuracy, even when the transmission starts during the emitter's acquisition process, the emission should last at least three frames ($m \geq 3$).

When the system is in the "Transmitting" state, the rectangular ROI containing only the light and dark bands from the emitter is obtained and stored from each frame. During the data extraction process, as shown in figure IV.4, these frames' ROI are normalized using the "max-min" technique. In this way, the frames' pixel values are in the same range (from 0 to 1). Therefore, any possible effect of an environmental light change is mitigated. Then the PCC is calculated from the adequate consecutive frames' ROI.

As stated in the previous section, if the transmission started during the acquisition of the emitter's pixel rows, the frame's ROI, which contains the transition between symbols, is eliminated from the frame's group. In this case the PCC calculation is done $m - 2$ times. Otherwise, when the emission began before or after the emitter acquisition, this process is done $m - 1$ times. Then the average PCC of the frame's group is determined from the obtained PCC values. Finally, based on that average PCC value, the data is decoded using equation IV.3.

$$DATA = \begin{cases} 10 & PCC > 0.7 \\ 11 & 0 < PCC < 0.65 \\ 01 & -0.65 < PCC < 0 \\ 00 & PCC < -0.7 \end{cases} \tag{IV.3}$$

Since the PCC value is obtained from the consecutive frames' comparison, there is no need for thresholding techniques to identify the light state. Moreover, the pixel's intensity value by itself is irrelevant, so an initial calibration is not required. Additionally, these correlation values can be evaluated with an image's ROI containing two strips or more. So, the system's theoretical distance range depends on the emitter's projected size and the band's pixel size. These dimensions can be easily calculated using equations III.29, III.28, and IV.2. Then the obtained values can be used for the frequency selection in the system design process. Therefore equations for determining the adequate frequencies for each implementation must be deduced. These equations are based on the α parameter which relates f_{SW} and f_{CAM}, called frequency multiplier. This parameter has specific requirements related to the camera's characteristics, the emitter's size, and the system's distance range. In the next subsection, the selection of this value will be explained.

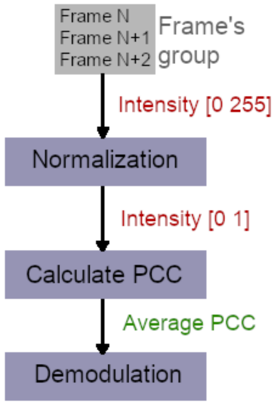

Figure IV.4: Data extraction scheme's diagram.

IV.3.a Frequency multiplier's selection

In order to employ the adequate frequencies, the frequency multiplier (α) must be determined based on the system's characteristics: distance range, the selected camera's vertical resolution, and vertical FoV; and the selected emitter's dimensions. This frequency multiplier is an integer parameter that multiply the camera's frame rate (f_{CAM}) to obtain the coupled frequency, defined as $f_{SW} = \alpha f_{CAM}$. Using this relation, equation IV.2 can be modified to calculate the band's size in terms of the camera's resolution and the frequency multiplier, as shown in equation IV.4.

$$\begin{aligned} N_{\text{BAND}} &= \frac{N_y f_{\text{CAM}}}{2\ \alpha f_{\text{CAM}}} \\ N_{\text{BAND}} &= \frac{N_y}{2\ \alpha} \end{aligned} \tag{IV.4}$$

As has been stated previously, the PCC requires that each image contains at least two strips. Therefore the projected vertical size of the light source, y_{Source}, must be greater than the double of the strip's vertical size. Additionally, in order to locate the transmitter in the frame, recover the corresponding ROI and adequately process the cropped image, the band's vertical size should be greater than five pixels. The theoretical value is three pixels for assuring the four possible PCC values. However, the five pixel requirement was determined from the execution of several experiments related with the data extraction process for OCC. Therefore the boundaries of the number of light bands are expressed as:

$$
\begin{gathered}
y_{\text{Source}} > \upsilon N_{\text{BAND}} > 5 \quad \upsilon \geq 2 \\
\frac{2}{\varphi_y}\left[\arctan\left(\frac{d_y}{2D}\right)\right] > \upsilon\left(\frac{N_Y}{2\ \alpha}\right) > 5\upsilon \\
\frac{N_y}{10} > \alpha > \frac{\frac{\upsilon}{2}\varphi_y N_y}{2\ \arctan\left(\frac{d_y}{2D}\right)}
\end{gathered} \tag{IV.5}
$$

Therefore, the frequency multiplier α can be obtained based on the camera's characteristics (φ_y, N_y, FoV_y), the distance between the emitter and the receiver (D), and the light source's size (d_y) using equation IV.6

$$
\frac{N_y}{10} > \alpha > \frac{\upsilon \text{FoV}_y}{4\left[\arctan\left(\frac{d_y}{2D}\right)\right]} \tag{IV.6}
$$

As previously stated, this frequency multiplier is the base for selecting the switching frequencies under specific conditions. The selection process is presented in the following subsection.

IV.3.b Switching frequencies' selection

The frequency multiplier, α, directly provides two frequencies for the system: coupled frequency ($f_1 = \alpha f_{CAM}$) and uncoupled frequency ($f_2 = (\alpha + 0.5) f_{CAM}$). The next step is to determine the other two frequencies needed for the two-bits symbols generation.

Based on the quasi linear relation between the frequencies in the range from αf_{CAM} to $(\alpha + 0.5) f_{CAM}$ and the consecutive frames' ROI correlation coefficient, a fixed step between the frequencies is assumed. This relation is depicted in equation IV.7 and can be observed in figure IV.5

$$
\begin{aligned}
\text{step} &= \frac{(\alpha + 0.5) f_{\text{CAM}} - \alpha f_{\text{CAM}}}{3} \\
&= \frac{\alpha f_{\text{CAM}} + 0.5 f_{\text{CAM}} - \alpha f_{\text{CAM}}}{3} \\
&= \frac{f_{\text{CAM}}}{6}
\end{aligned} \tag{IV.7}
$$

The remaining frequencies are calculated using equation IV.7 as follows:

$$
\begin{aligned}
f_3 &= f_1 + \text{step} \\
&= \alpha f_{\text{CAM}} + \frac{f_{\text{CAM}}}{6} \\
&= \left(\alpha + \frac{1}{6}\right) f_{\text{CAM}}
\end{aligned} \tag{IV.8}
$$

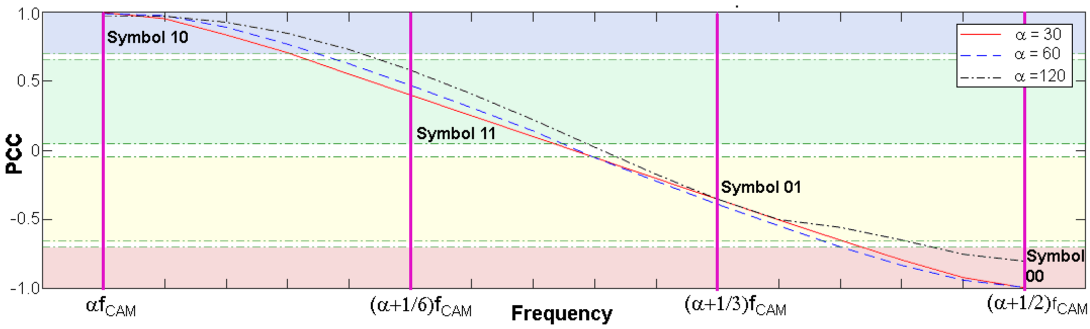

Figure IV.5: Relation between the PCC values and the switching frequencies. All the experiments were performed with a camera's frame rate of 30fps. The straight red line represents $\alpha = 30$, and band's size = 36 pixels. The dashed blue line represents $\alpha = 60$, and band's size = 18 pixels. The dotted black line represents $\alpha = 120$, and band's size = 9 pixels.

$$\begin{aligned} f_4 &= f_1 + 2\text{step} \\ &= \alpha f_{\text{CAM}} + \frac{2 f_{\text{CAM}}}{6} \\ &= \left(\alpha + \frac{1}{3}\right) f_{\text{CAM}} \end{aligned} \tag{IV.9}$$

Therefore the switching signal frequency can be determined using equation IV.10

$$f_{\text{SW}} = \begin{cases} \alpha f_{\text{CAM}} & \text{DATA} = 10 \\ (\alpha + 1/6) f_{\text{CAM}} & \text{DATA} = 11 \\ (\alpha + 1/3) f_{\text{CAM}} & \text{DATA} = 01 \\ (\alpha + 1/2) f_{\text{CAM}} & \text{DATA} = 00 \end{cases} \tag{IV.10}$$

IV.4 Modulation's advantages

The flickering free, distance independent modulation scheme proposed in this chapter overcomes two of the main constraints for OCC modulation techniques: limited distance range and high algorithm's complexity. Since at least three consecutive frames are required for transmitting two bits symbols, the data rate is limited to 2 $f_{CAM}/3$. This data rate is greater than the value obtained by other similar modulations that reach transmissions of $f_{CAM}/2$. However a 2 $f_{CAM}/3$ transmission is considered slow but usable for IoT applications. Therefore the data rate issue is partially addressed.

Nevertheless, the proposed procedure increases the average distance range of the modulation schemes and is intended to implement short, medium, and long links. This modulation is defined as a rolling shutter effect-based modulation. The distance constraint for this type of modulation is that the number of recovered bands decreases with the distance. However, for this technique, data extraction requires a minimum number of light bands. Therefore it can perform without problems even for long distances where only two bands are recovered.

Additionally, the modulation is based on changing the switching frequency for different symbols, while the demodulation relies on the simple calculation of the PCC value from consecutive frames. Consequently, the process complexity is minor. The use of the PCC value also eliminated the necessity of an adaptive thresholding algorithm for identifying the light state in each frame. In the same way, the pixel's intensity value is irrelevant due to the frame normalization performed at the beginning of the demodulation process. Therefore an initial calibration is not required; neither the system is affected by changes in the environmental conditions.

Due to these advantages, the proposed modulation scheme can be easily implemented for a wide range of OCC applications independently of the distance between the emitters and the camera. Since the complexity is minor, non-specialized hardware can be used for the deployment of the OCC systems without impacting its performance. Therefore, this modulation scheme is suitable for IoT applications in urban environments where the distances vary from less than one meter to several hectometers.

For observing the performance of the proposed systems, simulations and experimental implementations have been prepared. The preliminary results of these field experiments and simulations are presented in the next chapter, along with some possible implementations of OCC systems for deploying IoT applications.

Chapter V

Simulations and experimental validation

Since proving the predictions is a fundamental phase in any scientific research, some simulations, lab experiments, and field tests were performed as part of this thesis. At first, a set of trials were done in a darkroom for validating the usability of equations III.28, and III.29, presented in section III.6, for estimating, based on the camera's characteristics, the number of pixels (vertical, and horizontal dimensions) that real-world objects produce in an image without complex plane transformations or projections. This estimation is the base for determining the closeness of light sources within an OCC system and predicting the interference from close-emitters. In the same way, the emitter's pixel projection approximation is used as a constrain value during the implementation of the proposed distance-independent modulation scheme. Once the accuracy of this pixels' estimation was validated, the prediction of close-emitters interference over an OCC communication link had to be proven. For this purpose, initially, an experiment was designed to obtain the values of the relation NPSIR, introduced in section III.7, for the different color channels (red, green, and blue) with known distances between the sources. These experimental measurements were then used to prove the usability of the NPSIR to directly quantify the impact of relative close emitters over the communication's link performance. An indoor WSN using OCC was designed, and simulated. The BER of this system was calculated using the NPSIR values. These predictions were compared with the simulation's outcomes regarding the accuracy of the received signal. In this way, the possibility of estimating the impact of close-emitters interference over an OCC communication link was proved. This prediction of the communication performance's degradation due to the closeness of light sources can be used for avoiding its effect by applying interference compensation on the receiver side during the data extraction process or by placing the system's emitters adequately during the applications' implementation.

The next step in the research was to demonstrate the existence of viable OCC applications for IoT. Two proposed implementations were validated with lab tests and field experiments. The first one was an indoor positioning and tracking system that can be adapted for outdoor applications, while the second one was an outdoor WSN for smart cities. With those simulations and field experiments, the implementation of OCC-based systems for IoT was validated. Nevertheless, the outdoor implementation was no flickering-free; the long-distance demodulation process required the same light state in the full emitter image even if the receiver was a rolling shutter camera, so the system works as in global shutter conditions where the data rate depends only on the frame rate. In this particular field experiment, since the selected LED-based device was used for advertising purposes, the flickering was not an issue. However, in general, the outdoor applications need a flickering-free distance-independent modulation scheme, like the one proposed in chapter IV. This process required validation for short, medium, and long-distance rages to be used in different applications. To prove that this scheme works properly, a two phases procedure was used.

During the first stage, the procedure described in chapter IV for selecting the switching frequencies was tested. For this purpose, the modulated signals using the proposed scheme were generated using the switching frequencies obtained by applying equation IV.10 for different frequency multiplier α values. These signals were then used as the light emitters' input in the flickering free, distance independent modulation scheme simulations. From these simulations, the corresponding PCC values of the acquired consecutive frames were calculated to demonstrate the frequency selection procedure. Once this process was validated, the switching frequencies for three different distance ranges were selected and applied during the second stage. The experimental implementation of the proposed scheme was done using those frequencies for determining the system's BER, and therefore, prove that the proposed modulation scheme can be used for applications independently of the distance range.

V.1 Validation of projected pixels' estimation

The pixels' estimation of real-world distances is important for determining potential light interference sources' closeness and predicting systems implementations' viability. In this sense, the usability, and accuracy of equations III.28, and III.29 for estimating the projected pixels requires validation. A basic OCC system, shown in figure V.1, was designed for measuring the light sources separation (vertical, and horizontal) in pixels under different parameters. The emitters' location is fixed over a board, so their distance does not change during the experiments. However, the board can be rotated over the vertical axis for changing the angle γ, located in the intersection of the camera-objective vertical plane and the object's normal plane. Additionally, the distance between the emitters' board and the camera can be modified without changing the angle γ. In this way, the sources' separation's experimental measurements can be compared with the pixels' estimation obtained using the deduced equations.

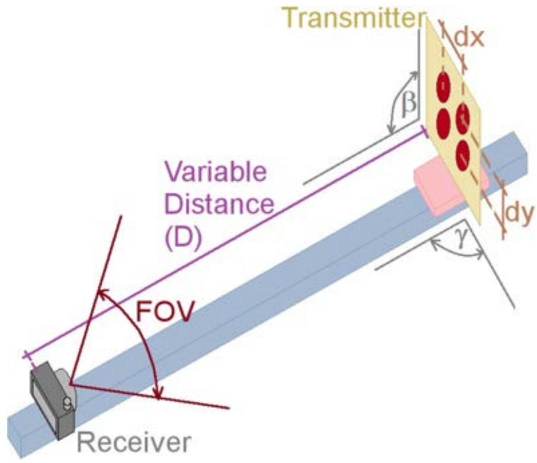

Figure V.1: Testbed designed for validating the estimation of the pixels' projections. The angle γ is variable while the angle β is fixed to 90°, in the same way, the distance between the emitter, and the receiver (D) can be changed.

V.1.a Experimental setup

Since this experiment's goal is to measure the separation between the light sources in the images obtained from different distances with different rotations and compare these outcomes with the theoretically estimated ones, the real-world separation should not change during the trials. For this purpose, the implementation of the proposed system, as shown in figure V.2, has four LEDs fixed over a board for emitting the signal, while the receiver was mounted over a 2 m rail allowing the modification of distance D without changing the angles between the camera's normal plane, and the object.

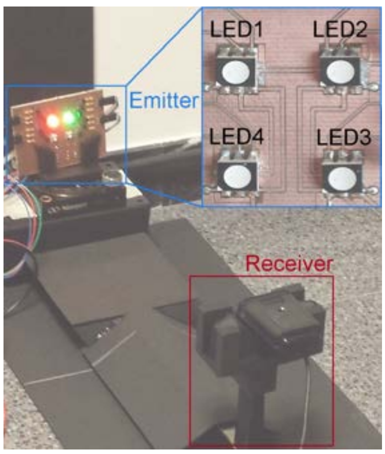

Figure V.2: Implemented experimental testbed

The board shown in figure V.3 was used as the emitter. In this case, the selected LEDs were circular shaped with a radius of 5 mm, and viewing angle of 120°; each LED was RGB with independent control of each color. This board was located over an angle translator for emulating possible vertical rotations by changing the angle γ accurately over four values: 45°, 60°, 75°, and 90°. The distance between the emitter, and the receiver, D, varied from 20 cm to 200 cm. At each position D 160 photographs were taken, 40 frames per angle γ: 10 with all the LEDs in red, 10 with all the LEDs in blue, 10 with all the LEDs in green, and 10 with all the LEDs in white. The resulting 1600 images were stored and then processed off-line.

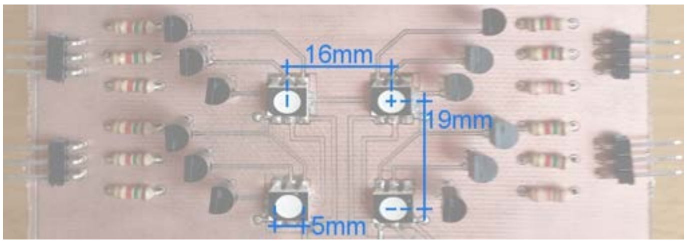

Figure V.3: Designed LED's board with the distances between its elements.

After the implementation of the board, the separations between the light sources were measured, obtaining horizontal distance of 16 mm, and vertical distance of 19 mm vertically. These values were used for calculating the theoretical pixels values applying equations III.28, and III.29. These theoretical values are showed on tables V.1, V.2, and V.3.

Table V.1: Calculated pixels for horizontal distance $d_x = 16mm$

γ	Distance (m)									
	0.20	0.40	0.60	0.80	1.00	1.20	1.40	1.60	1.80	2.00
45°	33.26	16.62	11.08	8.31	6.65	5.54	4.75	4.16	3.69	3.32
60°	40.71	20.36	13.57	10.18	8.14	6.79	5.82	5.09	4.52	4.07
75°	45.39	22.70	15.14	11.35	9.08	7.57	6.49	5.68	5.05	4.54
90°	46.99	23.50	15.67	11.75	9.40	7.84	6.72	5.88	5.22	4.70

Table V.2: Calculated pixels for vertical distance $d_y = 19mm$ when it is located in the object's side that is located closer to the camera

γ	Distance (m)									
	0.20	0.40	0.60	0.80	1.00	1.20	1.40	1.60	1.80	2.00
45°	57.41	28.31	18.78	14.06	11.23	9.35	8.01	7.00	6.22	5.60
60°	56.92	28.19	18.73	14.03	11.21	9.34	8.00	7.00	6.22	5.59
75°	56.37	28.05	18.67	13.99	11.19	9.32	7.99	6.99	6.21	5.59
90°	55.78	27.91	18.61	13.96	11.16	9.30	7.98	6.98	6.20	5.58

The light switching was controlled with a small single-board computer programmed with Python. Since an independent control of the LEDs 's color is required, each one is driven by three bipolar transistors (one for each color). The

Table V.3: Calculated pixels for vertical distance $d_y = 19mm$ when it is located in the object's side that is located farther from the camera

γ	Distance (m)									
	0.20	0.40	0.60	0.80	1.00	1.20	1.40	1.60	1.80	2.00
45°	54.25	27.52	18.43	13.86	11.10	9.26	7.94	6.95	6.18	5.57
60°	54.69	27.63	18.48	13.89	11.12	9.27	7.95	6.96	6.19	5.57
75°	55.21	27.76	18.54	13.92	11.14	9.29	7.96	6.97	6.20	5.58
90°	55.78	27.91	18.61	13.96	11.16	9.30	7.98	6.98	6.20	5.58

selected receiver was a commercial USB webcam. Logitech C920 [104], with diagonal FoV of 78°. The resolution was set to 640×480 pixels. The camera has high contrast, low brightness, and focus to infinity. The camera's shutter was controlled by a script for capturing frames with ISO 200 ($t_{EXP} = 1/1000$ s). The image acquisition was performed with a delay to assure the camera's stabilization and get the same parameters in each captured image. The camera was located on a rail to guarantee the alignment with the transmitter. Additionally, the experiment was performed in a dark room to eliminate interference from external light sources.

Once all the images were captured and stored, some image processing needs to be applied to determine the light sources' experimental pixel distance. Firstly, the images were binarized using Otsu thresholding method [103]. Next, the resulting images were eroded to eliminate imperfections; see figure V.4.

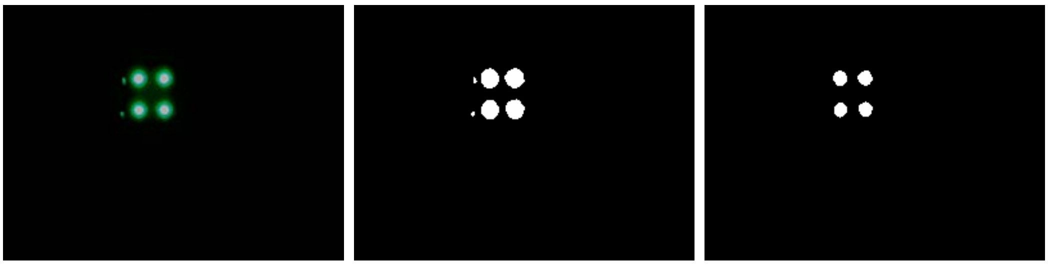

(a) (b) (c)

Figure V.4: Example of the projected pixels' estimation: photography taken at $D = 20$ cm with $\gamma = 75°$; all the LEDs turned on in green. **(a):** Original image; **(b):** Binarized image; **(c):** Eroded image.

A procedure for identifying the regions composed of the connected white pixels was performed over the new binary image. These regions should correspond to the light sources. Nevertheless, since the light sources were round LEDs, the regions' circularity was used for assuring this fact. As can be observed in table V.4, the regions obtained from figure V.4 has almost a perfect circularity (values close to one); therefore, those segments correspond to round-shaped objects.

For each identified region, labeled as shown in figure V.5, the obtained centroids' coordinates were used to determine the experimental horizontal, and vertical distances in pixels between the LEDs. The results from the example shown

Table V.4: Consecutive regions' characteristics of example in figure V.4

Region	Area	Centroids	Major Axis	Perimeter	Circularity
1	586	(255.67,138.62)	29.11	84.38	1.04
2	541	(256.18,197.26)	27.87	81.03	1.04
3	593	(302.67,138.05)	28.17	84.78	1.04
4	571	(303.08,196.60)	27.99	83.36	1.03

Areas, Major Axis Lengths, and Perimeters are in pixels. Centroids locations follow a (x,y) format. Circularity was calculated using equation III.2

in figure V.4 can be observed on table V.5. The calculated distances of each photography were stored. Finally, for each distance D, and angle γ the obtained distances (80 horizontal, 40 vertical for closer objects, and 40 vertical for farther objects) were compared with the estimated pixel separations, presented in tables V.1, V.2, and V.3.

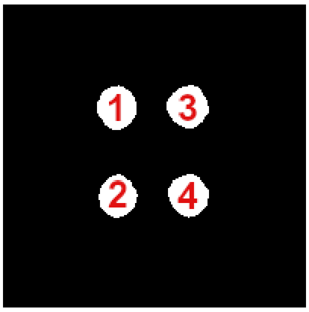

Figure V.5: Regions identified in figure V.4.

Table V.5: Calculated distances of example in figure V.5

Regions	Distance in pixels	Distance name
1 - 2	58.64	Vertical with object closer
3 - 4	58.55	Vertical with object farther
1 - 3	47	Horizontal
2 - 4	46.9	Horizontal

V.1.b Experimental results

The average error values of the experimentally measured distances compared with the predicted pixel separations are shown on table V.6 for the horizontal samples, and table V.7 for the vertical cases. As shown in the mentioned tables, the obtained average pixels' error was less than one pixel for all the cases with distance D greater than 40 cm. For the samples with closer distance ($D \leqslant 40$ cm), the maximum error was 2.7547 pixels, representing the 6.07% of the experimental value.

These higher values resulted from two main factors: the minimum focus distance and the theoretical projected pixel separation size. When the camera focus is set to infinity, as in this experiment, the minimum focus distance change from 7 cm to 40 cm; therefore, the images took at $D \leqslant 40$ cm were out of focus. This condition added undesired pixels to the light sources' projections, changing the centroids' coordinate location and possibly increasing the calculated distances. Additionally, since the projected pixels' amount decreases with the object's separation from the camera, the theoretical number of projected pixels between the center of the LEDs for these two positions is the greater ones. Consequently, a more significant absolute pixel error can be expected.

Table V.6: Average error for horizontal measurements in pixels

γ	Distance (m)										Average
	0.20	0.40	0.60	0.80	1.00	1.20	1.40	1.60	1.80	2.00	
45°	2.00	1.00	0.61	0.31	0.28	0.33	0.23	0.32	0.26	0.25	0.56
60°	2.23	1.73	0.77	0.71	0.30	0.38	0.35	0.28	0.20	0.22	0.72
75°	2.75	1.69	0.48	0.32	0.55	0.18	0.50	0.27	0.20	0.16	0.71
90°	0.45	1.15	0.76	0.51	0.36	0.22	0.26	0.27	0.24	0.20	0.44

Table V.7: Average error for vertical measurements in pixels

γ	Distance (m)										Average
	0.20	0.40	0.60	0.80	1.00	1.20	1.40	1.60	1.80	2.00	
45°	2.14	0.65	0.37	0.15	0.22	0.25	0.19	0.22	0.15	0.29	0.46
60°	2.75	1.11	0.51	0.19	0.37	0.20	0.17	0.14	0.23	0.27	0.59
75°	2.40	1.24	0.69	0.19	0.27	0.19	0.20	0.15	0.21	0.28	0.58
90°	0.85	0.93	0.78	0.29	0.32	0.23	0.15	0.21	0.17	0.23	0.42

In general, taking into account only the samples from pictures taken at positions above the minimum focus distance, the horizontal pixel's mean error was 0.3529 pixels (4.37%), and the vertical pixel's mean error was 0.2648 pixels (2.73%). Since the mean error was less than one pixel in all these cases, and the average measurement error was 3.76%, the proposed equations' usability for estimating the 2D pixels' projection, horizontal, and vertical sizes, of real-world objects in a photograph, was validated.

V.2 NPSIR's calculation

With the previous experiment, the usability of equations III.28, and III.29 for estimating pixels' separations was adequately validated. The next step in the research was to predict close-emitters' interference over an OCC communication link. Afterward, this interference can be added to the environmental light interference for determining the system's capabilities by applying superposition. The relation NPSIR, introduced in section III.7, can be used to directly quantify the impact of relative close emitters over the communication's link performance. Accordingly, the values of NPSIR for the different color channels (red, green, and blue) with known distances between the sources were required for the characterization of the close-emitters' interference in the system. For measuring the NPSIR, a laboratory experiment in the darkroom was designed using the same elements from the previous experiment described in section V.1. The darkroom was used for measuring only the interference from the close emitters, without possible disturbance from external factors. When these values were experimentally measured, they were used for calculating the BER of a defined system. Then the predicted values were compared with the simulated system's outcomes. This process will be described in detail in section V.3.

V.2.a Experimental setup

For this experiment, the board was placed with both angles, β, and γ, fixed to 90°, therefore, the LEDs were aligned with the camera. The distance D between the emitters and the receiver changed within three values: 100 cm, 140 cm, and 200 cm. The board was programmed to turn on the LEDs for each color (blue, green, red, and white) following a predefined sequence: one at the time (4 images), two horizontal at the time (2 images), two vertical at the time (2 images), two diagonal at the time (2 images), and all simultaneously (1 image).

As shown in figure V.6, the experiment had four phases: image acquisition; image's ROI extraction; image's ROI masking;, and NPSIR's analysis. A script was used for acquiring and storing the 44 photographs at each position. The other procedures will be explained in detail.

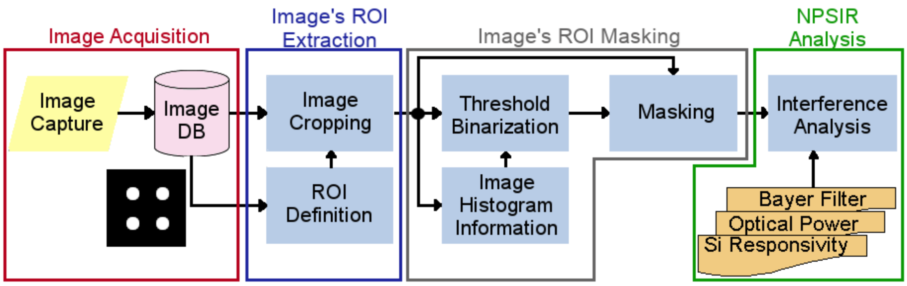

Figure V.6: Optical interference experimental calculation procedure.

Image's ROI extraction

For each selected distance, the all-white LEDs image was used for extracting the ROI, which contains the four sources. This image was binarized using the Otsu thresholding method. The resulting image was dilated using a disk of two pixels as the structuring element. Figure V.7 shows an example of the dilated image. Then a segmentation was performed over the dilated binary image into consecutive regions that correspond to the LEDs. Two characteristics were extracted from the regions: centroids' location and maximum axis length. These data was used to determine the ROI's edges using equations V.1. An example of this process results are shown in tables V.8, and V.9. Finally, these values were employed to crop each acquired image.

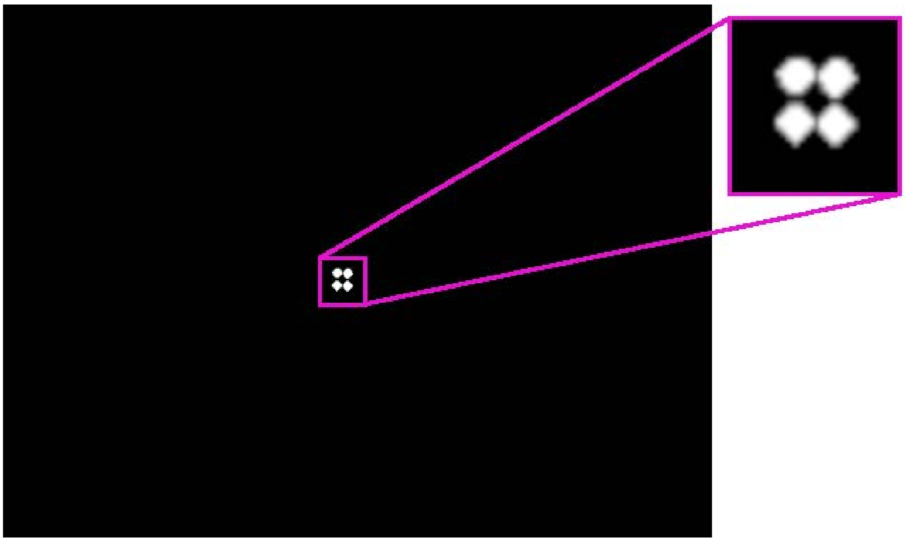

Figure V.7: Dilated binary image for distance $D = 100$ cm.

$$\begin{cases} Left & = min(x_S) - max(\frac{round(length_S)}{2}) \\ Right & = max(x_S) + max(\frac{round(length_S)}{2}) \\ Top & = min(y_S) - max(\frac{round(length_S)}{2}) \\ Bottom & = max(y_S) + max(\frac{round(length_S)}{2}) \end{cases} \tag{V.1}$$

Table V.8: Regions' characteristics of image in figure V.7

Regions	Centroids' locations	Major Axis Length
1	(302,242)	8.46
2	(302,254)	8.16
3	(312,243)	8.60
4	(312,254)	8.16

Table V.9: ROI's edges for images taken at 100 cm

Point	location in pixels
Left	297
Right	317
Top	237
Bottom	259

Image's ROI masking

Each ROI was binarized. In this case, the binarization was performed by analyzing the image histogram. The threshold was set to the value that accumulates the 95% of the total pixel's amount. This binary image was used as a mask (see figure V.8). The pixels from the transmitting LED (Pix_S) were determined by applying the corresponding mask to the appropriate channel (see figure V.8(c)). In the same way, the pixels from the close by interference LED (Pix_I) were calculated by masking with the same binary image, the photograph that contains the next horizontal or vertical LED (figure V.8(d)).

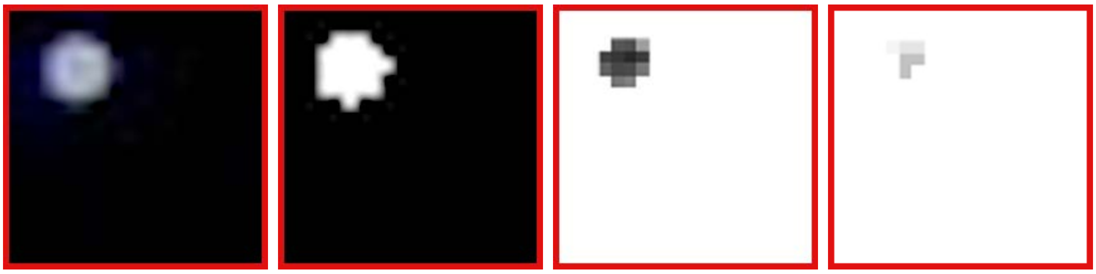

(a) (b) (c) (d)

Figure V.8: Image processing phase. **(a):** original image; **(b):** binary mask; **(c):** non-zero pixels of the emitting LED's image; **(d):** non-zero pixels of the interference signal.

NPSIR's analysis

For calculating the NPSIR, as shown in equation III.33, pixel count was executed. Additionally, using an optical spectrum analyzer, the optical power emitted by each LED of the board was obtained. The optical power data were determined by sampling wavelengths from 385 nm to 745 nm with steps of 5 nm. figure V.9 shows the particular case of LED1 (top left in figure V.2). In the same way, the Bayer filter response (figure V.10) and the silicon responsivity (figure V.11) of the selected camera were obtained from its digital image sensor datasheet [104]. Since the values related to the optical power, the CFA, and the silicon response were sampled, a numerical integration of equation III.33 is needed. Additionally, the outcome of this experiment is required in dB. For fulfilling these constrains equation V.2 was deduced. The NPSIR was calculated for each selected distance: 100 cm, 140 cm, and 200 cm; with transmissions in four colors: blue, green, red, and white (generated by RGB combination).

$$NPSIR_{dB} = 20 \cdot log\left[\frac{Pix_S}{Pix_I} \cdot \frac{\sum_{\lambda=385}^{745}\left(P_I(\lambda)R(\lambda)F_S(\lambda)\right)}{\sum_{\lambda=385}^{745}\left(P_S(\lambda)R(\lambda)F_S(\lambda)\right)}\right] \tag{V.2}$$

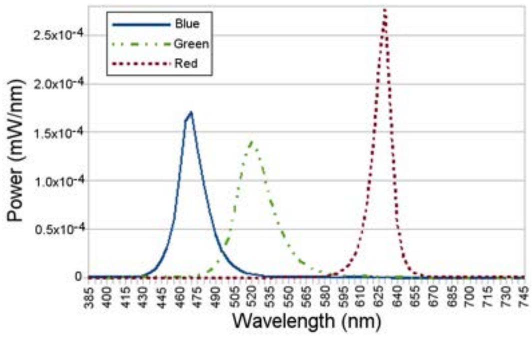

Figure V.9: Optical power emitted by the top left LED of the designed board

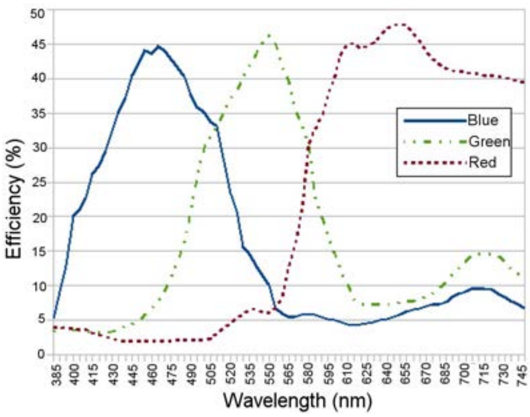

Figure V.10: Webcam Bayer filter response for blue, green, and red respectively.

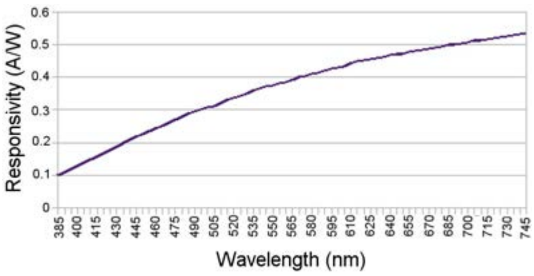

Figure V.11: Webcam silicon responsivity.

V.2.b Calculated NPSIR

Since the NPSIR was calculated for transmission in different colors, the results were grouped by transmitted channel. Additionally, the calculations were performed for the three selected distances. From the results can be concluded that these distances corresponded to three cases: entirely separated sources (D = 100 cm), a limited separation between the sources (D = 140 cm), and critically close sources (D = 200 cm). As expected, the worst-case scenario was the transmission of white light (see figure V.12), which is affected by the three channels, resulting in lower NPSIR values.

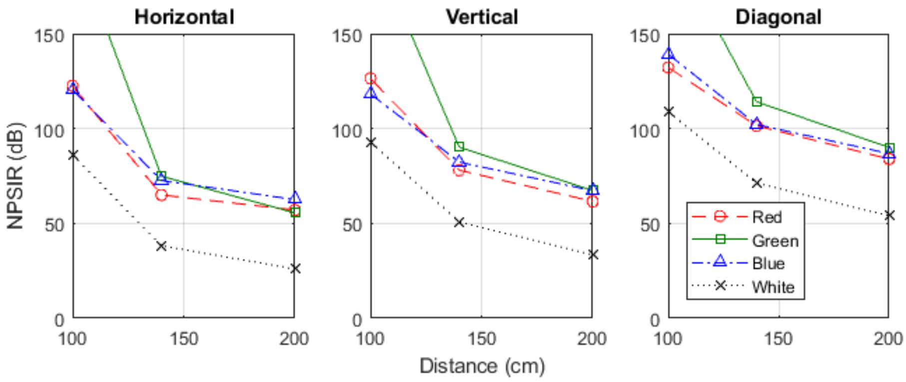

Figure V.12: NPSIR for transmitting in white.

Additionally, when the legit emitter's transmission and the additional light source is done in the same wavelength, or the interference comes from a device emitting white light, the NPSIR reaches the lowest results affecting the data communication. For the perfect spatial separation of the sources, the NPSIR represents minimum interference, above $86dB$, demonstrating that the communication link would not be affected by the close-emitter interference. Since the spatial inter-symbol interference from close-emitters working in the same wavelength affects the system significantly, the smart use of the three color channels should be introduced in the system design stage.

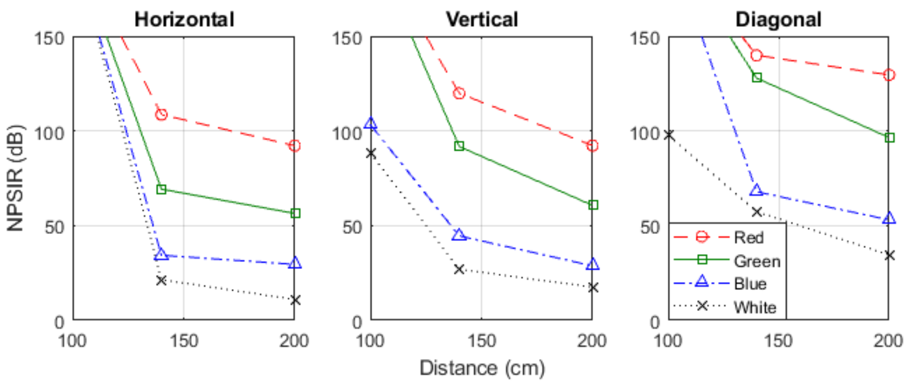

Figure V.13: NPSIR for transmitting in blue.

However, the results showed a dependency on the selected wavelength for the limited and critical spatial separation. For the transmissions in blue (figure V.13) and red (figure V.14), the interference came from close sources emitting in green, while the LED transmitting in green (figure V.15) was affected similarly by emissions in blue and red.

V.3 NPSIR's validation

As proposed in chapter III, the calculated NPSIR can be used for estimating the impact of close-emitter interference over real scenarios of OCC implementations.

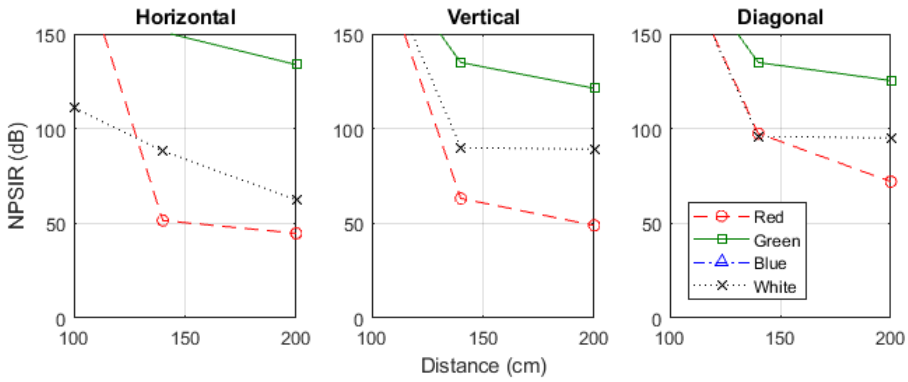

Figure V.14: NPSIR for transmitting in red.

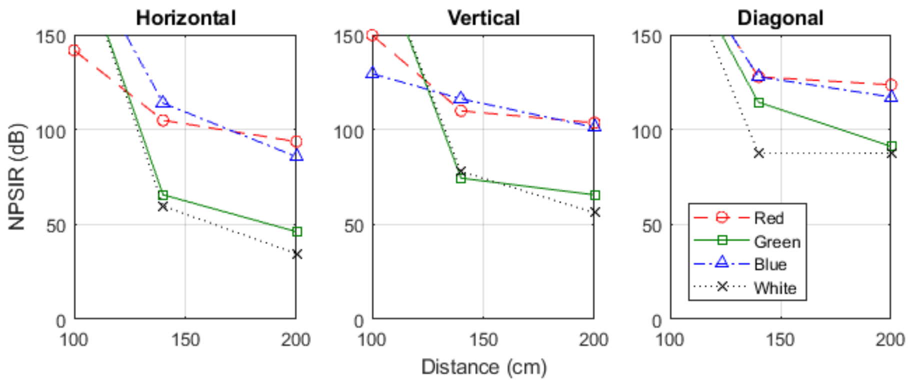

Figure V.15: NPSIR for transmitting in green.

Since these estimations are based on equations, the process is quick and simple. To validate the usability of the NPSIR for this particular purpose, a comparison between the simulated system's BER and the calculated values using the already obtained NPSIR measurements was proposed. In this case a basic indoor WSN, shown on figure V.16, was designed. The scenario was a windowless 3.00m length x 3.00m height x 3.00m width room for avoiding external light interference.

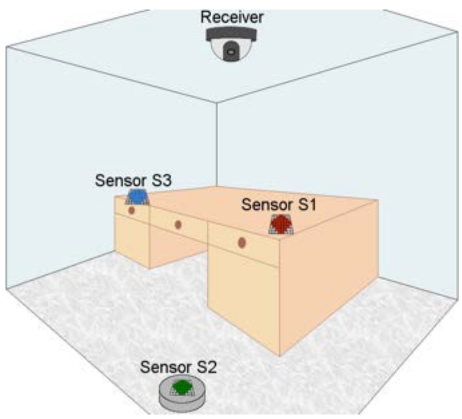

Figure V.16: Simulated indoor WSN scenario.

V.3.a Simulation setup

A global shutter dome camera with diagonal FoV of 90°, and resolution of 640 × 480 pixels, installed on the ceiling, was selected as the receiver. This camera was set up with a frame rate of 30fps, high contrast (255), low brightness (zero), and exposure time of 1/1000 s. Three sensors (S_1, S_2, S_3) were allocated in the office, each with an optical emitter. An 4 × 4 RGB LED matrix with viewing angle of 10° was selected as transmitter, and modeled with specific dimensions: 2.00 cm length, 2.00 cm width, and 0.40 cm height. For simplicity, each matrix turns on 12 LEDs in a circle shape that was assumed as a unique source. The optical power was defined as the summation of all the elements' contributions.

Two sensors (S_2 and S_3) were modeled with a dynamic location. Sensor S_2 (transmitting in green) was represented over an autonomous vacuuming robot with 9.10 cm height, while S_3 (emitting in blue) was over a desk of 80 cm height. Finally, S_1 (transmitting in red) was modeled with a fixed location over the same desk. Since the close-emitters interference when the transmitters are working on the same wavelength affects the system significantly, the three sensors used a specific color channel for reducing the effect.

The selected modulation for this scenario was OOK with non-return to zero (NRZ) line coding. For this simulation, it was assumed that the matrices are not part of the room illumination system, and the flickering effect was not taken into account. Therefore, the modulation does not use undersampling methods. Since each bit is sampled twice, the bit rate was set to 15 bps.

As the synchronization method, an adaptation of the frame selection technique proposed in [24] was applied for each transmission's three first frames. The message's header (1×AA) ensures at least one bit 1 among those three frames, which has the maximum average pixel intensity (k_{max}). For each frame a bit value is determined based on pixel intensity value (k), following equation V.3. As shown in figure V.17, if the two first bits are the same while the third one is different, the signal is synchronized. When the last two bits are equal while the first one is different, the signal is considered unsynchronized (case 1). In this case, the first frame is dropped, and the remaining ones are considered synchronized. Finally, if the first and the last bits are equal, the signal cannot be used (unsynchronized - case 2), and the emitter needs to restart the transmission.

$$\text{bit} = \begin{cases} 0 & k < \frac{k_{max}}{2} \\ 1 & \text{otherwise} \end{cases} \tag{V.3}$$

Equations III.28, and III.29 were used to determine the proportional separation distances between the emitters, and also their projected diameter. During the simulation, a different projection from each source was assumed. As shown in figure V.18, the sensors over the desk (S_1, and S_3) had a wider disk representation than the sensor over the vacuum cleaner (S_2) due to the height's difference.

For comparison purposes, the first step was to perform the simulation of the proposed scenario. The Monte Carlo method [105] was selected for the base-line simulation. A total of 10^6 bits were transmitted for each projected distance. For

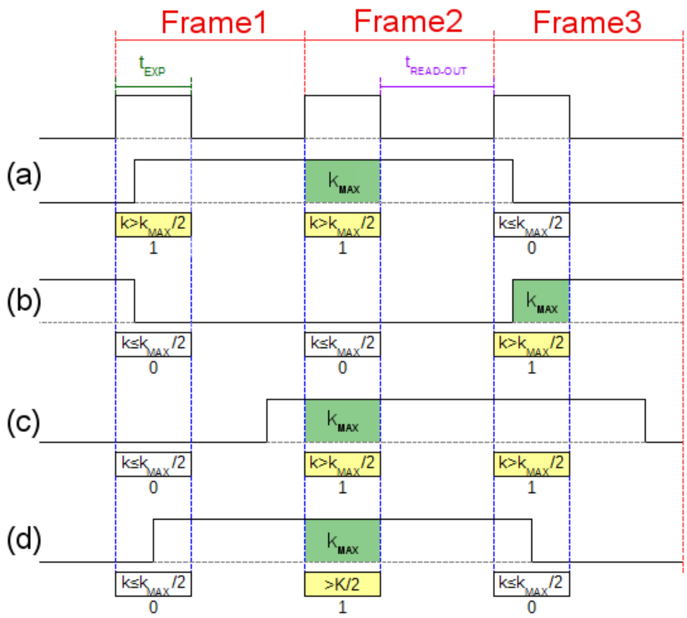

Figure V.17: Possible cases of the synchronizing procedure. **(a):** synchronized signal with two consecutive ones; **(b):** synchronized signal with two consecutive zeros; **(c):** unsynchronized signal - case 1; **(d):** unsynchronized signal - case 2.

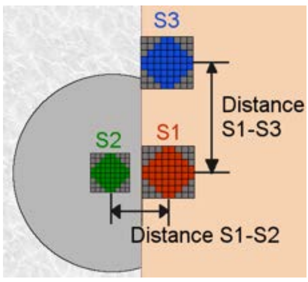

Figure V.18: Dome camera perspective of the sensors.

this simulation, the transmitted signal delay (τ_{Signal}) was assumed as a uniformed distributed variable. Additionally, the interference signal was turned on all the time, assuming the worst-case scenario, while the user signal could change its value depending on the bit that was representing.

The optical power received by the camera was defined as the sum of the legit signal and the interference. The amplitude of the legit signal and the interference were calculated using the individual optical power of the RGB LEDs employed in the previous experiment (Section V.2). Then for obtaining the corresponding projection, this power influence was limited to the exposure time (t_{exp}) in each color channel (red, green, and blue), taking into account the Bayer filter's response and the Silicon responsivity. For simplicity, the Bayer filter's response and the Silicon responsivity were assumed equal to those of the Logitech C920 webcam. Since this simulation's goal is to measure the impact of the interference, the analysis focused on the affected pixels instead of the whole frame, speeding up the process. However, the simulation was time and resource consuming.

As stated in the introduction of this validation, the NPSIR can be used for calculating the impact of the close-emitters interference over the communication link. For determining the relation between the legit signal, and the interference, Signal to Interference Ratio (SIR), that in an image is represented as the pixels' relation Pix_S/Pix_I, equation V.4 was applied using the NPSIR presented in section V.2. Then the BER for the OOK modulation under the described conditions was determined by equation V.5 presented in [106]

$$\mathrm{SIR} = \frac{\mathrm{Pix}_S}{\mathrm{Pix}_I} = \frac{\sum_{\lambda=385}^{745} P_S(\lambda)R(\lambda)F_S(\lambda)}{\sum_{\lambda=385}^{745} P_I(\lambda)R(\lambda)F_S(\lambda)} \cdot 10^{\frac{\mathrm{NPSIR_{dB}}}{20}} \tag{V.4}$$

$$\mathrm{BER_{OOK\text{-}NRZ}} = \frac{1}{2} \cdot erfc\left(\frac{1}{2\sqrt{2}} \cdot \sqrt{\mathrm{SIR}}\right) \tag{V.5}$$

V.3.b Simulation's results

The BER values obtained from the Monte Carlo simulation are presented in table V.10. Since 10^6 bits were transmitted for each projected distance. When the communication was error-free, a BER value of $1 \cdot 10^{-6}$ was assumed. The directly calculated values are presented in table V.11. These results are similar to the outcomes of the simulation.

Nevertheless, the values from the application of the NPSIR formula were slightly greater than the values obtained from the simulations, showing that the NPSIR provides an upper limit of the system's BER. As expected, the transmission from S_1 was more affected by the interference from S_2 than by the light from S_3, demonstrating that the red channel is more sensitive to the green light interference.

Table V.10: BER Results from the Monte Carlo Simulation

Distance	**S1 over S2**	**S2 over S1**	**S1 over S3**	**S3 over S1**
2.03	$4.84 \cdot 10^{-4}$	$2.53 \cdot 10^{-5}$	$5.09 \cdot 10^{-4}$	$2.00 \cdot 10^{-6}$
2.31	$1.32 \cdot 10^{-4}$	$1.24 \cdot 10^{-5}$	$5.40 \cdot 10^{-5}$	$1.00 \cdot 10^{-6}$
2.41	$1.14 \cdot 10^{-4}$	$9.00 \cdot 10^{-6}$	$2.00 \cdot 10^{-6}$	$< 1.00 \cdot 10^{-6}$
2.74	$2.10 \cdot 10^{-5}$	$2.00 \cdot 10^{-6}$	$< 1.00 \cdot 10^{-6}$	$< 1.00 \cdot 10^{-6}$
2.90	$9.00 \cdot 10^{-6}$	$1.00 \cdot 10^{-6}$	$< 1.00 \cdot 10^{-6}$	$< 1.00 \cdot 10^{-6}$
3.30	$1.00 \cdot 10^{-6}$	$< 1.00 \cdot 10^{-6}$	$< 1.00 \cdot 10^{-6}$	$< 1.00 \cdot 10^{-6}$
3.45	$< 1.00 \cdot 10^{-6}$	$< 1.00 \cdot 10^{-6}$	$< 1.00 \cdot 10^{-6}$	$< 1.00 \cdot 10^{-6}$
3.92	$< 1.00 \cdot 10^{-6}$	$< 1.00 \cdot 10^{-6}$	$< 1.00 \cdot 10^{-6}$	$< 1.00 \cdot 10^{-6}$

V.4 Positioning, and tracking system

With the experiments presented in sections V.1, and V.3 the benefits of using equations III.28, and III.29 for predicting the number of pixels projected on an

Table V.11: BER results estimated from applying the NPSIR value

Distance	S1 over S2	S2 over S1	S1 over S3	S3 over S1
2.03	$5.44 \cdot 10^{-4}$	$2.88 \cdot 10^{-5}$	$5.52 \cdot 10^{-4}$	$2.51 \cdot 10^{-6}$
2.31	$2.00 \cdot 10^{-4}$	$1.41 \cdot 10^{-5}$	$6.16 \cdot 10^{-5}$	$2.48 \cdot 10^{-6}$
2.41	$1.32 \cdot 10^{-4}$	$1.06 \cdot 10^{-5}$	$2.44 \cdot 10^{-6}$	$2.29 \cdot 10^{-6}$
2.74	$2.81 \cdot 10^{-5}$	$3.48 \cdot 10^{-6}$	$1.13 \cdot 10^{-7}$	$8.80 \cdot 10^{-8}$
2.90	$1.73 \cdot 10^{-5}$	$1.76 \cdot 10^{-6}$	$3.25 \cdot 10^{-8}$	$2.53 \cdot 10^{-9}$
3.30	$2.41 \cdot 10^{-6}$	$8.40 \cdot 10^{-8}$	$2.28 \cdot 10^{-8}$	$1.71 \cdot 10^{-9}$
3.45	$2.10 \cdot 10^{-7}$	$4.32 \cdot 10^{-9}$	$1.42 \cdot 10^{-8}$	$1.92 \cdot 10^{-10}$
3.92	$1.73 \cdot 10^{-8}$	$4.66 \cdot 10^{-12}$	$1.89 \cdot 10^{-12}$	$1.64 \cdot 10^{-11}$
4.06	$1.09 \cdot 10^{-9}$	$1.65 \cdot 10^{-13}$	$7.38 \cdot 10^{-13}$	$1.24 \cdot 10^{-16}$
4.62	$6.50 \cdot 10^{-13}$	$< 1.00 \cdot 10^{-13}$	$< 1.00 \cdot 10^{-13}$	$< 1.00 \cdot 10^{-13}$
4.82	$< 1.00 \cdot 10^{-13}$	$< 1.00 \cdot 10^{-13}$	$< 1.00 \cdot 10^{-13}$	$< 1.00 \cdot 10^{-13}$
5.48	$< 1.00 \cdot 10^{-13}$	$< 1.00 \cdot 10^{-13}$	$< 1.00 \cdot 10^{-13}$	$< 1.00 \cdot 10^{-13}$

image have been validated as well as the usability of the NPSIR for estimating the impact of close-emitters interference impact over an OCC communication system. The next step in the research was to demonstrate possible real applications of OCC for IoT. At first, an industrial indoor application that also can be employed for outdoor purposes was proposed. This real-time two-step 3D positioning and tracking system was proposed on [51, 52].

As shown in Fig.V.19, the system employs four beacons (B_1 - B_4) for the concurrent localization of several objects (O_n). The beacons are positioned at a predefined static distance from the camera's normal plane, forming a virtual plane representing the projected frame.

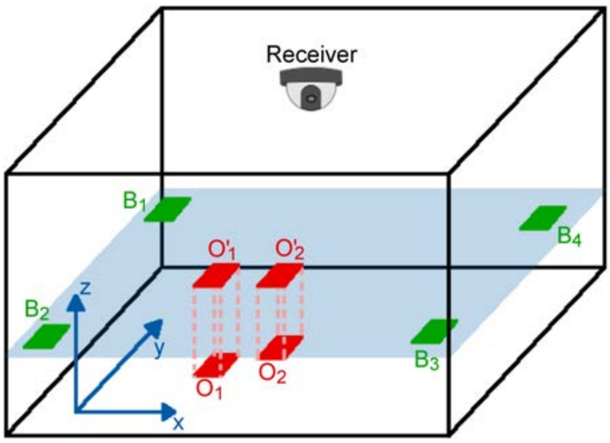

Figure V.19: Proposed system's scheme. In this example, a single ceiling security camera is used as receiver; the four beacons (B_1 - B_4) form the virtual plane;, and two objects (O_1, and O_2) are to be located.

A simplified version of equations III.28, and III.29 is applied to obtain the horizontal (equation V.6), and vertical (equation V.7) separation between the objects, and the beacons. In the same way, the relation between the beacons', and the objects' projection size, as shown in equation V.8, is used to determine the distance of each object to the camera. Afterward, the distance from the object to each beacon ($r_{\mathrm{OB}i}$) can be calculated by applying equation (V.9), and the object three dimensions (3-D) location is obtained from simple trilateration, based on the known positions of the beacons.

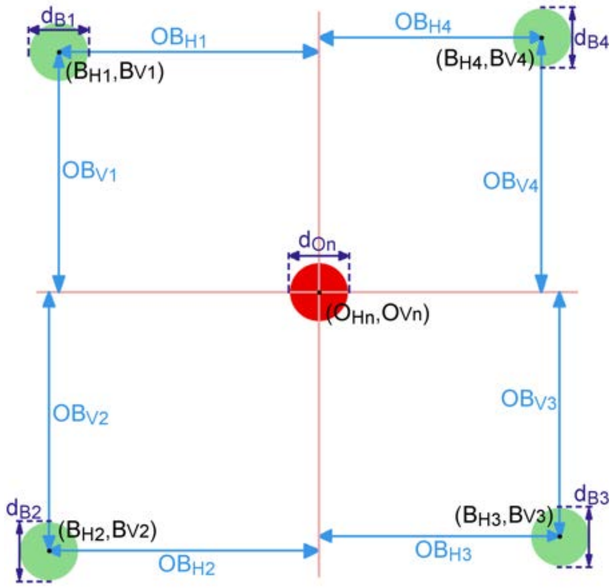

Figure V.20: Representation of the data necessary for the localization process.

$$H_{\mathrm{img}} = \frac{2}{\varphi_H}\left[\tan^{-1}\frac{H_{\mathrm{real}}}{2D}\right] \implies H_{\mathrm{real}} = 2D \cdot \left[\tan\frac{H_{\mathrm{img}} \cdot \varphi_H}{2}\right] \tag{V.6}$$

$$V_{\mathrm{img}} = \frac{2}{\varphi_V}\left[\tan^{-1}\frac{V_{\mathrm{real}}}{2D}\right] \implies V_{\mathrm{real}} = 2D \cdot \left[\tan\frac{V_{\mathrm{img}} \cdot \varphi_V}{2}\right] \tag{V.7}$$

$$D_{\mathrm{O}i} = D \cdot \frac{tan\dfrac{d_{\mathrm{B}i} \cdot \varphi_H}{2}}{tan\dfrac{d_{\mathrm{O}} \cdot \varphi_H}{2}} \tag{V.8}$$

$$r_{\mathrm{OB}i} = \sqrt{OB_{Hi}^2 + OB_{Vi}^2 + (D - D_{\mathrm{O}i})^2} \tag{V.9}$$

To demonstrate the viability of the proposed system, an experimental validation was performed in a 3 m × 3.5 m × 2.5 m dark room. During this process, four objects were located and tracked simultaneously.

V.4.a System setup

As emitters, the beacons, and the objects used a LEDs' matrix (see figure V.21), composed by sixteen 6-pin RGB LEDs with viewing angle of 120°. In this way, each color of the LEDs was controlled independently. For simplicity in the projected sources' dimensions comparison, a round shape was selected. Therefore, only twelve LEDs were used for signaling. Additionally, a light diffuser panel was used for assuring that the arrangement worked as a single light source.

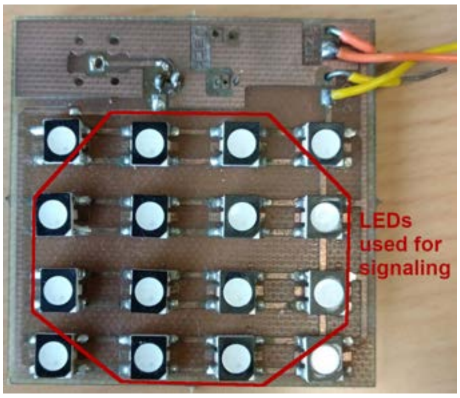

Figure V.21: Synchronization Scheme.

Each color channel was independently controlled by a small single-board computer programmed with Python. In this way, the sources can transmit their unique identification signal. The beacons used only the green LEDs, while the objects employed blue and red ones. The identification signal was the OOK modulation of code '0×AAAA' with specific switching frequency for each element (beacon or object), as defined in table V.12.

Table V.12: Frequency of the Devices' Identification Signal

Device ID	Frequency (Hz)	Color Channel
B_1	2400	Green
B_2	1200	Green
B_3	600	Green
B_4	900	Green
O_1	1200	Red
O_2	2400	Red
O_3	1200 / 2400	Red / Blue
O_4	2400	Blue

The beacons were located at a predefined distance $D = 2.00$ m to the camera's normal plane forming a virtual referential plane. For guaranteeing this distance during the testing, all the emitters were stationed in different positions over a 2.0 m × 2.0 m × 0.2 m board on the room's floor. The beacons (B_1 - B_4) were kept in static known positions, while the objects (O_1 - O_4) were moved over a specific area of the board, as shown in table V.13.

Table V.13: Emitter's 3-D positions

Device ID	Position (m)		
	x	y	z
B_1	1.00	2.00	0.02
B_2	1.00	0.50	0.02
B_3	3.05	0.50	0.02
B_4	3.05	2.00	0.02
O_1 - O_4	1.80 - 2.25	1.10 - 1.50	0.02

A rolling shutter USB webcam with diagonal FoV of 78° was used as the receiver. It captured frames at 30 fps with resolution of 640×480, then $N_V = 480$. The camera was set up to high contrast (255), low brightness (zero), and focus on infinity (zero). Due to the rolling shutter effect, the transmitted code was observed as light strips, as shown in figures V.22, and V.23. The theoretical band's widths were calculated using equation IV.2, and the results can be observed on table V.14.

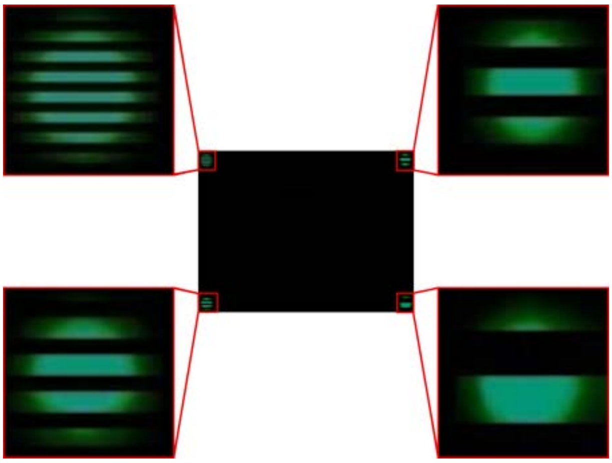

Figure V.22: Experimental image of the four beacons (B_1 - B_4) extracted from the first frame.

Table V.14: Theoretical Band's widths

Device ID	Band's width (pixels)	Color Channel
B_1	3	Green
B_2	6	Green
B_3	12	Green
B_4	8	Green
O_1	6	Red
O_2	3	Red
O_3	6 / 3	Red / Blue
O_4	3	Blue

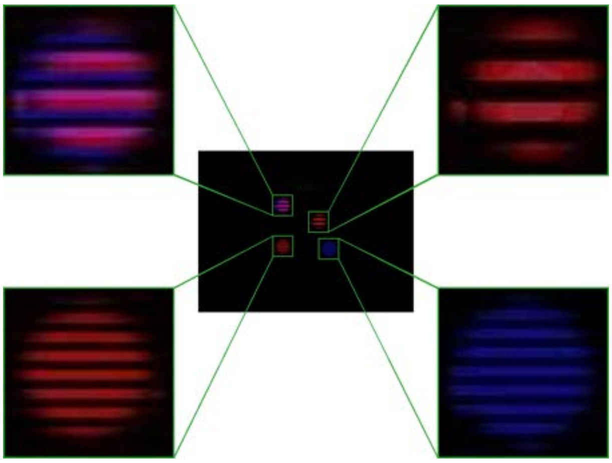

Figure V.23: Experimental image of the objects to be located simultaneously (O_1 - O_4).

For determining the objects' 3D position, the information of the emitters' pixel locations was extracted, and the sources were identified based on the strip's width during the "Image Processing" phase. In the beacons' case, the location was obtained only from the first frame for speeding up the process. Afterwards, the position of the different objects is calculated using equations V.6, V.7, V.8, and V.9.

V.4.b Image processing

This experiment's image processing phase was divided into five procedures: binarization, dilation, segmentation for data extraction, ROI extraction, and bandwidth calculation for the source's identification. The image processing diagram shown in figure V.24.

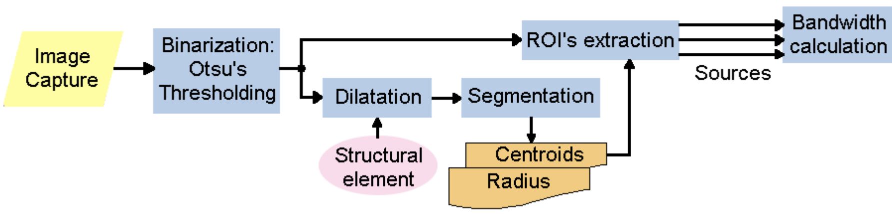

Figure V.24: Positioning system: image processing flow chart.

At first, the appropriated color channel was binarized using Otsu's algorithm for thresholding. For the beacons, the process is applied over the green channel of the first frame (see figure V.25). On the other hand, the binary image combines the binarization of blue and red channels for the objects.

Then, for transforming each source into an image region of consecutive pixels, the binary image is dilated. The selected structural element was an 8 pixels diameter disk to grow the size of the white bands symmetrically in all directions, and therefore, keeping the round shape of the emitters and the centroids' location

Figure V.25: Beacons' binarized image.

in the correct place. After this process, the light sources can be observed as closed white regions, as shown in figure V.26.

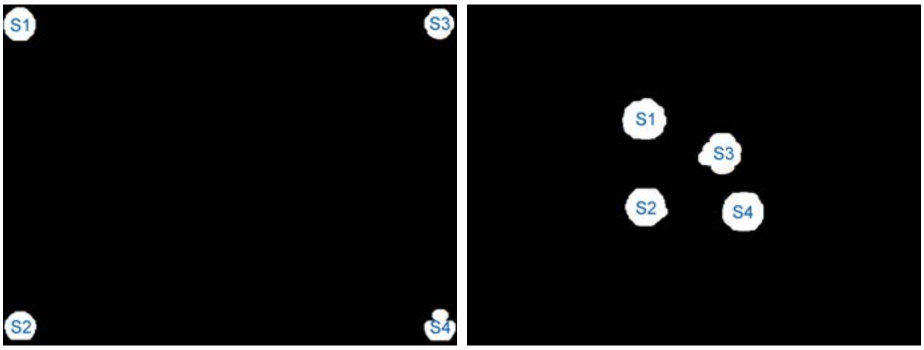

(a) (b)

Figure V.26: Experimental dilated binary image. At this stage, the emitters are perceived as independent white regions, and they have temporal labels (S_1 - S_4) associated. **(a):** Beacons from first frame; **(b):** Objects.

Then the binary image was segmented using a consecutive pixels' algorithm. The centroids' coordinates and maximum axis length of the resulting region were extracted. Since the LEDs has a round shape, the maximum axis length is the corresponding source's diameter. The table V.15 shows the results of this process for the beacons, while table V.16 presents an example for the objects to be located.

Table V.15: Beacons' extracted data

Beacon ID	Position (px)		Diameter (px)
	Horizontal	Vertical	
S1	25.28	29.13	43
S2	25.74	455.30	42.7
S3	615.24	27.00	42.9
S4	616.14	450.55	43

Table V.16: Objects' extracted data from example on figure V.26

Object ID	Position (px)		Diameter (px)
	Horizontal	Vertical	
S1	250.38	162.67	42.7
S2	252.87	285.65	42.8
S3	358.86	210.36	43.1
S4	389.80	292.13	43.2

The appropriated channel's ROI of each light source is extracted from the corresponding undilated binarized image. For cropping the images, the centroid's location, and the maximum axis length obtained in the previous step were applied to equation V.1. As shown in Fig. V.27, in the beacons' case, only one ROI is cropped from the green channel of the first frame for each light source. In the case of the objects, figure V.28, for each object to be located two ROIs are cropped; one from the red channel, and one from the blue channel.

(a) (b) (c) (d)

Figure V.27: Beacons' ROI for determining the corresponding source's code.**(a):** S1; **(b):** S2; **(c):** S4; **(d):** S3.

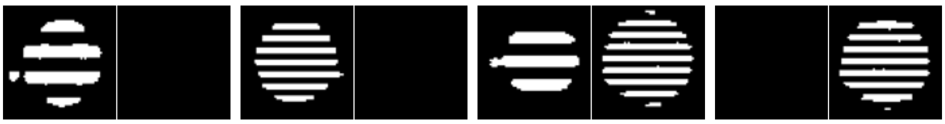

(a) (b) (c) (d)

Figure V.28: Objects' ROI for determining the corresponding source's code. The left image corresponds to the red channel while the right one represents the blue channel.**(a):** S3; **(b):** S2; **(c):** S1; **(d):** S4.

To identify the different light sources, the band's width $Npixels_i$ was calculated in each obtained ROI. This width was defined as the consecutive white pixels' statistical mode in the three central columns of each ROI's corresponding channel. These values were compared to the theoretical ones, and afterward, the sources were identified in function of the proximity to the real values. The results of the identification process can be observed on tables V.17, and V.18.

In this way, the pixel's horizontal and vertical location of each beacon (B_{Hi}, B_{Vi}) was matched with a known real 3-D position and stored by the system along with the source diameter (d_{Bi}). Similarly, for the objects to be located, the centroid's

Table V.17: Beacons' Identification results

Regions' ID	Band's width (pixel)	Beacons' ID
S1	3	B1
S2	5	B2
S3	8	B4
S4	14	B3

Table V.18: Objects' Identification results from example on figure V.26

Regions' ID	Bands' width (px)		Objects' ID
	Red	Blue	
S1	6	3	O3
S2	3	0	O2
S3	3	0	O1
S4	0	4	O4

horizontal and vertical pixel coordinates (O_{Hi}, O_{Vi}), and the source diameter (d_{Oi}) were recorded for further calculations.

These measures were employed to estimate, for each object, the distances to the different beacons' horizontal (equation V.6), and vertical (equation V.7) positions, and also the separation from the camera's normal plane (equation V.8.) Finally, the 3-D object's location was determined using trilateration by applying the values r_{OBi} calculated with equation V.9.

Additionally, all the locations were stored in a database. Each data entry included the position, the device identification, and the time stamp. Therefore, the objects can be tracked independently or by a group. Moreover, queries to the database can be done using the object's identification, a time range, or both parameters simultaneously.

As an example of this tracking process, a query about the object's movements O_1 throughout five minutes was made. During that period, the object was manually moved 5 cm at the time. At the beginning, the object was located at $(1.80, 1.10)$ m, then it was moved to the right until it reached the position $(2.25, 1.10)$ m. Afterward, O_1 advance up 0.40 m, followed by nine moves to the left. From there, the object shifted to location $(1.80, 1.40)$ m, and again to the right until position $(2.20, 1.40)$ m. Later O_1 went down 0.25 m then 0.35 m to the left, and 0.10 m up. Finally, the object moved right to the point $(2.10, 1.25)$ m.

V.4.c Position‘s results

In each (x,y) position over the moving area of the objects, four 3-D estimated locations were calculated, one per object. Table V.19 presents the calculated positions of the objects showed in figure V.26 based on the data from table V.16. For this selected example, the resolved positions showed a maximum error of 2.94 cm for x dimension, 3.04 cm for y dimension, and 0.93 cm for z dimension.

Table V.19: Located Objects' Positions for example in figure V.26

Source ID	Real Position (m)			Calculated Position (m)		
	x	y	z	x	y	z
O1	2.15	1.35	0.02	2.16	1.36	0.01
O2	1.80	1.10	0.02	1.78	1.09	0.02
O3	1.80	1.50	0.02	1.77	1.53	0.02
O4	2.25	1.10	0.02	2.28	1.07	0.03

In general, the position error range was between 0.16 cm, and 3.10 cm for x dimension, between 0.09 cm, and 2.65 cm for y dimension, and between 0.01 cm, and 1.32 cm for z dimension. figure V.29 shows the average error for each position. This average error position was appraised as a combination of the four measurements and the three dimensions. Moreover, the mean location error was 1.2404 cm, with an average processing time of 18.2 ms per frame. These results proved the applicability of such positioning system.

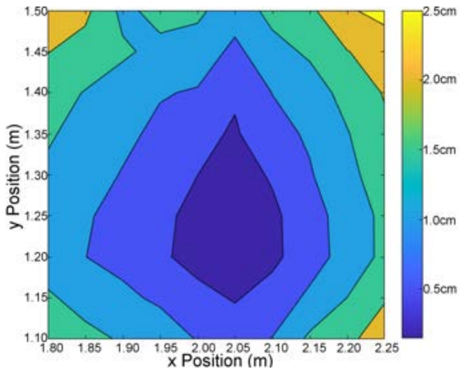

Figure V.29: Location's error map

V.4.d Tracking 'process results

The tracking of the selected object over five minutes started on the location $(1.77, 1.09)$ m, and ended at the position $(2.11, 1.25)$ m. The figure V.30 shows the tracking of object O_1 movements. The straight blue line represents the object's real path, while the dotted red line constitutes the system's track of the object. In this case, the maximum error location was 3.10 cm for x dimension, 2.65 cm for y dimension, and 0.48 cm for z dimension. Therefore, the tracking process can be employed when the objects to be located do not possess embedded cameras but own a LED.based device.

V.5 Outdoor wireless sensor network

With the previous experiment, the implementation of an IoT application was proved. However, the proposed system was designed for indoor purposes. For

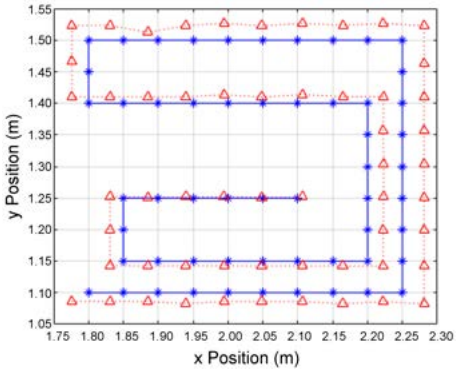

Figure V.30: Tracking experiment's results: the straight blue line represents the real path of the object, while the dotted red line constitutes the system track

this reason, another field experiment for an outdoor deployment was designed. In this case, the outdoor WSN system proposed on [64] was tested.

As shown in figure V.31, this outdoor system could use several cameras as receivers, including rolling and global shutter. Nevertheless, the light source state must be the same during the ROI scanning, emulating the global shutter acquisition technique. These cameras transmit the pictures to the cloud for off-line processing. The collected data is modulated and then applied for switching LED-based devices. One or more cameras can capture this signal.

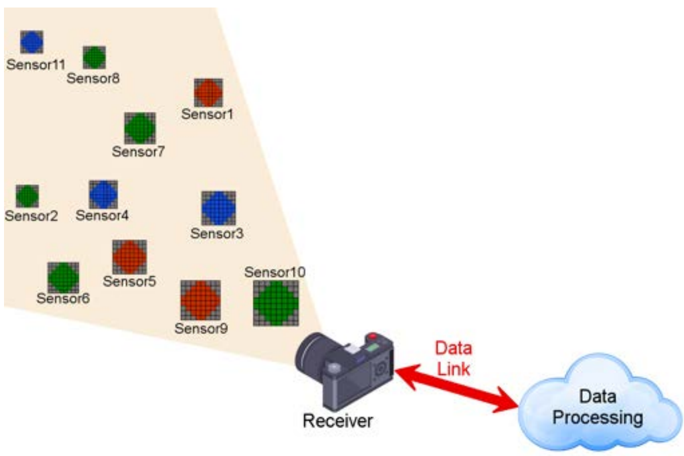

Figure V.31: Proposed outdoor WSN system: The emitters are LED-based devices, and the receivers are medium cost camera.

The proposed system requires at least a 2×2 pixel representation of each light source. therefore, equations III.28, and III.29, that have been validated previously, were used to determine the maximum distance (D_{MAX}) between the LED-based devices, and the cameras that assures that pixel projection.

V.5.a Experimental setup

To validate this outdoor WSN a field experiment was performed in Las Palmas de Gran Canaria (Spain). The test was carried out with a fresh breeze, wind speed of five in the Beaufort wind force scale ($29 - 38$ Km/h), and under the presence of haze. These atmospheric conditions were not optimal for establishing a communication link; however, they were realist conditions for the zone.

The selected emitter was a cross-shaped LED matrix of 48 cm $\times$ 48 cm emitting in green, see figure V.32. Since this LED-based device was operating for advertising a pharmacy, the flickering was expected and desired. Therefore, each bit was transmitted during two consecutive frames for assuring its reception without undersampling. The signal was modulated using OOK-NRZ. For synchronization, the process described in section V.3 was used.

Figure V.32: Outdoor WSN's transmitter.

The receiver was a rolling shutter smart-phone camera with horizontal FoV of 28.1°. In this case, the contrast and brightness were left as automatic, while the resolution was set to 1920×1080 pixels. The camera worked at 30 fps, the default camera's frame rate.

Based on the selected devices' characteristics: LED 's matrix, and camera; the maximum distance of the system was defined as 400 m. Since the pharmacy sign had a fixed location, the smart-phone camera was moved to a high place with LoS to the emitter. The devices' final locations assure a distance between the camera and the emitter lower than the calculated maximum value, 328 m.

The camera captured 20 short videos, each one of 30 seconds. In this particular case, the videos were recorded and stored temporally in the camera. Then they were copied to a computer for off-line processing. From each video, approximately 900 frames were extracted. Figure V.33 shows the first frame of one of these videos, highlighting the transmitter location.

In each frame, the LED matrix was represented by a disc of approximately 10 pixels diameter. Since the system knows the source's locations, the corresponding ROI is extracted frame by frame to speed up the operation. A 14×14 pixels ROI was selected to compensate a possible emitter's movement.

Based on previous videos' histograms, a fixed threshold for data recovery over the green channel was defined as 0.4118. In each ROI, the average pixel's intensity was calculated for the green channel. Then the data was recovered. If the intensity of two consecutive frames was greater or equal to the threshold,

Figure V.33: Outdoor WSN field experiment: image extracted from the first frame of one of the thirty seconds videos. The red box shows the location of the emitter

the bit was defined as "1"; otherwise, it was decoded as "0". From each frames' group, a maximum of 450 bits was extracted.

V.5.b Experimental results

The decoded data of the first video, figure V.34.(b), is similar in pattern to the emitted signal, figure V.34.(a). In this particular case, eight bits out of the 450 recorded bits were not recovered properly. therefore, the BER was 0.01778. As shown in Table V.20, the maximum error was ten bits (BER of 0.02222), obtained from the eighth video, while the minimum error was four bits (BER of 0.00889), and the mean error was 6.4 bits, resulting in an average BER of 0.01388. Therefore, the communication link's viability has been proved, and an outdoor OCC implementation for IoT has been validated. Nevertheless, the flickering problem requires additional research, and a distance-independent flickering-free modulation scheme, like the one proposed in chapter IV is needed.

V.6 Flickering-free distance independent modulation's validation

Finally, the proposed flickering-free distance independent modulation (Chapter IV) was validated. For this purpose, a two phases validation process was performed. During the first stage, a simulation was designed for validating the switching frequencies' selection procedure by using equations IV.6 and IV.10. The modulated signals generated with the calculated switching frequencies were used in the simulation as the light emitters' input. The obtained frames were stored, and the corresponding PCC values were calculated to demonstrate the frequency

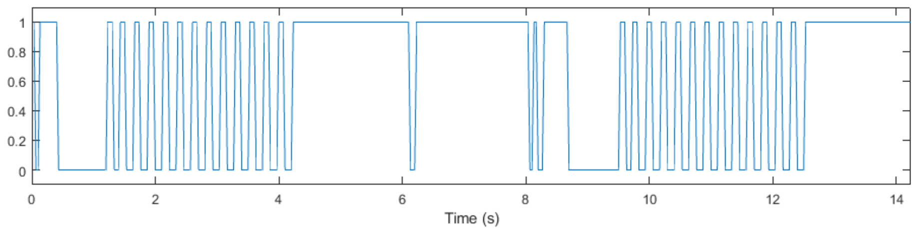

(a)

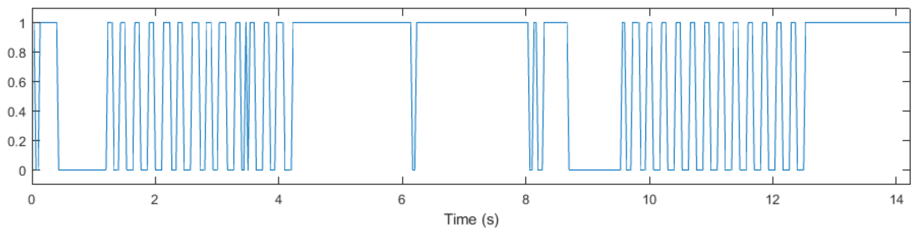

(b)

Figure V.34: Outdoor WSN Experiment results of the first video.**(a):** original data; **(b):** decoded data, for comparison purposes the delay in the decoded signal was eliminated;

Table V.20: Videos Bit Error Rate

Video's ID	Bits with error	BER
1	8	0.01778
2	4	0.00889
3	6	0.01333
4	5	0.01111
5	7	0.01556
6	5	0.01111
7	4	0.00889
8	10	0.02222
9	6	0.01333
10	5	0.01111
11	6	0.01333
12	4	0.00889
13	8	0.01778
14	6	0.01333
15	7	0.01556
16	5	0.01111
17	8	0.01778
18	8	0.01778
19	5	0.01111
20	7	0.01556

selection procedure's usability. In general, to demonstrate the effectiveness of the calculated frequency multiplier α, the resulting frames should have at least $\upsilon = 2$ light bands. Additionally, each light strip should be greater than five pixels wide. For validating the viability of selecting the switching frequencies using equation IV.6, the obtained PCC for each data symbol must fit within the range defined in section IV.3 by equation IV.3.

The second stage was a field experiment designed for calculating the BER, the success probability, and the transmission failure probability of the system. The proposed scheme's experimental implementation was done using switching frequencies for three different distance ranges to validate the scheme's independence from the distance. The experimental testing was designed to send data using the whole modulation scheme, including the wake-up process. Overall, the transmissions, the received data were compared to the sent information to obtain the number of symbols appropriately decoded and the bits that the system failed to recover. In this way, the BER was calculated along with the probability of transmitting each symbol successfully.

V.6.a Simulation setup

In this case, the frame acquisition process was simulated for a RaspberryPi camera with diagonal FoV of 67°. The camera's frame rate was set to 30 fps. To emphasize the light bands, a high contrast (255), low brightness (zero), and short exposure time (1/1000 s) were assumed. For speeding up the simulations, a basic image resolution (640×480 pixels) was selected. The emitter was a 10.00 cm $\times$10.00 cm white LED-based lamp with square shape., and the distance between the camera and the emitter was set to 0.25 m for assuring that the whole frame represents the light source while the environmental conditions can be neglected, therefore, the greatest range of α values can be evaluated.

From equation IV.6, the maximum value of the frequency multiplier α for the selected resolution ($N_y = 640$) is 64 ($\alpha < N_y/10$). On the other hand, since the whole frame represent the light source, and the minimum value of α is one ($f_{SW} = f_{CAM}$), the frame has at least two bands. When $f_{SW} = f_{CAM}$, the signal period corresponds to the frame's acquisition time ($t_{SW} = t_{CAM}$); therefore, the frame has a full light band and a complete dark strip. The frequency multiplier was set from 10 to 70. For all the cases, the number of extracted light strips should be greater than two. However, the number of projected pixels for each band at $\alpha = 70$ should be less than five, the number of pixels that assures the emitter's extraction with at least two bands for long-distances.

Using this range of α, the coupled switching signal's frequency varies from 300Hz to 2100Hz. For all the cases, it is expected that the PCC of consecutive frames for the different calculated switching frequencies are distinguishable. The values should not overlap, allowing the correct demodulation of the four symbols. A total of 7500 frames for each value of α were generated.

V.6.b Simulation's results

As a result of the simulation, 52500 frames were obtained. The figure V.35 shows two of the obtained binary images for $\alpha = 10$; $F_{Sw} = 300Hz$, and $\alpha = 50$; $F_{Sw} = 1500Hz$, where we must highlight two things: there are at least 19 strip lines, and each band has at least 7 pixels. In fact, since the minimum α value was set to 10, at least 18 full light bands were projected on the image. In the case of the bands' pixel width, with $\alpha = 70$ the frames showed values between four and five pixels, while lower frequency multipliers ($\alpha < 64$) produced frames with bands of at least five pixels that can be easily extracted from longer distances. With these results, the proposed limits for the frequency multiplier has been validated.

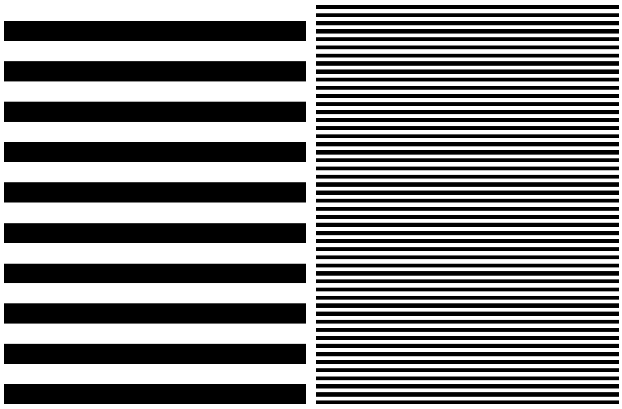

(a) (b)

Figure V.35: Simulated binary image. **(a):** $\alpha = 10$; $F_{Sw} = 300Hz$; **(b):** $\alpha = 50$; $F_{Sw} = 1500Hz$.

On the other hand, as can be seen in table V.21, and figure V.36, for all the selected values of the frequency multiplier α, the obtained PCC values of the consecutive frames for the selected frequencies corresponding to the data symbols were within the proposed ranges, without overlapping. In this way, the signals that correspond to the different symbols can be separated adequately. These results validate the calculated switching frequencies, and therefore, the equation IV.10. Nevertheless, this simulation was done without external interference and for a short distance. For validating the modulation scheme, field experimentation is needed. In this way, the impact that the environmental conditions, including external interferences such as other illumination sources, the camera's frame rate fluctuations, and changes in the distance could have over the modulation scheme can be tested.

V.6.c Experimental setup

As stated in the previous subsection, a field test is required for validating the proposed modulation scheme under realistic conditions. For this experiment the emitter was the commercial LED-based square panel shown in figure V.37. Despite a lamp dimension of 60×60 cm^2, the effective area is 59.5×59.5 cm^2.

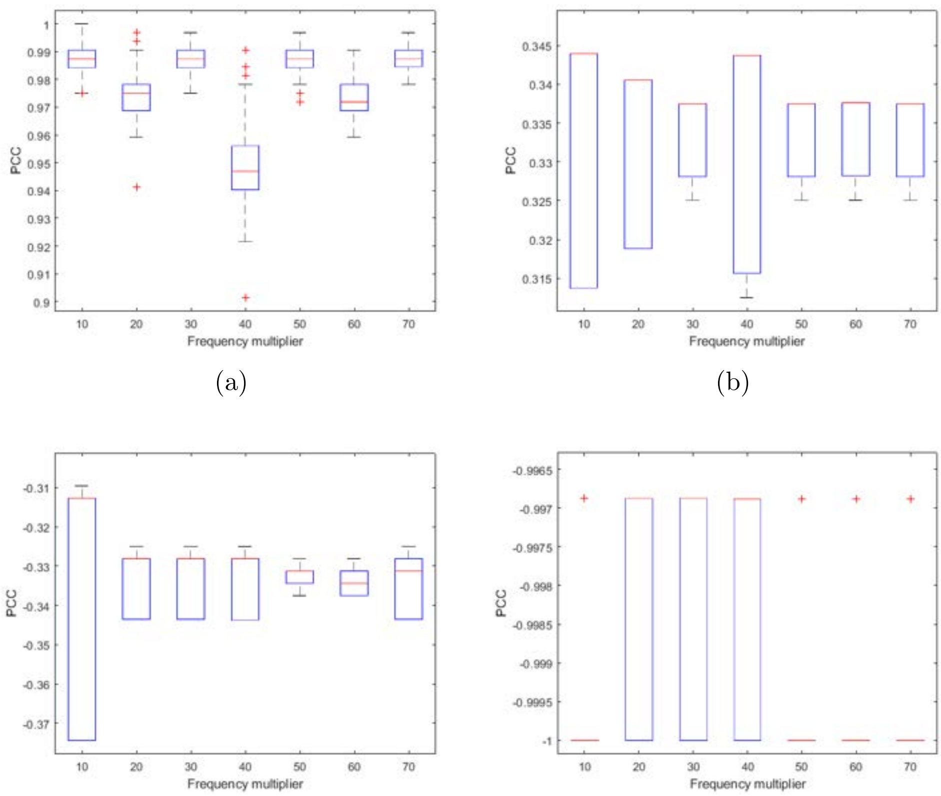

(a) (b)

(c) (d)

Figure V.36: Pearson correlation coefficient vs switching frequency in terms of the frequency multiplier. **(a):** $f_{SW} = \alpha f_{CAM}$ ($PCC > 0.7$); **(b):** $f_{SW} = (\alpha + 1/6) \cdot f_{CAM}$ ($0 < PCC < 0.65$); **(c):** $f_{SW} = (\alpha + 1/3) \cdot f_{CAM}$ ($-0.65 < PCC < 0$); **(d):** $f_{SW} = (\alpha + 1/2) \cdot f_{CAM}$ ($PCC < -0.7$)

Therefore, the real-world vertical distance value was assumed as $d_y = 0.595$ for all the calculations. A squared signal activated this lamp during transmission with a duty cycle of 50%. However, when the panel was in the waiting state, it receives a continuous power supply.

Figure V.37: Field experiment emitter

The optical power of the LED panel with different input values is shown in figure V.38. Based on these results, an input voltage of 10 V was selected. Consequently, the driver circuit for controlling the data transmission received a 10 V squared signal. The frequency of this signal changes depending on the symbol to be transmitted.

On the receiver side, a Raspi Camera Module V2 (see figure V.39) was selected.

Table V.21: Pearson Correlation Coefficient obtained values.

Frequency (Hz)	Maximum	Mean	Minimum
300	0.9969	0.9887	0.9781
305	0.3439	0.3338	0.3138
310	-0.3097	-0.3331	-0.3744
315	-0.9969	-0.9982	-1.0000
600	1.0000	0.9787	0.9500
605	0.3406	0.3334	0.3189
610	-0.3251	-0.3333	-0.3436
615	-0.9969	-0.9982	-1.0000
900	1.0000	0.9870	0.9719
905	0.3375	0.3334	0.3250
910	-0.3251	-0.3333	-0.3436
915	-0.9969	-0.9983	-1.0000
1200	0.9906	0.9571	0.9072
1205	0.3438	0.3333	0.3125
1210	-0.3250	-0.3333	-0.3437
1215	-0.9969	-0.9985	-1.0000
1500	1.0000	0.9860	0.9688
1505	0.3375	0.3334	0.3250
1510	-0.3281	-0.3333	-0.3375
1515	-0.9969	-0.9995	-1.0000
1800	0.9906	0.9738	0.9476
1805	0.3376	0.3334	0.3251
1810	-0.3282	-0.3333	-0.3375
1815	-0.9969	-0.9994	-1.0000
2100	1.0000	0.9885	0.9750
2105	0.3375	0.3334	0.3250
2110	-0.3251	-0.3333	-0.3336
2115	-0.9969	-0.9993	-1.0000

This camera was mounted on a Raspberry Pi B for managing its characteristics and controlling the video acquisition. During the experiments, the resolution was set to 1920×1080, while the frame rate was left as default (25 fps). For this combination the vertical FoV is partial with a value of $34.65°$ (0.6048 radianes) instead of $48.8°$, resulting in a camera's FoV, and resolution ratio of $\varphi_y = 5.5996 \cdot 10^{-4}$. Additionally, the camera has high contrast, low brightness, focus to infinity, and automatic white balance.

The camera was activated for recording videos of three minutes duration before the emitter started the data transmission. The resulting 4500 frames were stored in the Raspberry Pi memory card for off-line processing for each video.

Since the proposed modulation scheme requires at least two projected bands,

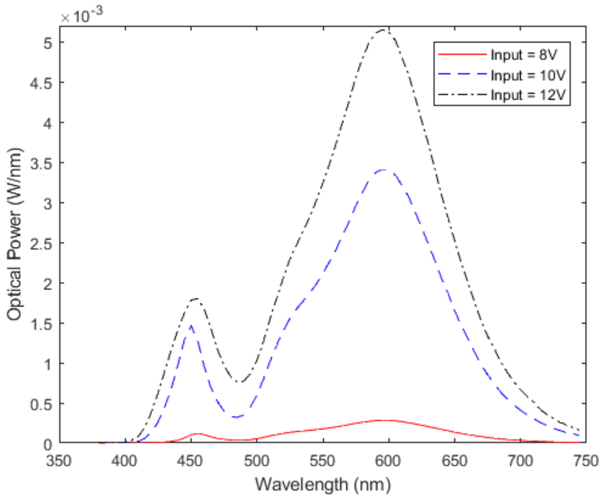

Figure V.38: Emitter's optical power.

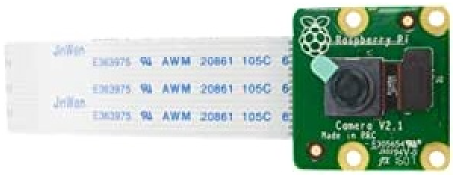

Figure V.39: Field experiment receiver.

υ was assumed to be 2 for the worst-case scenario for all the calculations. Additionally, the frequency multiplier was determined by applying equation IV.6, resulting in a maximum value of 108 for the applied resolution $N_y = 1080$. However, the minimum frequency multiplier depends on the projected source size, and therefore, on the distance D between the emitter and the receiver. Then, this experiment was divided into three trial sets:

1. Short range: D< 20 m

2. Medium range: 20 <D< 60 m

3. Long-range: D> 60 m

In all the trials, the distance between the emitter and the receiver changes. This separation started at 5 m, and the receiver was moved lineally 5 m at the time. Additionally, each symbol was repeated for three, four, and five consecutive frames.

For the short range case, the target distance was $D = 15$ m. For this separation, the selected light source ($d_y = 0.595$) is represented by approximately 72 vertical pixels (calculated using equation III.29 with β, and γ set to 90°). Therefore, the minimum frequency multiplier is calculated as follows:

$$\alpha > \frac{\upsilon \mathrm{FoV}_y}{4\left[\arctan\left(\frac{d_y}{2D}\right)\right]}$$

$$\alpha > \frac{2 * 0.6048}{4\left[\arctan\left(\frac{0.595}{2*15}\right)\right]}$$

$$\alpha > 14.99$$

This value was selected for the experimental implementation. The system's frequencies were determined with equation IV.10, while by applying equation IV.4 a strip's size of 36 pixels was calculated. The calculated frequencies are shown in equation V.10. For practical reasons, the frequencies were set to their approximations.

$$f_{\mathrm{SW}} = \begin{cases} 375.00 & \approx 375.0 \quad \mathrm{DATA} = 10 \\ 379.17 & \approx 379.0 \quad \mathrm{DATA} = 11 \\ 383.33 & \approx 383.5 \quad \mathrm{DATA} = 01 \\ 387.50 & \approx 387.5 \quad \mathrm{DATA} = 00 \end{cases} \tag{V.10}$$

In the medium range case, the target distance was $D = 30$ m. For this separation, the selected emitter ($d_y = 0.595$) has at least 36 vertical pixels (calculated using equation III.29 with β, and γ set to 90°). Then, the minimum frequency multiplier is calculated as follows:

$$\alpha > \frac{2 * 0.6048}{4\left[\arctan\left(\frac{0.595}{2*30}\right)\right]}$$

$$\alpha > 29.98$$

This value was selected for the experimental implementation. Based on the distance, and the frequency multiplier, the system's frequencies were determined using equation IV.10. In the same way, by applying equation IV.4 a strips' vertical width of 18 pixels was calculated. The calculated frequencies were:

$$f_{\mathrm{SW}} = \begin{cases} 750.00 & \approx 750.0 \quad \mathrm{DATA} = 10 \\ 754.17 & \approx 754.0 \quad \mathrm{DATA} = 11 \\ 758.33 & \approx 758.5 \quad \mathrm{DATA} = 01 \\ 762.50 & \approx 762.5 \quad \mathrm{DATA} = 00 \end{cases} \tag{V.11}$$

Finally, for the long range case, a distance $D = 70$ m was selected, and the lamp ($d_y = 0.595$) in the frames has 15 vertical pixels (calculated using equation

III.29 with β, and γ set to 90°). So the the minimum frequency multiplier is calculated as follows:

$$\alpha > \frac{2 * 0.6048}{4\left[\arctan\left(\frac{0.595}{2*70}\right)\right]}$$

$$\alpha > 71.14$$

The value of $\alpha = 75$ was selected for the frequency multiplier. Using equation IV.10 the system's frequencies were determined, while by applying equation IV.4 a strip's size of 7.2 pixels was calculated. The frequencies were:

$$f_{\text{SW}} = \begin{cases} 1875.00 & \approx 1875.0 \quad \text{DATA} = 10 \\ 1879.17 & \approx 1879.0 \quad \text{DATA} = 11 \\ 1883.33 & \approx 1883.5 \quad \text{DATA} = 01 \\ 1887.50 & \approx 1887.5 \quad \text{DATA} = 00 \end{cases} \tag{V.12}$$

At each location, before starting the transmission, a photo of the lamp turned on was taken. These frames were used to locate the light source for each distance D. For this purpose, at first, the image was manually masked around the lamp location for eliminating the great part of the background. Then the resulting frame was binarized using Otsu's thresholding technique. Therefore, the binary image was segmented to obtain the lamp's centroid. By applying equations III.28, and III.29 the pixel distance of the panel were calculated. With these data, the exact ROI containing only the emitter was obtained and cropping the video frames.

Afterward, the videos were processed using cropped frames. At first, the 2-D mean and standard deviation of the image were computed for performing the wake-up process described in chapter IV section IV.2. In this particular case, the symbol "10" was selected as the transmission head for determining if the transmission started before, during, or after acquiring the light source pixels. Once the system changed its status to transmitting, the images were grouped depending on the number of consecutive frames representing each symbol.

Finally, each group of m frames was put through the data extraction procedure described in figure IV.4. At firsts, a min-max normalization was applied for assuring the same pixel's intensity range in all the frames. Then the PCC was calculated for the corresponding consecutive frames. For example, in the case of $m = 3$, and a synchronized signal, two PCC values would be computed: $PCC(F_n, F_{n+1})$, and $PCC(F_{n+1}, F_{n+2})$. For the demodulation process, the average value of PCC was used. The obtained symbols were stored gradually in a vector.

When the system detected the transmission's end employing the wake-up process, the stored data vector was compared to the transmitted data. From this comparison, critical information was extracted: the BER of the communication, the failure transmission probability for each combination, and the successful transmission probability. The failure transmission probability is defined as the specific symbol error rate for each combination. It is the probability of receiving the symbol A given that the symbol B was transmitted. However, the successful transmission probability was defined as the inverse of the complete symbol error rate. In other words, it is the probability of receiving the symbol A given that symbol A was transmitted.

V.6.d Experimental results

As shown in figure V.40, for $\alpha = 15$ the transmission at the target distance D= 15 m was successful with BER of $5 \cdot 10^{-4}$ for 3 consecutive frames. The same happened at 20 m, where the lamp was represented by 53 vertical pixels (1.5 bands). However, at 25 m where the lamp was represented by 43 vertical pixels (1.2 bands) the BER increases to $2 \cdot 10^{-2}$ for 3 consecutive frames, but stays at $9 \cdot 10^{-4}$ for 4 consecutive frames. Additionally, in all the cases, the success probabilities are above 99.8% for distances below 20 m.

As shown in figure V.41, for $\alpha = 30$ the transmission at the target distance D= 30 m was successful with BER of $1.2 \cdot 10^{-3}$ for 3 consecutive frames, and $1.1 \cdot 10^{-3}$ for 4 consecutive frames. Then at 35 m, and 40 m, where each frame captured 1.5 light bands, the link increased its BER to $1.3 \cdot 10^{-3}$, and $1.8 \cdot 10^{-3}$ correspondingly for 3 consecutive frames. In the case of 4 consecutive frames, the BER value did not change. While the BER was less than $1 \cdot 10^{-4}$ for 5 consecutive frames. Moreover, at 45 m where the lamp was represented by 24 vertical pixels (1.3 bands) the BER reaches $4 \cdot 10^{-2}$ for 3 consecutive frames, but $2.9 \cdot 10^{-3}$ for 4 consecutive frames, and $1.5 \cdot 10^{-3}$ for 5 consecutive frames. Additionally, in all the cases, the succeed probabilities are above 99.6% for distances below 40 m.

Finally, as shown in figure V.42, for $\alpha = 75$ the transmission at the target distance D= 70 m, an up to 90 m, was successful with BER of $6 \cdot 10^{-4}$ for 3, and 4 consecutive frames. While at 95 m, where the lamp was represented by 11 vertical pixels (1.5 bands), the link has BER of $7 \cdot 10^{-4}$ for 3, and 4 consecutive frames. Moreover, at 100 m, the distance where each frame captured 1.4 light bands, the BER increases to $2 \cdot 10^{-3}$ for 3 consecutive frames, and up to $7 \cdot 10^{-4}$ for 4 consecutive frames. Additionally, in all the cases, the succeed probabilities are above 99.6% for distances below 100 m, and 99.8% for maximum 95 m.

Since the probability of decoding the symbols successfully is above 99.6% for the three distance ranges, the experiment demonstrated that the modulation scheme is functional, even when only 1.5 light bands are extracted from the frame. Additionally, the BER results for three consecutive frames are comparable to the outcomes presented in [93, 94], which are considered viable modulations schemes. Therefore, the proposed modulation has been validated. Since each transmitted symbol contains two bits, the throughput of the system is $f_{cam} * 2/3 = 16.67$ bps.

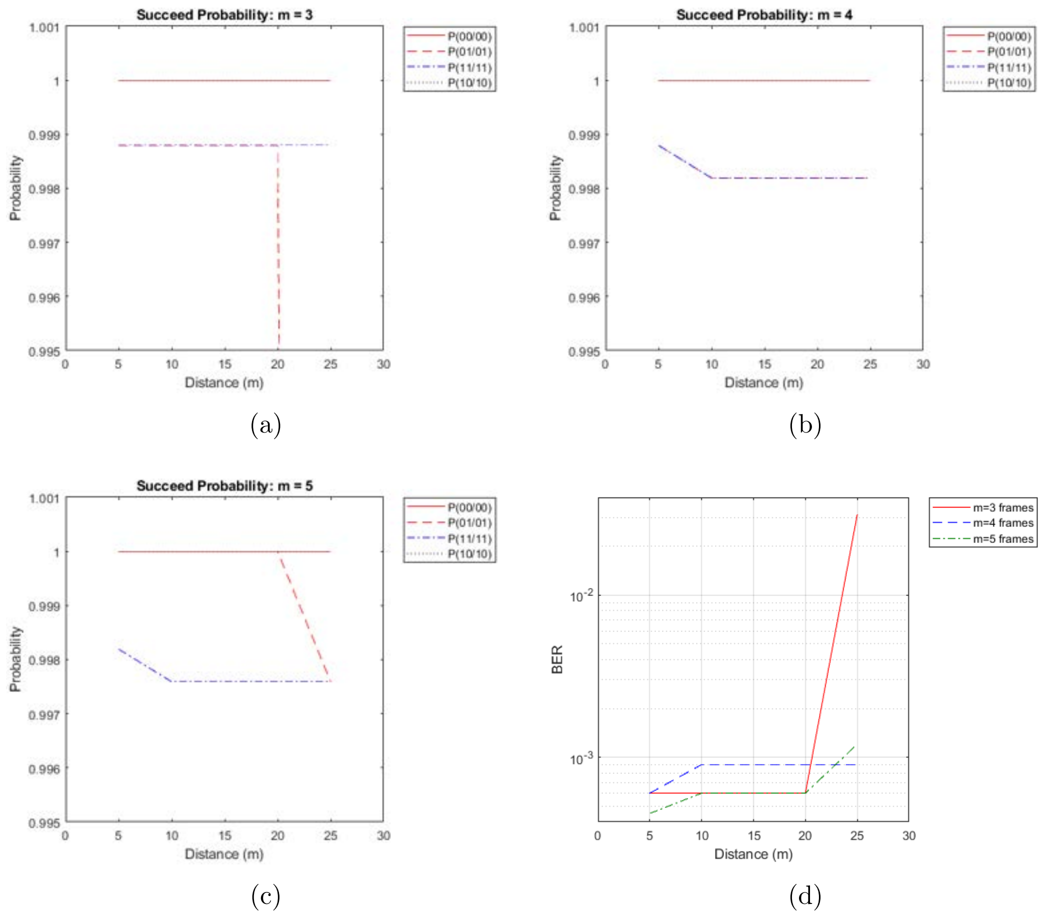

Figure V.40: Modulation scheme's results for $\alpha = 15$.**(a):** success probability for 3 consecutive frames; **(b):** success probability for 4 consecutive frames; **(c):** success probability for 5 consecutive frames; **(d):** bit error rate.

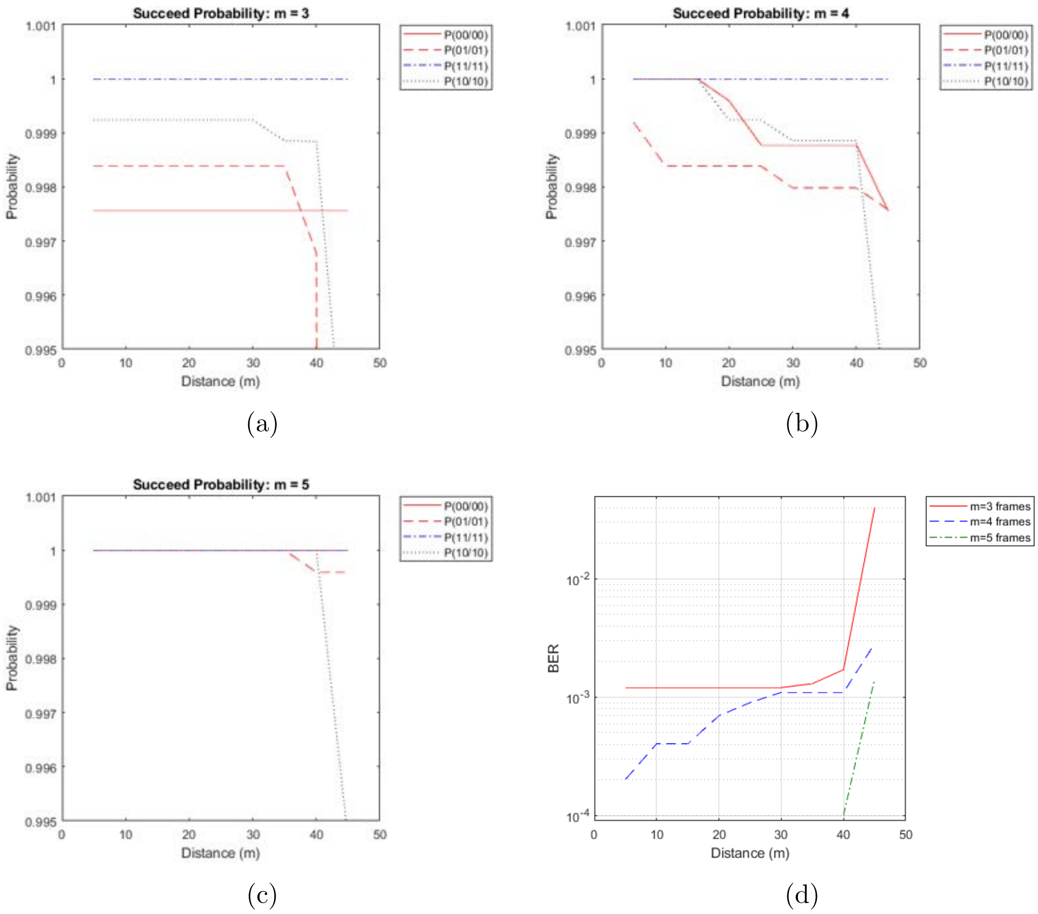

Figure V.41: Modulation scheme's results for $\alpha = 30$.**(a):** success probability for 3 consecutive frames; **(b):** success probability for 4 consecutive frames; **(c):** success probability for 5 consecutive frames; **(d):** bit error rate.

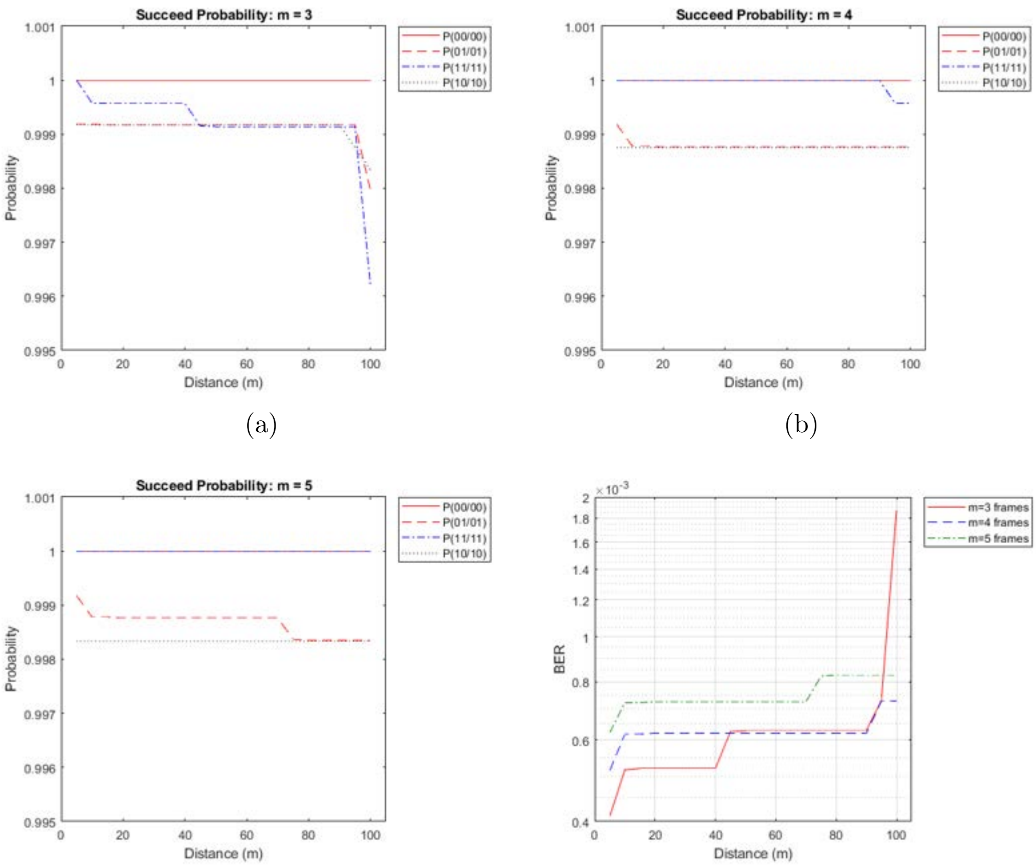

(a) (b) (c) (d)

Figure V.42: Modulation scheme's results for $\alpha = 75$.**(a):** success probability for 3 consecutive frames; **(b):** success probability for 4 consecutive frames; **(c):** success probability for 5 consecutive frames; **(d):** bit error rate.

Chapter VI

Conclusions and future research lines

This research work, "Optical Camera Communication for Internet of Things in Urban Environments," focused on the possibility of implementing IoT applications to start the deployment of smart cities, especially in developing countries by using OCC technology. For this purpose, some useful approximations related to the pixel's representation of objects on images and the impact of close light emitters over the communication performance were provided. These predictions were the base for designing possible OCC systems for real-world applications. Examples of those systems have been presented on [51, 52, 64, 107], while their corresponding simulations and experiments were provided in this work. Additionally, the proposed applications' implementation demonstrated the necessity of a novel flickering-free distance independent modulation scheme. This modulation technique was presented and validated through simulations and field experiments.

VI.1 Conclusions

During the analysis of OCC present, challenges, and trends in chapter II three main conclusions were extracted: the interference characterization of OCC systems should be focused on self-interference taking into account the chromatic nature of light; the demonstration of viable outdoor long-distance OCC systems is required for assuring the implementation of OCC-based IoT solutions in urban environments. Additionally, a flickering-free modulation scheme that can reach long distances with moderately complex algorithms should be based on comparing consecutive frames.

At first, the characterization of OCC systems are generally based on previous VLC studies and neglected the image formation perspective. There is a comprehensive survey in the field of the possible impact that solar radiation [22] and weather conditions, such as snowfall [13], rain [14] and fog [15], can produce over the transmitted signal. However, its direct effect on the obtained image has not been studied. All these works presented models based on photodiode receivers for predicting the degradation of the signal. Some studies related to the image distortion problem due to optical turbulence [18, 19], or lens aberration [20] did not consider the data transmission, only the image generation. For the characterization of OCC systems, both things are needed: data transmission and image generation. Nevertheless, the effect of distance over the projection of the emitters [16], the viewing-angle dependency over the SNR of the communication link [17, 23], and the self-interference as a performance degradation factor [17, 21, 22], have been studied assuming the use of cameras with a simplified frame acquisition scheme as receivers and a simple OOK data transmission. However, these works used complex 2-D representations, and the chromatic effect has not been discussed. Therefore a simple and efficient way of predicting the 2-D representation of the emitters is required along with the chromatic influence of close light transmitters. For these reasons, a simplified general equation for predicting the 2-D projections over an image was presented on chapter III and validated on chapter V, while the relation NPSIR, that take into account the signal's wavelength, was introduced on chapter III and its acquisition and usability validation were detailed on chapter V.

Secondly, nowadays different IoT applications based on OCC systems have been proposed. Typically these applications, such as positioning, tracking and navigation systems [43–50], motion captures, and WSN [61–63, 108] are designed for indoor purposes or short distances. Additionally, the proposed ITS implementations using OCC technology with mobile vehicles can work properly for short distances, under 2 m [57, 59, 60]; and for medium range links, under 50 m [54–56] with acceptable BER values. In the case of longer distances the communication presents errors, for example, the system proposed in [58], according to the simulations, can establish communication with 10^{-2} SER for a 75 m link with direct communication, and a 128 m link by using a relay vehicle. In this sense, a real outdoor long distance application for OCC systems is required for implementing IoT in urban environments. For these reasons, an indoor implementation that can be used for outdoor environments and a long distance outdoor application were tested as described on chapter V.

Finally, for long distance IoT applications based on OCC a distance-independent modulation scheme that employs low or moderate complexity algorithms is required. There are several low and moderate complexity modulation techniques based on OOK [63, 65–74], and based on CSK [23, 24, 75, 76] that have been proposed. These schemes work properly exclusively for short distances, within a 5 m range. Other polychromatic modulations [46, 77, 78] achieves long distances, within a 100 m range, but the system's complexity increases significantly. The modulations based on space-time coding [89, 91, 92] reach the longest distances, more than 100 m. However the implementation of those techniques requires specialized hardware and the overall system's complexity is very high complexity. The undersampled techniques [80, 81, 83–88] provides the fastest transmissions rates with moderate to high complexity, and medium range distances, less than 60 m. Finally, the modulation schemes based on the comparison of consecutive frames [93, 94] work properly for long distance range, more than 100 m, with moderate complexity. In summary, the distance-independent modulation scheme that the OCC-based IoT's implementation for urban environments requires should be based on the comparison of consecutive frames. Such modulation technique was presented and detailed on chapter IV, and validated on chapter V.

Similarly, from the outcomes of the experimental evaluation described in section V.1, a low complexity and efficient way of predicting the 2-D representation of the emitters was validated. In this sense the usability of equations III.28 and III.29, described on section III.6, for estimating the 2-D pixel representation of real-world distance was tested for scenarios where the emitters rotated over the vertical axis. During the experiments, the estimated pixels' distance and the distance obtained from the frames were compared. On average, the approximation has an error 0.5605 pixels, which is comparable with the results from more complex photography representation models. Due to the symmetry related to the frame's acquisition, these results can be extrapolated to the rotation over the horizontal axis. Therefore the proposed equations can accurately estimate the 2-D pixel projection (x, y) in a photograph of a real distance (d_x, d_y) in function of the separation between the object and the camera (D), the relative angle of the object (vertical β or horizontal γ), and the camera's specific characteristics. In this way, the first detailed objective of this thesis has been fulfilled. Additionally, this experiment demonstrated the importance of taking into account the minimum focus distance while taking photographs. For the samples that were taken at a position closer than the minimum focus distance ($D \leqslant 40$ cm), the error in the pixels' calculation increased up to 2.7547 pixels.

By analyzing the experiment described in section V.2, several conclusions related to the interference from close-emitters within an OCC system were obtained. Concerning the distance between the light sources, the interference can be neglected when the pixel separation between the sources' boundaries is above three pixels, indicating a perfect spatial separation. On the other hand, for separations around one pixel, the interference would significantly impact the communication link's performance; therefore, distances below one pixel are considered critical spatial separation. In relation to the wavelength used by the light sources, since the transmission of white light has components in the three optical channels of the frame (red, green, and blue), these emissions are significantly affected by any light source and also impact the performance of other emitters independently of the selected wavelength. In the same way, the interference from light sources emitting in the same wavelength is remarkable greater than the interference from emitters using different wavelengths at the same distance, affecting the data communication negatively. Additionally, the blue and red transmissions are appreciably more affected by green emitters than by red and blue senders, respectively. However, green transmissions are similarly impacted by emissions in blue and red. Summarizing, the close emitters within the same OCC system with transmissions in red and blue affect less the communication performance than other color combinations.

From the simulation's results and the calculated emitter's interference presented in section V.3 can be concluded that NPSIR values can be applied to directly estimate the worst-case scenario of the impact from relative close emitters over the communication's link performance. For this purpose, an equation that relates the number of pixels affected by the interference with the BER on the communication's link is required. Such equations depend on the selected modulation technique and codification, as shown in equation V.5 applied during the calculations. However, these estimations need the emitter's optical power's characterization and the camera's CFA and silicon responsivity. Therefore the equation for predicting the upper limit of the system's BER can be customized for different designs. Additionally, the separation between sources can be predicted using equations III.28 or III.29 independently of the distance between the emitters and the camera. In this way, the adequate NPSIR values can be applied for the calculations. Consequently, the usability of the introduced relation NPSIR for quantifying the impact of relative close emitters over the communication link in OCC systems was proved, fulfilling the second detailed objective.

As previously stated, the NPSIR provides an estimation of the maximum BER due to the interference of close emitters within OCC systems. Moreover, this interference can be added to other optical noise sources such as sunlight or environmental illumination by applying superposition. Therefore, the communication's performance of any designed OCC application can be tested before the implementation stage, and some specific preventive measures can be implemented for mitigating the interference of close emitters. In this way, by fulfilling the detailed objectives O1 and O2, the hypothesis 1 "OCC close-emitter interference can be characterized for indoor and outdoor implementations" has been validated.

The real-time two-step 3-D localization and tracking system based on OCC proposed on [51,52] was tested under lab conditions, as described on section V.4. During these experiments, four objects were accurately positioned and tracked simultaneously, proving the applicability of such a system in the emerging Industrial Internet of Things (IIoT) applications field for robots' navigation, as well as for any tracking execution where the objects to be located does not possess embedded cameras but own a LED-based device. Moreover, the proposed positioning and tracking system can be implemented for outdoor deployments by configuring the receiver specifically for acquiring dark photographs with high contrast; therefore, the light sources could be highlighted. Consequently, this system is a viable OCC-based application for IoT that can be employed for outdoor purposes and contributes to fulfilling this thesis's fourth detailed objective.

The outdoor WSN system based on OCC proposed on [64] was tested with a field experiment, as described on section V.5. A long-distance communication link, more than 300 m, between an old generation smart-phone and a LED-based advertising device was successfully established. In this particular implementation, the emitter was designed for drawing the attention of potential customers; therefore, its flickering was expected and desired. For this reason, the deployment was done by applying OOK modulation without undersampling. Nevertheless, for general IoT implementations within urban environments, a flickering-free modulation scheme for long distances is required. However, the field experiment demonstrated that this OCC-based WSN is viable for IoT basic implementations contributing to fulfilling the fourth detailed objective of this thesis.

In order to generalize the applicability of the proposed WSN, a flickering-free distance-independent modulation scheme was introduced in chapter IV. From the detailed analysis of its theoretical fundamentals, a procedure for selecting the appropriated switching frequencies based on the receiver's characteristics, the emitters' sizes, and the maximum distance of the system was developed. The validity of that strategy was proved through a set of simulations detailed in section V.6, while the communication's performance when applying the modulation technique was determined with some field experiments presented in the same section. The obtained BER and success rate for the implementation with the minimum amount of consecutive frames are comparable to the outcomes of the target modulation schemes proposed in [93, 94]. At the same time, the system's throughput ($f_{cam} * 2/3$ bps) is better without the necessity of calibration procedures or overhead because the proposed modulation method is based on the analysis of the consecutive frames PCC. Additionally, the simplicity of the wake-up process and the modulation method assures an overall minor complexity of the system, an improvement compared to other long-distance modulation techniques which presented significant or high complexity [77,78,84,91,92] for similar distance's ranges.

Moreover, the experimental results showed a practical 100 m link using a frequency multiplier α below the maximum value calculated for the camera's characteristics. When a greater α is used for the system, the switching frequencies increase, producing thinner light bands that require fewer pixels for fulfilling the one and a half stripes limitation required for proper demodulation and longer distances can be reached. In the case of the detailed field experiment, the maximum achievable distance is 134 m for the selected vertical resolution working with a switching frequency of 2700 Hz. Finally, the experimental results conclude that this modulation technique's constraint is the number of lighter and darker bands extracted from each frame. The communication's performance is directly proportional to this number. Therefore, the maximum value of α should be applied to the system independently of the target distance.

Since the simulations validated the procedure for selecting the appropriated switching frequencies, and the experiments showed a practical 100 m link while proving that the implementation performs similarly for the same amount of obtained light strips independently of the target distance, the developed flickering-free distance-independent modulation scheme for OCC based on the analysis of consecutive frames has been experimentally validated. In this way, the third detailed objective has been fulfilled, and the hypothesis 2 "OCC systems can be deployed for medium and long distances by using a distance-independent modulation scheme based on consecutive frames relations without the necessity of previous calibration." has been verified.

Finally, since the proposed flickering-free distance-independent modulation scheme is effective, it can be applied for implementations with a wide distance's ranges, like the practical OCC-based applications for IoT validated on sections V.4 and V.5. In this way, the industrial indoor positioning and tracking system proposed on [51,52] can be employed for outdoor purposes, and by eliminating the flickering problem, the outdoor WSN system presented on [64] can be employed for environmental pollution monitoring, temperature or humidity variation control, water contamination monitoring, or disasters' detection, among other smart cities useful applications. Therefore, some viable applications of OCC for IoT have been validated. In this way, the final hypothesis 3 of this research work, "OCC-based implementations are suitable for the deployment of IoT systems in urban environments," has been demonstrated.

VI.2 Future works

Further research in the design, development, and implementation of OCC systems for IoT applications in urban environments is needed. The NPSIR is a tool for quantifying the interference of close-emitters and can be used to mitigate its impact over an OCC system. However, the communication of long-distance links can be significantly affected by solar radiation interference, weather conditions (rain, snow, fog), the presence of suspended particles in the air (haze, pollution), or the temperature variation. Therefore these phenomenons should be considered and characterized for outdoor environments.

The proposed modulation technique mitigates the problem of light's condition instability during data transmission by working on the similarity of normalized images. However, more research on the impact of light conditions and the camera's exposure time is required. Besides, as stated previously, the degradation of the communication link related to the solar radiation interference, weather conditions (rain, snow, fog), the presence of suspended particles in the air (haze, pollution), and the temperature variation should be studied. Therefore lab and field experiments under extreme weather conditions should be performed.

The proposed modulation technique has been tested for white light. However, for increasing the data transmission rate, the three color channels should send information independently. Therefore, experiments using RGB LEDs, as long as a study related to the advantages and disadvantages of including color channels, is required. Additionally, for improving the throughput, the use of n-bit symbols should be considered. For implementing this change, the modulation should be based on 2^n switching frequencies that generate distinctive PCC values. Consequently, in the future, a detailed analysis of the use of more frequencies should be done. In the same way, the possibility of combining this modulation technique with multilevel codification and the implications of using not true square switching signals should be explored.

Moreover, the indoor and outdoor applications can be improved by adding several concurrent receivers with overlapping views ranges. In this way, the OCC-based systems could cover more significant extensions. For example, the proposed positioning technique could be used to locate and track objects moving within an entire factory. However, this addition is not trivial, especially with non-static elements. The research of possible hand-off processes between the cameras is required.

Finally, for speeding up the image processing phase in a OCC system, the extraction of accurate ROI with minimal additional computational time is required. For the majority of the applications, the cropped section should contain almost exclusively the light source. To achieve this goal, a simple automatic location system and an efficient segmentation algorithm should be developed.

Bibliography

[1] "IEEE standard for local and metropolitan area networks–part 15.7: Short-range wireless optical communication using visible light," Sept 2011.

[2] R. Heile, *Short-range wireless optical communication. Revision to IEEE Standard 802.15.7-2011*. IEEE, heile ed., March 2014.

[3] W. Huang, P. Tian, and Z. Xu, "Design and implementation of a real-time CIM-MIMO optical camera communication system," *Opt. Express*, vol. 24, pp. 24567–24579, Oct 2016.

[4] N. Saha, M. S. Ifthekhar, N. T. Le, and Y. M. Jang, "Survey on optical camera communications: challenges and opportunities," *IET Optoelectronics*, vol. 9, pp. 172–183, oct 2015.

[5] F. J. Lopez-Hernandez, R. Perez-Jimenez, and A. Santamaria, "Ray-tracing algorithms for fast calculation of the channel impulse response on diffuse IR wireless indoor channels," *Optical Engineering*, vol. 39, p. 2775, oct 2000.

[6] C. Quintana, J. Rabadan, J. Rufo, F. Delgado, and R. Perez-Jimenez, "Time-hopping spread-spectrum system for wireless optical communications," *IEEE Transactions on Consumer Electronics*, vol. 55, pp. 1083–1088, aug 2009.

[7] J. Rufo, J. Rabadan, F. Delgado, C. Quintana, and R. Perez-Jimenez, "Experimental evaluation of video transmission through LED illumination devices," *IEEE Transactions on Consumer Electronics*, vol. 56, pp. 1411–1416, aug 2010.

[8] C. Quintana, V. Guerra, J. Rufo, J. Rabadan, and R. Perez-Jimenez, "Reading lamp-based visible light communication system for in-flight entertainment," *IEEE Transactions on Consumer Electronics*, vol. 59, pp. 31–37, feb 2013.

[9] J. Luna-Rivera, R. Perez-Jimenez, J. Rabadan-Borjes, J. Rufo-Torres, V. Guerra, and C. Suarez-Rodriguez, "Multiuser CSK scheme for indoor visible light communications," *Optics Express*, vol. 22, p. 24256, sep 2014.

[10] J. Rabadan, V. Guerra, R. Rodríguez, J. Rufo, M. Luna-Rivera, and R. Perez-Jimenez, "Hybrid visible light and ultrasound-based sensor for distance estimation," *Sensors*, vol. 17, p. 330, feb 2017.

[11] S. N. de Planificacion y Desarrollo (SENPLADES) de la Republica del Ecuador, "Plan Nacional de Desarrollo 2017 - 2021: Toda una Vida," Sept. 2017.

[12] N. Saeed, S. Guo, K.-H. Park, T. Y. Al-Naffouri, and M.-S. Alouini, "Optical camera communications: Survey, use cases, challenges, and future trends," *Physical Communication*, vol. 37, p. 100900, dec 2019.

[13] M. Akiba, K. Ogawa, K. Wakamori, K. Kodate, and S. Ito, "Measurement and simulation of the effect of snowfall on Free-Space Optical propagation," *Appl. Opt.*, vol. 47, pp. 5736–5743, Nov 2008.

[14] N. Araki and H. Yashima, "A Channel Model of Optical Wireless Communications during Rainfall," in *2005 2nd International Symposium on Wireless Communication Systems*, pp. 205–209, Institute of Electrical and Electronics Engineers (IEEE), Sept 2005.

[15] M. A. Naboulsi, "Fog attenuation prediction for optical and infrared waves," *Optical Engineering*, vol. 43, pp. 319–329, feb 2004.

[16] A. Ashok, M. Gruteser, N. Mandayam, J. Silva, M. Varga, and K. Dana, "Challenge: Mobile Optical Networks Through Visual MIMO," in *Proceedings of the Sixteenth Annual International Conference on Mobile Computing and Networking*, MobiCom '10, (New York, NY, USA), pp. 105–112, ACM, Sept. 2010.

[17] A. Ashok, M. Gruteser, N. Mandayam, and K. Dana, "Characterizing multiplexing and diversity in visual mimo," in *2011 45th Annual Conference on Information Sciences and Systems*, pp. 1–6, Institute of Electrical and Electronics Engineers (IEEE), March 2011.

[18] L. J. November, "Measurement of geometric distortion in a turbulent atmosphere," *Appl. Opt.*, vol. 25, pp. 392–397, Feb 1986.

[19] M. Roggemann, B. Welsh, and B. Hunt, *Imaging Through Turbulence*. Laser & Optical Science & Technology, Taylor & Francis, 1996.

[20] M. Rebiai, S. Mansouri, F. Pinson, and B. Tichit, "Image distortion from zoom lenses: modeling and digital correction," in *1992 IBC International Broadcasting Convention*, pp. 438–441, Jul 1992.

[21] S. Pergoloni, M. Biagi, S. Colonnese, R. Cusani, and G. Scarano, "A space-time rls algorithm for adaptive equalization: The camera communication case," *Journal of Lightwave Technology*, vol. 35, pp. 1811–1820, May 2017.

[22] K. Cui, G. Chen, Z. Xu, and R. D. Roberts, "Traffic light to vehicle Visible Light Communication channel characterization," *Appl. Opt.*, vol. 51, pp. 6594–6605, Sep 2012.

[23] T. Nguyen, N. T. Le, and Y. M. Jang, "Practical design of Screen-to-Camera based Optical Camera Communication," in *2015 International Conference on Information Networking (ICOIN)*, pp. 369–374, Jan 2015.

[24] T. Nguyen, N. T. Le, and Y. M. Jang, "Asynchronous Scheme for Optical Camera Communication-based Infrastructure-to-vehicle Communication," *Int. J. Distrib. Sen. Netw.*, vol. 11, p. 908139, Jan. 2015.

[25] Y. Hong and L. Chen, "On the Performance of Mobile Visible Light Communications," *CoRR*, vol. abs/1605.01848, 2016.

[26] P. Misra and P. Enge, "Global positioning system: signals, measurements, and performance," *USA: Ganga - JamunaPress*, 2006.

[27] B. Li, J. Salter, A. G. Dempster, and C. Rizos, "Indoor positioning techniques based on wireless lan," in *First IEEE International Conference on Wireless Broadband and Ultra Wideband Communications*, (Sydney, Australia), pp. 13–16, IEEE, Mar. 2006.

[28] M. Bouet and A. L. dos Santos, "RFID tags: Positioning principles and localization techniques," in *2008 1st IFIP Wireless Days*, pp. 1 –5, IEEE, nov. 2008.

[29] M. F. Keskin, A. D. Sezer, and S. Gezici, "Localization via visible light systems," *Proceedings of the IEEE*, vol. 106, pp. 1063–1088, June 2018.

[30] G. Kail, P. Maechler, N. Preyss, and A. Burg, "Robust asynchronous indoor localization using led lighting," in *2014 IEEE International Conference on Acoustics, Speech and Signal Processing (ICASSP)*, pp. 1866–1870, IEEE, May 2014.

[31] H. Steendam, T. Q. Wang, and J. Armstrong, "Cramer-rao bound for indoor visible light positioning using an aperture-based angular-diversity receiver," in *2016 IEEE International Conference on Communications (ICC)*, pp. 1–6, May 2016.

[32] I. Marin-Garcia, P. Chavez-Burbano, A. Munoz-Arcentles, V. Calero-Bravo, and R. Perez-Jimenez, "Indoor location technique based on visible light communications and ultrasound emitters," in *2015 IEEE International Conference on Consumer Electronics (ICCE)*, pp. 297–298, Institute of Electrical and Electronics Engineers (IEEE), Jan 2015.

[33] E. Torres-Zapata, J. M. Luna-Rivera, R. Perez-Jimenez, V. Guerra, J. Rabadan, J. Rufo, and C. A. Gutierrez, "Implementation of a VLC-based indoor localization system," *Transactions on Emerging Telecommunications Technologies*, p. e3498, aug 2018.

[34] T.-H. Do and M. Yoo, "An in-depth survey of visible light communication based positioning systems," *Sensors*, vol. 16, p. 678, may 2016.

[35] M. T. Taylor and S. Hranilovic, "Angular diversity approach to indoor positioning using visible light," in *2013 IEEE Globecom Workshops (GC Wkshps)*, pp. 1093–1098, Dec 2013.

[36] S. H. Yang, D. R. Kim, H. S. Kim, Y. H. Son, and S. K. Han, "Indoor positioning system based on visible light using location code," in *2012 Fourth International Conference on Communications and Electronics (ICCE)*, pp. 360–363, Aug 2012.

[37] S.-H. Yang, D.-R. Kim, H.-S. Kim, Y.-H. Son, and S.-K. Han, "Visible light based high accuracy indoor localization using the extinction ratio distributions of light signals," *Microwave and Optical Technology Letters*, vol. 55, no. 6, pp. 1385–1389, 2013.

[38] T. Q. Wang, Y. A. Sekercioglu, A. Neild, and J. Armstrong, "Position accuracy of time-of-arrival based ranging using visible light with application in indoor localization systems," *Journal of Lightwave Technology*, vol. 31, pp. 3302–3308, Oct 2013.

[39] P. Luo, M. Zhang, X. Zhang, G. Cai, D. Han, and Q. Li, "An indoor visible light communication positioning system using dual-tone multi-frequency technique," in *2013 2nd International Workshop on Optical Wireless Communications (IWOW)*, pp. 25–29, Oct 2013.

[40] P. Luo, Z. Ghassemlooy, H. L. Minh, A. Khalighi, X. Zhang, M. Zhang, and C. Yu, "Experimental demonstration of an indoor visible light communication positioning system using dual-tone multi-frequency technique," in *2014 3rd International Workshop in Optical Wireless Communications (IWOW)*, pp. 55–59, IEEE, Sept 2014.

[41] M. Biagi, S. Pergoloni, and A. M. Vegni, "Last: A framework to localize, access, schedule, and transmit in indoor vlc systems," *Journal of Lightwave Technology*, vol. 33, pp. 1872–1887, may 2015.

[42] D. Zheng, G. Chen, and J. A. Farrell, "Navigation using linear photo detector arrays," in *2013 IEEE International Conference on Control Applications (CCA)*, pp. 533–538, Aug 2013.

[43] "Indoor location measuring device and method," Jan. 19 2012. WO Patent App. PCT/KR2010/005,779.

[44] Y.-S. Kuo, P. Pannuto, K.-J. Hsiao, and P. Dutta, "Luxapose: Indoor positioning with mobile phones and visible light," in *Proceedings of the 20th Annual International Conference on Mobile Computing and Networking*, MobiCom '14, (New York, NY, USA), pp. 447–458, ACM, 2014.

[45] M. S. Ifthekhar, N. Saha, and Y. M. Jang, "Neural network based indoor positioning technique in optical camera communication system," in

2014 International Conference on Indoor Positioning and Indoor Navigation (IPIN), pp. 431–435, IEEE, Oct 2014.

[46] Z. Yang, Z. Wang, J. Zhang, C. Huang, and Q. Zhang, "Wearables can afford: Light-weight indoor positioning with visible light," in *Proceedings of the 13th Annual International Conference on Mobile Systems, Applications, and Services*, MobiSys '15, (New York, NY, USA), pp. 317–330, ACM, may 2015.

[47] P. Huynh and M. Yoo, "VLC-based positioning system for an indoor environment using an image sensor and an accelerometer sensor," *Sensors*, vol. 16, p. 783, may 2016.

[48] R. Zhang, W.-D. Zhong, D. Wu, and K. Qian, "A novel sensor fusion based indoor visible light positioning system," in *2016 IEEE Globecom Workshops (GC Wkshps)*, pp. 1–6, IEEE, Dec 2016.

[49] B. Lin, Z. Ghassemlooy, C. Lin, X. Tang, Y. Li, and S. Zhang, "An indoor visible light positioning system based on optical camera communications," *IEEE Photonics Technology Letters*, vol. 29, pp. 579–582, April 2017.

[50] C. Lin, B. Lin, X. Tang, Z. Zhou, H. Zhang, S. Chaudhary, and Z. Ghassemlooy, "An indoor visible light positioning system using artificial neural network," in *2018 Asia Communications and Photonics Conference (ACP)*, pp. 1–3, IEEE, Oct. 2018.

[51] P. Chavez-Burbano, V. Guerra, J. Rabadan, C. Jurado-Verdu, and R. Perez-Jimenez, "Novel indoor localization system using optical camera communication," in *2018 11th International Symposium on Communication Systems, Networks Digital Signal Processing (CSNDSP)*, pp. 1–5, IEEE, July 2018.

[52] P. Chavez-Burbano, V. Guerra, J. Rabadan, and R. Perez-Jimenez, "Optical camera communication system for three-dimensional indoor localization," *Optik*, vol. 192, p. 162870, 2019.

[53] I. Takai, S. Ito, K. Yasutomi, K. Kagawa, M. Andoh, and S. Kawahito, "Led and cmos image sensor based optical wireless communication system for automotive applications," *IEEE Photonics Journal*, vol. 5, pp. 6801418–6801418, Oct 2013.

[54] T. Yamazato, I. Takai, H. Okada, T. Fujii, T. Yendo, S. Arai, M. Andoh, T. Harada, K. Yasutomi, K. Kagawa, and S. Kawahito, "Image-sensor-based visible light communication for automotive applications," *IEEE Communications Magazine*, vol. 52, pp. 88–97, jul 2014.

[55] T. Yamazato, A. Ohmura, H. Okada, T. Fujii, T. Yendo, S. Arai, and K. Kamakura, "Range estimation scheme for integrated i2v-VLC using a

high-speed image sensor," in *2016 IEEE International Conference on Communications Workshops (ICC)*, IEEE, may 2016.

[56] T. Yamazato, "V2X communications with an image sensor," *Journal of Communications and Information Networks*, vol. 2, pp. 65–74, dec 2017.

[57] I. Takai, T. Harada, M. Andoh, K. Yasutomi, K. Kagawa, and S. Kawahito, "Optical Vehicle-to-Vehicle Communication System Using LED Transmitter and Camera Receiver," *IEEE Photonics Journal*, vol. 6, no. 5, pp. 1–14, 2014.

[58] J.-E. Kim, J.-W. Kim, Y. Park, and K.-D. Kim, "Applicability of color-independent visual-mimo for v2x communication," in *2015 Seventh International Conference on Ubiquitous and Future Networks*, pp. 898–901, IEEE, July 2015.

[59] S. Teli, W. A. Cahyadi, and Y. H. Chung, "High-speed optical camera v2v communications using selective capture," *Photonic Network Communications*, vol. 36, pp. 210–216, Oct 2018.

[60] S. Teli and Y.-H. Chung, "Selective capture based high-speed optical vehicular signaling system," *Signal Processing: Image Communication*, vol. 68, pp. 241–248, oct 2018.

[61] N. Kumar, "Smart and intelligent energy efficient public illumination system with ubiquitous communication for smart city," in *Smart Structures and Systems (ICSSS), 2013 IEEE International Conference on*, pp. 152–157, March 2013.

[62] J.-E. Kim, J.-W. Kim, Y. Park, and K.-D. Kim, "Color-Space-Based Visual-MIMO for V2X Communication," *Sensors*, vol. 16, p. 591, apr 2016.

[63] W.-C. Wang, C.-W. Chow, L.-Y. Wei, Y. Liu, and C.-H. Yeh, "Long distance non-line-of-sight (nlos) visible light signal detection based on rolling-shutter-patterning of mobile-phone camera," *Opt. Express*, vol. 25, pp. 10103–10108, May 2017.

[64] P. Chavez-Burbano, V. Guerra, J. Rabadan, and R. Perez-Jimenez, "Optical Camera Communication for Smart Cities," in *2017 IEEE/CIC International Conference on Communications in China (ICCC Workshops)*, pp. 1–4, Oct 2017.

[65] N. Izuka, *OCC proposal of scope of standarization and applications: IEEE Std 802.15 SG7*. IEEE, izuka, n. ed., March 2014.

[66] T. Nguyen, N. T. Le, and Y. M. Jang, "Asynchronous scheme for unidirectional optical camera communications (occ)," in *2014 Sixth International Conference on Ubiquitous and Future Networks (ICUFN)*, pp. 48–51, IEEE, July 2014.

[67] T. Nguyen, C. H. Hong, N. T. Le, and Y. M. Jang, "High-speed asynchronous optical camera communication using led and rolling shutter camera," in *2015 Seventh International Conference on Ubiquitous and Future Networks*, pp. 214–219, July 2015.

[68] C. Danakis, M. Afgani, G. Povey, I. Underwood, and H. Haas, "Using a CMOS Camera Sensor for Visible Light Communication," in *2012 IEEE Globecom Workshops*, pp. 1244–1248, Dec 2012.

[69] N. Rajagopal, P. Lazik, and A. Rowe, "Visual light landmarks for mobile devices," in *Proceedings of the 13th International Symposium on Information Processing in Sensor Networks*, IPSN '14, (Piscataway, NJ, USA), pp. 249–260, IEEE Press, Apr. 2014.

[70] N. Rajagopal, P. Lazik, and A. Rowe, "Hybrid visible light communication for cameras and low-power embedded devices," in *Proceedings of the 1st ACM MobiCom Workshop on Visible Light Communication Systems*, VLCS '14, (New York, NY, USA), pp. 33–38, ACM, sept. 2014.

[71] H.-Y. Lee, H.-M. Lin, Y.-L. Wei, H.-I. Wu, H.-M. Tsai, and K. C.-J. Lin, "RollingLight: Enabling Line-of-Sight Light-to-Camera Communications," in *Proceedings of the 13th Annual International Conference on Mobile Systems, Applications, and Services*, MobiSys '15, (New York, NY, USA), pp. 167–180, ACM, May 2015.

[72] C.-W. Chow, C.-Y. Chen, and S.-H. Chen, "Visible light communication using mobile-phone camera with data rate higher than frame rate," *Opt. Express*, vol. 23, pp. 26080–26085, Oct 2015.

[73] K. Liang, C.-W. Chow, and Y. Liu, "Rgb visible light communication using mobile-phone camera and multi-input multi-output," *Opt. Express*, vol. 24, pp. 9383–9388, May 2016.

[74] Z. Li, Z. Zhang, Q. Yuan, Y. Qiao, K. Liao, and H. Yu, "Digital image processing in led visible light communications using mobile phone camera," in *2016 IEEE International Conference on Network Infrastructure and Digital Content (IC-NIDC)*, pp. 239–243, IEEE, Sept 2016.

[75] S.-H. Chen and C.-W. Chow, "Color-Shift Keying and Code-Division Multiple-Access Transmission for RGB-LED Visible Light Communications Using Mobile Phone Camera," *IEEE Photonics Journal*, vol. 6, pp. 1–6, Dec 2014.

[76] P. Hu, P. H. Pathak, X. Feng, H. Fu, and P. Mohapatra, "Colorbars: Increasing Data Rate of LED-to-camera Communication Using Color Shift Keying," in *Proceedings of the 11th ACM Conference on Emerging Networking Experiments and Technologies - CoNEXT15*, pp. 1–12, ACM, ACM, Dec. 2015.

[77] P. Das, B.-Y. Kim, Y. Park, and K.-D. Kim, "A new color space based constellation diagram and modulation scheme for color independent vlc," *Advances in Electrical and Computer Engineering*, vol. 12, pp. 11–18, Nov. 2012.

[78] P. Das, B.-Y. Kim, Y. Park, and K.-D. Kim, "Color-independent vlc based on a color space without sending target color information," *Optics Communications*, vol. 286, pp. 69 – 73, jan 2013.

[79] H.-W. Chen, S.-S. Wen, X.-L. Wang, M.-Z. Liang, M.-Y. Li, Q.-C. Li, and Y. Liu, "Color-Shift Keying for Optical Camera Communication Using a Rolling Shutter Mode," *IEEE Photonics Journal*, vol. 11, pp. 1–8, apr 2019.

[80] R. D. Roberts, "Undersampled Frequency Shift ON-OFF keying (UFSOOK) for camera communications (CamCom)," in *2013 22nd Wireless and Optical Communication Conference*, pp. 645–648, May 2013.

[81] N. T. Le, T. Nguyen, and Y. M. Jang, "Frequency shift on-off keying for optical camera communication," in *2014 Sixth International Conference on Ubiquitous and Future Networks (ICUFN)*, pp. 22–25, July 2014.

[82] Z. Ghassemlooy, P. Luo, and S. Zvanovec, *Optical Camera Communications*, pp. 547–568. Cham: Springer International Publishing, 2016.

[83] P. Luo, Z. Ghassemlooy, H. L. Minh, X. Tang, and H. M. Tsai, "Undersampled phase shift on-off keying for camera communication," in *2014 Sixth International Conference on Wireless Communications and Signal Processing (WCSP)*, pp. 1–6, Oct 2014.

[84] P. Luo, Z. Ghassemlooy, H. L. Minh, H. M. Tsai, and X. Tang, "Undersampled-PAM with subcarrier modulation for camera communications," in *2015 Opto-Electronics and Communications Conference (OECC)*, pp. 1–3, June 2015.

[85] P. Luo, M. Zhang, Z. Ghassemlooy, H. L. Minh, H.-M. Tsai, X. Tang, L. C. Png, and D. Han, "Experimental Demonstration of RGB LED-Based Optical Camera Communications," *IEEE Photonics Journal*, vol. 7, pp. 1–12, Oct 2015.

[86] P. Luo, M. Zhang, Z. Ghassemlooy, H. L. Minh, H.-M. Tsai, X. Tang, and D. Han, "Experimental demonstration of a 1024-qam optical camera communication system," *IEEE Photonics Technology Letters*, vol. 28, pp. 139–142, Jan 2016.

[87] N. Liu, J. Cheng, and J. F. Holzman, "Undersampled differential phase shift on-off keying for optical camera communications with phase error detection," in *13th International Wireless Communications and Mobile Computing Conference (IWCMC)*, pp. 916–921, June 2017.

[88] P. Luo, T. Jiang, P. A. Haigh, Z. Ghassemlooy, and S. Zvanovec, "Undersampled pulse width modulation for optical camera communications," in *2018 IEEE International Conference on Communications Workshops (ICC Workshops)*, pp. 1–6, IEEE, may 2018.

[89] Y. Amano, K. Kamakura, and T. Yamazato, "Alamouti-type coding for visible light communication based on direct detection using image sensor," in *2013 IEEE Global Communications Conference (GLOBECOM)*, pp. 2430–2435, Institute of Electrical and Electronics Engineers (IEEE), Dec 2013.

[90] M. Simon and V. Vilnrotter, "Alamouti-type space-time coding for free-space optical communication with direct detection," *IEEE Transactions on Wireless Communications*, vol. 4, pp. 35–39, jan 2005.

[91] K. Ebihara, K. Kamakura, and T. Yamazato, "Layered transmission of space-time coded signals for image-sensor-based visible light communications.," *Journal of Lightwave Technology*, vol. 33, pp. 4193 – 4206, oct 2015.

[92] K. Masuda, K. Kamakura, and T. Yamazato, "Spatial modulation in layered space-time coding for image-sensor-based Visible Light Communication," in *2016 IEEE 27th Annual International Symposium on Personal, Indoor, and Mobile Radio Communications (PIMRC)*, pp. 1–6, Institute of Electrical and Electronics Engineers (IEEE), Sept 2016.

[93] C.-W. Chow, R.-J. Shiu, Y.-C. Liu, Y. Liu, and C.-H. Yeh, "Non-flickering 100 m RGB visible light communication transmission based on a CMOS image sensor," *Opt. Express*, vol. 26, pp. 7079–7084, Mar 2018.

[94] M. A. Atta and A. Bermak, "A 160 m visible light communication link using hybrid undersampled phase-frequency shift on-off keying and CMOS image sensor," *Opt. Express*, vol. 27, pp. 2478–2487, jan 2019.

[95] N. B. Hassan, Z. Ghassemlooy, S. Zvanovec, M. Biagi, A. M. Vegni, M. Zhang, and P. Luo, "Non-line-of-sight MIMO space-time division multiplexing visible light optical camera communications," *Journal of Lightwave Technology*, vol. 37, pp. 2409–2417, may 2019.

[96] T. Nguyen, M. D. Thieu, and Y. M. Jang, "2d-OFDM for optical camera communication: Principle and implementation," *IEEE Access*, vol. 7, pp. 29405–29424, 2019.

[97] M. Langford, *Basic Photography.* Focal Press, 2000.

[98] Y. Ohno, "Color quality of white LEDs," in *Topics in Applied Physics*, pp. 349–371, Springer Netherlands, 2013.

[99] J. R. Martín, "Curso de Fotografía Digital," 2008.

[100] M. Freeman, *The Photographer's Handbook*. Octopus Publishing Group, 2017.

[101] M. Wolf, *Smart Camera Design*. Springer-Verlag GmbH, 2017.

[102] D. Menon and G. Calvagno, "Color image demosaicking: An overview," *Signal Processing: Image Communication*, vol. 26, pp. 518 – 533, oct 2011.

[103] N. Otsu, "A Threshold Selection Method from Gray-Level Histograms," *IEEE Transactions on Systems, Man, and Cybernetics*, vol. 9, pp. 62–66, Jan 1979.

[104] "Logitech hd pro webcam c920.." online, Oct. 2016.

[105] Rubinstein, *Simulation and the Monte Carlo Method*. John Wiley & Sons, 2016.

[106] A. B. Carlson and P. B. Crilly, *Communication Systems: An introduction to Signals and Noise in Electrical Communication*. McGraw-Hill Higher Education, 5 ed., 2010.

[107] P. Chavez-Burbano, V. Guerra, J. Rabadan, D. Rodríguez-Esparragón, and R. Perez-Jimenez, "Experimental Characterization of Close-Emitter Interference in an Optical Camera Communication System," *Sensors*, vol. 17, p. 1561, jul 2017.

[108] D. R. Dhatchayeny, W. A. Cahyadi, S. R. Teli, and Y. Chung, "A novel optical body area network for transmission of multiple patient vital signs," in *2017 Ninth International Conference on Ubiquitous and Future Networks (ICUFN)*, pp. 542–544, July 2017.

List of Abbreviations

2-D	two dimensions. 3, 4, 8, 26, 28, 45–49, 56–59, 102, 108, 109
3-D	three dimensions. 84, 89, 90, 110
ADC	Analog-to-Digital Converter. 32, 50
ANN	Artificial Neural Network. 13
AOA	Angle of Arrival. 12
BER	Bit Error Rate. xxiii–xxvii, 5–8, 13, 16, 18, 20–23, 51, 67, 68, 74, 79, 82, 94, 96, 103, 108, 110, 111, 125, 131, *Glossary:* BER
CCD	Charge Coupled Device. 28, 30, 125, 131, *Glossary:* Charge Coupled Device
CDMA	Code Division Multiple Access. 16
CFA	Color Filter Array. xxiv, 29, 32, 50, 76, 110, 131
CMOS	Complementary Metal Oxide Semiconductor. 15, 28, 31, 125, 127, 131, 132, *Glossary:* CMOS
COTS	Commercial off-the-shelf. 4
CSK	Color Shift Modulation. xxi, 16–18, 24, 108
DSLR	digital single-lens reflext. 29, 32, 131
ESPOL	Escuela Superior Politécnica del Litoral. 4
FDMA	Frequency Division Multiple Access. 15
FEC	Forward Error Correction. 21
FoV	Field of View. xxvi, 32, 35, 43, 45–49, 62, 71, 80, 86, 93, 96, 99, 129
fps	frames per second. 34
FSK	Frequency Shift Keying. 15, 22
GCM	Generalized Color Modulation. 17

GPS	Global Positioning System. 11, 126, 131, *Glossary:* GPS
ICI	Inter-channel Interference. 16
IDeTIC	Instituto para el Desarrollo Tecnológico y la Innovación en Comunicaciones. 4
IIoT	Industrial Internet of Things. xxvi, 110
IoT	Internet of Things. xxiii, xxvii, 1, 3–9, 11, 24, 35, 43, 64, 65, 67, 83, 91, 94, 107–112, 132
IPS	Indoor Positioning System. 3, 5, 11
ISO	International Organization for Standardization. 33
ITS	Intelligent Transportation Systems. xix, 1, 5, 11, 13, 21, 27, 108
LED	Light Emitting Diode. xix, xx, xxiii, xxiv, xxvi, xxvii, 2, 4, 10, 12–15, 18, 20–22, 25–27, 57, 68–71, 74, 76, 78, 80, 85, 88, 91–93, 96–98, 110, 112, 132
LoS	Line of Sight. 15, 16, 23, 51, 93, 126
MIMO	Multiple-Input Multiple-Output. xx, 3, 9, 10, 14, 16, 19, 23
NLoS	Not Line of Sight. 16, 23
NPSIR	Normalized Power Signal to Interference Ratio. xvii, xxi–xxv, 3, 5, 6, 8, 50, 51, 67, 74, 76–79, 82, 83, 108–110, 112
NRZ	non-return to zero. 80, 93
OCC	Optical Camera Communication. xx–xxvii, 3–11, 13, 14, 23–29, 31, 32, 42, 50, 51, 53, 62, 64, 65, 67, 68, 73, 78, 83, 94, 107–113
OFDM	Orthogonal Frequency Division Modulation. 23
OOK	On-Off Keying. xxi, 14–16, 22, 24, 80, 82, 85, 93, 108, 110
PCC	Pearson correlation coefficient. xxiii, xxv, 42, 55, 56, 58–62, 65, 68, 94, 96, 97, 102, 111, 112
PWM	Pulse Width Modulation. 20, 21
QAM	Quadrature Amplitude Modulation. 20
RF	Radio-Frequency. xix, xx, 1–3, 11

RGB	Red, Green, and Blue. 16, 19, 24
ROI	region of interest. 40, 43, 51, 54, 55, 57–63, 74–76, 87, 89, 92, 93, 102, 113
sCMOS	Scientific CMOS. 131, 132
SDMA	Spatial division multiple access. 9
SIR	Signal to Interference Ratio. 82, 132
SNR	Signal to Noise Ratio. 5, 10, 108
UDPSOOK	Undersampled Differential Phase Shift On-Off Keying. 20
UFSK	Undersampled Frequency Shift Keying. 22
UFSOOK	Undersampled Frequency Shift On-Off Keying. 18
UPAM	Undersampled Pulse-amplitude modulation. 20, 21
UPAMSM	Undersampled Pulse-amplitude modulation with Subcarrier Modulation. 19, 20
UPSK	Undersampled Phase Shift Keying. 12, 20
UPSOOK	Undersampled Phase Shift On-Off Keying. 19
UPWM	undersampled pulse width modulation. 20, 21
USA	United States of America. 4
USM	Undersampled Modulation. 22
UV	Ultraviolet. 27, 132
UWB	Ultra-Wide Band. 11
V2V	Vehicle to Vehicle. 26
V2X	Vehicle to Anything. 1, 3, 13
VLC	Visible Light Communication. xx, 2–4, 7, 10, 11, 14, 25, 26, 107
VLP	Visible Light Positioning. 11–13
WiFi	Wireless Fidelity. 11
WSN	Wireless Sensor Networks. xxii, xxiii, xxv, xxvii, 2–4, 8, 11, 14, 67, 68, 79, 92, 93, 108, 110–112, 133

Symbols

α is the frequency multiplier. The integer relation between the camera's frame rate and the emitter's switching frequency for symbol "10".

β is the angle of the camera-object horizontal plane intersecting the object's normal plane..

γ is the angle of the camera-objective vertical plane intersecting the objective's normal plane..

μ is the 2D average value of the pixel's intensity in an image.

φ is the relation between the camera's FoV and resolution.

σ is the 2D standard deviation of an image..

Glossary

B | C | D | G | I | L | P | S | U | W

B

BER is the rate at which errors occur in the transmission of digital data. It can be calculated as the number of bit errors divided by the total number of transferred bits during a studied time interval often expressed as a percentage.

C

Charge Coupled Device is a light-sensitive integrated circuit that stores and displays the data for an image in such a way that each pixel in the image is converted into an electrical charge the intensity of which is related to a color in the color spectrum.

CMOS is a technology for constructing integrated circuits used in microprocessors, microcontrollers, static RAM, and other digital logic circuits which are high noise immunity and low static power consumption. *See also:* Scientific CMOS (sCMOS).

D

demosaicking is a digital image process used to reconstruct a full color image from the incomplete color samples output from an image sensor overlaid with a Color Filter Array (CFA). It is also known as CFA interpolation or color reconstruction.

DSLR is a digital camera that combines the optics and the mechanisms of a single-lens reflex camera with a digital imaging sensor.

G

GPS GPS is a radio navigation system that allows land, sea, and airborne users to determine their exact location, velocity, and time 24 hours a day, in all weather conditions, anywhere in the world.

I

Infrared is, in the case of electromagnetic radiations, the ones that have a wavelength greater than that of the red end of the visible light spectrum but less than that of microwaves. Infrared radiation has a wavelength from about 800 nm to 1 mm, and is emitted particularly by heated objects.

IoT is a system of interrelated computing devices, mechanical and digital machines provided with unique identifiers (UIDs) and the ability to transfer data over a network without requiring human-to-human or human-to-computer interaction.

L

LED is a semiconductor light source that emits light when current flows through it.

P

photodiode is a semiconductor diode which, when exposed to light, generates a potential difference or changes its electrical resistance.

photon is an elementary particle that also exhibits properties of waves. A photon travels through space at the speed of light with a specific frequency that defines its energy and its classification along the electromagnetic spectrum (visible spectrum). The number of photons determines the intensity of light of an object emitting or reflecting those photons.

S

sCMOS is a technology based on next-generation CMOS Image Sensor design and fabrication techniques that offer extremely low noise, rapid frame rates, wide dynamic range, high quantum efficiency, high resolution, and a large field of view simultaneously in one image.

SIR is a measure that compares the level of a desired signal to the level of an interference to the system..

U

UV is a form of electromagnetic radiation with wavelength from $10nm$ ($30PHz$) to $400nm$ ($750THz$), shorter than that of visible light. UV radiation is present in sunlight, and constitutes about 10% of the total electromagnetic radiation output from the Sun.

W

wearable smart electronic device with micro-controllers that is worn close to and/or on the surface of the skin. These devices detect, analyze, and transmit information concerning body signals, or environmental data.

WSN is a group of dedicated sensors, generally spatially dispersed, used for monitoring, storing and transmitting environmental physical conditions. Usually the collected data is organized at a central location.